UNIVERSITÀ DEGLI STUDI DI PADOVA

Sede Amministrativa: Università degli Studi di Padova

Dipartimento di Ingegneria Industriale

Corso di Dottorato di ricerca in Ingegneria Industriale

Curriculum Ingegneria Energetica

XXXII° Ciclo

Theoretical and experimental analysis of the transient behaviour of refrigerated transport systems

Direttore della Scuola di Dottorato: Prof. Paolo Colombo

Coordinatore dell' indirizzo: Prof.ssa Luisa Rossetto

Supervisore: Prof. Davide Del Col

Cosupervisore: Dr.ssa Silvia Minetto

Dottorando: Paolo Artuso

Abstract

Refrigerated transport systems are employed in the cold chain to supply the consumer with safe, high-quality perishable freights. Differently from static refrigeration systems, refrigerated transport equipment is required to perform reliably in a wide range of ambient temperatures and under extremely variable weather conditions (solar radiation, cloudiness, rain etc…). Refrigerated vehicles include vans, rigid trucks and semi-trailers. The refrigerating system has to ensure a precise temperature control of the internal cargo space: given a certain perishable freight requiring a certain set-point temperature, a lower temperature might damage it while a higher temperature might reduce its shelf life or result in unsafe or low quality product for the consumer. Close temperature control systems for chilled goods require continuous, modulated refrigeration combined with high rates of air circulation.

This thesis contains the results of a study carried out during three years of PhD activity, conducted at the Construction Technology Institute (ITC) of the National Research Council (CNR) in Padova, where an official ATP test station is located. The ATP (Agreement on the International Carriage of Perishable Foodstuffs and on the Special Equipment to be Used for such Carriage) is an international agreement regulating the transport of perishable foodstuff. Starting from this experience, dedicated experimental activity was set up to collect data: ATP K-value measurement tests have been performed, along with step tests intended to evaluate the characteristic time constant of the insulated body of a brand new refrigerated van, designed to the carriage of chilled products (0°C-class refrigerated vehicle). The experimental data collected during the ATP test and step test of the brand new refrigerated van were used to develop and validate a 0-D, unsteady, lumped capacitance, simple numerical model of its insulated box. The numerical model presented in this thesis introduces a novel approach to model the average transient response of the insulated body of a refrigerated vehicle: the model is able to reproduce the actual performance of the structure without the need for the detailed drawing of the structure or the knowledge of the actual properties of the material used for the construction.

Under the stimulus of environmental sustainability and in order to offer the market with a natural alternative to F-gases, CO_2 was considered as a possible working fluid for refrigerating units serving refrigerated vehicles. A new lay-out for the cooling unit, developed for refrigerated transport application, which utilizes carbon dioxide as the working fluid, was developed. Starting from the experience developed in stationary refrigeration, but taking care of constraints specific of refrigerated transport, the cooling unit was designed to operate according to three different configurations: traditional low-pressure receiver cycle configuration, ejector cycle configuration and ejector cycle configuration utilizing an auxiliary evaporator located in the line between the ejector outlet and the low-pressure receiver. Numerical simulations of the refrigerating system operation with an internal cargo space temperature varying between -5°C and +15°C and an external ambient temperature spanning between 15 °C and 45 °C demonstrated that the operation of the refrigerating system with the ejector cycle configuration was convenient in hot climates and internal air temperature between +5 °C and -5 °C. For ambient temperature lower than 30 °C the operating range of the ejector could be extended with an auxiliary evaporator at the outlet of the ejector. Taking the coefficient of performance of the system as a thermal performance indicator, the ejector cycle configuration provided a maximum advantage by 15.9 % over the traditional cycle configuration at 42°C ambient

temperature and -5°C internal cargo space temperature. On the other hand, when the auxiliary evaporator was employed in the refrigerating system, the maximum advantage of 14.2 % on the COP was identified for an ambient temperature of 27 °C and an internal cargo space temperature of 5 °C.

After the numerical models of the cooling unit and the insulated body were developed, they were coupled and a typical delivery mission was defined. The selected delivery mission was characterized by a total of 12 door opening operations where doors are kept completely opened and heat enters directly from the external environment. Numerical results gave the input to insight on the correct dimensioning and sizing of a refrigerated transport cooling unit, but were also utilized to compare the thermal performance of the state of the art (i.e. cooling unit operating with R-134a as the working fluid) with the innovation proposed in this thesis. Moreover, numerical simulations were able to assess the main heat fluxes that influence the performance of the refrigerating system during operation.

Summary

1. Introduction

The cold chain is a temperature-controlled supply chain that facilitates the production, transportation and storage of perishable foodstuff such as fresh and frozen agricultural and seafood production, meat, chemicals and even pharmaceutical products. Since the deterioration rate of perishable products directly depends on the storage temperature at which they are kept, perishable goods should be kept refrigerated or frozen throughout the entire cold chain. A breakage in the cold chain determines product waste: according to Food and Agriculture Organisation of the United Nations (2017)[1] an estimated one third of all food produced globally is either lost or wasted along the food chain, before reaching the consumers.

Food production, pre-cooling, transport, storage and distribution are the main stages within the cold chain (Mercier et al., 2017 [2]): the main difficulties are encountered at the weakest links or interface as delivering, loading or unloading operations and temporary storage where perishable products are generally handled in somewhat uncontrolled temperature environments.

Land transportation by means of refrigerated vehicles is the most common mode of perishable transportation and represents one of the most important links in the cold chain (Mercier et al., 2017 [2], Oury et al., 2015 [3]). Refrigerated transport systems are then widely used to distribute chilled and frozen products through the world while they are required to operate reliably in much harsher environments than stationary refrigeration systems, given by the product to be transported (pre-cooled or not), a high variability of climatic conditions, variable orientation of the walls of the insulated body affecting solar radiation insisting on the walls, heat transfer between the outside air and the walls of the vehicle, infiltration of air from the external environment given by door opening operations. Consequently, refrigerated transport systems generally present poor Coefficient of Performance (COP) (Tassou et al., 2009 [4]) when compared to stationary refrigeration systems.

In addition, increasing the quantity of transported goods, home delivery and expectations on the quality of goods bring to increasing the use of refrigerated transport systems, resulting in a tremendous amount of energy consumption by the refrigerated transport industry (Tassou et al., 2009 [4]; Ahmed et al., 2010 [5]). In a study presented by the United Nations Environment Programme UNEP (2010) [6], an estimation of around 4 million refrigerated vehicles in service worldwide, including vans (40%), trucks (30%), semi-trailers or trailers (30%) was reported, forecasting by 2030 a growth by 2.5% a year of global road freight transport. A more recent document by Eurostat 2017 [7] reported that the total number of refrigerated vehicles in Europe was superior to 4 million at the end of 2016, with an increase of 1.6% respect to the previous year. In view of the growing importance of the refrigerated transport sector, United Nations adopted an internal governmental Agreement on Transportation of Perishable food stuff (ATP). The agreement was signed in Geneva on 1 September 1970 and introduces common internationally recognized standards for temperature-controlled transport vehicles such as road vehicles, rail wagons and sea containers, with the objective of facilitating international transport of perishable foodstuff while ensuring a high level of preservation during their carriage. The agreement establishes the appropriate temperatures under which the various types of perishable foodstuffs should be carried and lays down the requirements for the equipment, as well as the methods and procedures for measuring and checking them (United Nations, 1970 [8]). According to the ATP

standards, the insulating performance of a refrigerated vehicle is characterized by the overall heat transfer coefficient of its insulated body, K $Wm^{-2}K^{-1}$, which is measured in a climatic chamber. Below the value of 0.4 $Wm^{-2}K^{-1}$, vehicles are classified as "Reinforced Insulated" (IR), while between the value of 0.4 and 0.7 $Wm^{-2}K^{-1}$ they are classified as "Normally Insulated" (IN). Despite the level of insulation of the refrigerated vehicle, thermal performance of the insulation material deteriorates with time due to inherent foam characteristics (Tassou et al., 2009 [4], Capo et al., 2019 [9]), and the overall performance, identified by the K-value, is affected by many factors like the type of vehicle, the manufacturing process, the type of transport realized and the architecture of the refrigerating unit.

In a very recent paper by Capo et al., 2019 [9], the relative weight of each contribution was identified with reference to 1158 vehicles measured in French ATP stations. Recent data showed a typical loss of insulation value between 3% and 5% per year which can lead to considerable rise in the thermal conductivity after few years (Chatzidakis and Chatzidakis, 2003 [10], Economic Commission for Europe [11]), resulting in an significant increase in energy consumption and CO_2 emissions if the large number of refrigerated vehicles in use worldwide is considered. Furthermore, the value of the overall heat transfer coefficient of the insulated body can also be influenced by the manufacturing process: in a study provided by Estrada-Flores and Eddy (2006) [12] it was shown that for similar refrigerated vans the K -value can vary from 0.82 to 1.24 $Wm^{-2}K^{-1}$.

Energy consumption in the cold chain is still a global challenge and it is reported to account for 30% of total world energy consumption according to Kayfeci et al., 2013 [13]. Despite the ATP regulation, road transport is responsible for a considerable part of global emissions: the percentage of CO_2 emissions caused by truck transportation in the European Union has increased from 5.6% in 1990 to 9% in 2014, causing 14% of global emissions (Derrek et al., 2012 [14]). In 2016, Adekomaya et al. (2016) [15] stated that 15% of world's energy from fossil fuel is used in food transport refrigeration, and the environmental influence of emissions form food transport vehicles account for 40% of the global greenhouse effect. After all, diesel engine driven vapour compression systems account for huge fuel drain in transport refrigeration systems and by today they are the most common type of refrigeration system in use, with an expected coefficient of performance generally between 0.5 and 1.5 (Tassou et al., 2009 [4]). A typical refrigerated vehicle cooling system interacts with the truck cargo space and regulates the internal space condition to a certain temperature by extracting the heat from the cargo and transferring it to the external ambient environment. In refrigerated transport, methods for modulating refrigeration power to part-load operations include hot gas bypass, suction throttling, compressor ON/OFF and compressor speed control (International Institute of refrigeration, 2003 [16]).

Compressor speed control, either in stages or continuously through an inverter supply, is effective but is limited in its unloading capacity and needs an additional control method to reach low levels. By far, the most common temperature control in the refrigerated transport having a cooling unit based on a vapor compression cycle is a simple on-off feedback controller with hysteresis (James et al., 2006 [17]) where the compressor's on or off control action is driven by the difference between measured cargo space temperature and set-point temperature.

In the majority of food refrigeration systems, heat is transferred primarily by convection within the refrigerated space: air temperature and its homogeneity are directly governed by the patterns of airflow (James et al., 2006 [17], Moureh and Flick, 2004 [18], Smale et al., 2006 [19], Zertal-Menia et al., 2002 [20]). Different studies have shown a significant level of spatial temperature variability in

some food refrigeration systems (Estrada-Flores et al., 2002 [21]; Amos and Tanner, 2003 [22]; Tanner and Amos, 2003 [23]) with non-uniform airflow as a major cause of this variability. The air distribution system must provide sufficient airflow to absorb energy from heat sources (walls, door and often products itself) to avoid unacceptable temperature increase.

To maintain a uniform temperature throughout the cargo space, which is essential to maintain the quality, safety and extend the shelf life of perishable freights within the refrigerated space, the temperature level and homogeneity is governed directly by the airflow patterns.

Based on the low value of the coefficient of performance in refrigerated transport systems and on the increasing number of refrigerated vehicles in-service worldwide, any small improvement to the refrigerated transport sector could lead to a significant impact on the reduction of the world energy consumption. Numerical modelling offers and economic alternative to physical experiments, though a reliable model needs to be validated with experimental data.

For this reason, this thesis presents the complete analysis of a refrigerated transport system, composed by the insulated body, refrigerating unit and mission profile, by means of dynamic numerical simulations.

References

[1] Food and Agriculture Organization of the United Nations, “The future of food and agriculture: trend and challenges”, Rome, 2017. http://www.fao.org/3/a-i6583e.pdf.

[2] S. Mercier, S. Villenueve, M. Mondor, I. Uysal, Time–temperature management along the food cold chain: a review of recent developments, Comprehensive Reviews in Food Science and Food Safety, 16 (4) (2017), pp. 647-667.

[3] A. Oury, P. Namy, M. Youbi-Idrisi, Aero-Thermal simulation of a refrigerated truck under open and closed-door cycles, Proceedings of the 2015 COMSOL Conference, Grenoble (2015)

[4] S.A. Tassou, G. De-Lille, Ge Y.T., Food transport refrigeration–approaches to reduce energy consumption and environmental impacts of road transport, Appl. Therm. Eng., 29 (8–9) (2009), p. 1467

[5] M. Ahmed, O. Meade, M.A. Medina, Reducing heat transfer across the insulated walls of refrigerated truck trailers by the application of phase change materials, Energy Convers. Manag., 51 (3) (2010), pp. 383-392

[6] UNEP. Report of the Refrigeration, Air conditioning and Heat Pumps Technical Options Committee, 2010, UNEP.

[7] Eurostat Total number of relevant goods vehicles in the reporting countries, 2012-2016, https://ec.europa.eu/eurostat/statistics-explained/index.php?title=File:Total_number_of_relevant_goods_vehicles_in_the_reporting_countries,_2012-2016.png .

[8] United Nations, Agreement on the International Carriage of Perishable Foodstuffs and on the Special Equipment to be Used for Such Carriage (ATP), UNECE Transport Division, Geneva, Switzerland (1970)

[9] C. Capo, J.M. Petit, R. Revellin, J. Bonjour, G.Cavalier, Ageing of in-service refrigerated transport vehicles: a statistical analysis, proceedings of th 25th IIR International Congress of Refrigeration, Montreal, Quebec, Canada, 2019.

[10] S.K. Chatzidakis, K.S. Chatzidakis, Refrigerated Transport and Enviroment, 2003. Available from <http://www3.interscience.willey.come/cgi-bin/fulltext/109060950/PDFSTART/>.

[11] Economic Commission for Europe, TRANS/WP.11/2000/9, Inland Transport Committee, Working Party on the Transport of Perishable Foodstuffs (Geneva, 30 October- 2 November 2000), Comment to Annex 1, Appendix 2, paragraph 29, Transmitted by the expert from Denmark. Available from: <http://unece.org/trans/wp11/wp11doc/2000/wp110009.pdf/>

[12] S. Estrada-Flores, A. Eddy, Thermal performance indicators for refrigerated road vehicles, Int. J. Refrig., 29 (2006), pp. 889-898.

[13] M. Kayfeci, A keçebas, E. Gedik, Determination of optimum insulation thickness of external walls with two different methods in cooling applications, Appl. Therm. Eng., 50 (2013), pp. 217-224.

[14] R. Derrek, J. Bloemhof, I. Mallidis, Operations research for green logistics- an overview of aspects, issues, contributions and challenges, Eur. J. Oper. Res., 219 (3) (2012), pp. 671-679.

[15] O. Adekomaya, T. Jamiru, R. Sadiky, Huan Z., Sustaining the shelf life of fresh food in cold chain- a burden on the environment, Alex. Eng. J., 55 (2) (2016), pp. 1359-1365.

[16] International Institute of refrigeration, 2013, 16th Informatory Note on Refrigeration, refrigerated transport: progress achieved and challenges to be met. Available from: http://www.iifiir.org/userfiles/file/publications/notes/NoteTech_16_EN.pdf.

[17] S.J. James, C. James, J.A. Evans, Modelling of food transportation systems—a review, Int. J. Refrig., 29 (6) (2006), pp. 947-957.

[18] J. Moureh, D. Flick, Airflow pattern and temperature distribution in a typical refrigerated truck configuration loaded with pallets, Int. J. Refrig., 27 (5) (2004), pp. 464-474.

[19] N.J. Smale, J. Moureh, G. Cortella, A review of numerical models of air flow in refrigerated food applications, Int. J. Refrig., 29 (6) (2006), pp. 911-938.

[20] N. Zertal-Menia, J. Moureh, D. Flick, Simplified modelling of air flows in refrigerated vehicles, Int. J. Refrig., 25 (5) (2002), pp. 660-672

[21] S. Estrada-Flores, D.J. Tanner, N.D. Amos, Cold chain management during transport of perishable products, Food Aust., 54 (7) (2002), pp. 268-270.

[22] N. Amos, D.J. Tanner, Temperature variability during refrigerated vessel shipment of fresh produce, Proceedings of the 21st International Congress Refrigeration (2003), p. 8, ICR 0250

[23] D.J. Tanner, N.D. Amos, Temperature variability during shipment of fresh produce, Acta Hortic., 599 (2003), pp. 193-203

2. Modelling the ATP test facility

An ATP official test station, entrusted by the Italian ministry of infrastructure and transport, is located at ITC-CNR in Padua. This chapter describes the geometrical features of the test station, the characteristic of the cooling and measuring equipment and provides a description of the numerical model utilized to predict the internal air temperature evolution and the cooling energy consumed by the ATP test station.

This facility and its data acquisition system was used during the research activity to perform test on insulated boxes and refrigerating units. Furthermore, in the next chapter, the experimental data collected in the ATP test will be utilized to develop the numerical model of the insulated body of a truck.

2.1. The ATP test station

The ATP agreement requires testing of insulated trucks and refrigerated systems devoted to transport refrigeration in a controlled environment. The ATP foresees tests which require tunnel temperature ranging from -20 °C to 30 °C. The Padova Tunnel was designed to operate between 0 and 30 °C indoor temperature.

According to the ATP agreement, when a refrigerated truck is tested, the test tunnel must comply with the following requirements:

Table 2.1 – Test station's requirements according to the ATP agreement

Description	Range
Air velocity range	1-2 m s^{-1}
Temperature distribution outside the vehicle	Max +2 K
Temperature variation in time	0.3 K

No humidity control is required; however, humidity measurement is requested.

The official ATP test station is composed by two rooms: the tunnel, where refrigerated vehicles reside during the experimental tests, and the machine room, where the finned coil heat exchangers of a cooling unit, a fan-rack and finned electric heating resistances are located. The two rooms are coupled by the air-flow rate developed by the fan rack, the internal air of the tunnel is cooled down by the cooling unit, or eventually heated up by finned electric resistances and fan-heaters, depending on the temperature requirements given by the type of test that must be carried out. To ensure the air flow rate reaches the tunnel below with the minimum pressure losses due to the sudden change of direction, air flow deflectors (Figure 2.1 and Figure 2.3 b) are installed in the machine room and in the tunnel.

Figure 2.1 shows that the tunnel, where vehicles reside during the test, has a total internal length of 28 m. The floor area of the tunnel is 152.6 m^2, while the floor are of the machine room is 140.4 m^2 as two openings of equal area (8m^2) are present to allow the passage of air flowrate from the machine room to the tunnel and from the tunnel back to the machine room. The roof is a horizontal surface with an area of 161 m^2.

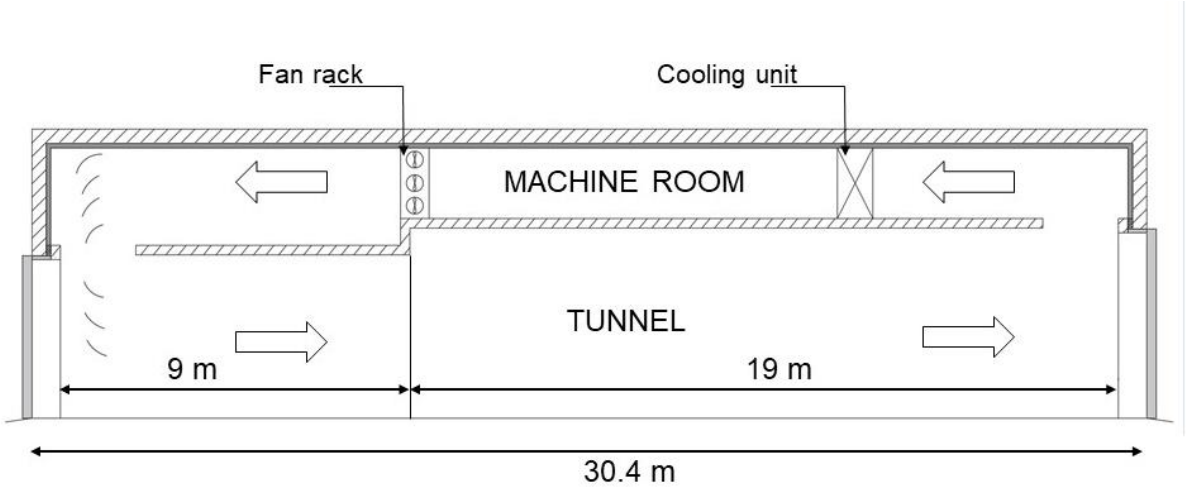

Figure 2.1 – ATP official test station's main dimensions

Table 2.2 reports the net areas of the vertical surfaces of the station (tunnel and machine room):

Table 2.2- Test station's opaque walls net areas

Description	Tunnel [m^2]	Machine room[m^2]
North	131.9	58.5
South	133.7	60.3
West	6.7	15.1
East	7.7	11.1

The South, West, East vertical walls of the station and the horizontal roof divide the inside air volume of the test station from the external environment and thus are defined as external walls, while the North wall divides the air volume of the station from the test station control room and an adjacent building, as reported in Figure 2.2. The air volume contained in the tunnel and in the machine room is equal to 728.7 m^3 and 346.9 m^3, for a total air volume of 1075.6 m^3, without quantifying the obstruction given by the presence of trucks under test, fan rack, cooling system etc…

The tunnel is provided of an entrance gate in the east wall, with an area of 16.8 m^2(4.2 m height x 4 m width) and an exit gate in the west wall, with an area of 19.6 m^2(4.9 m height x 4 m width), as the maximum dimensions of a truck must not exceed a width of 2.6 m, an height of 4 m and a length of 18.4 m.

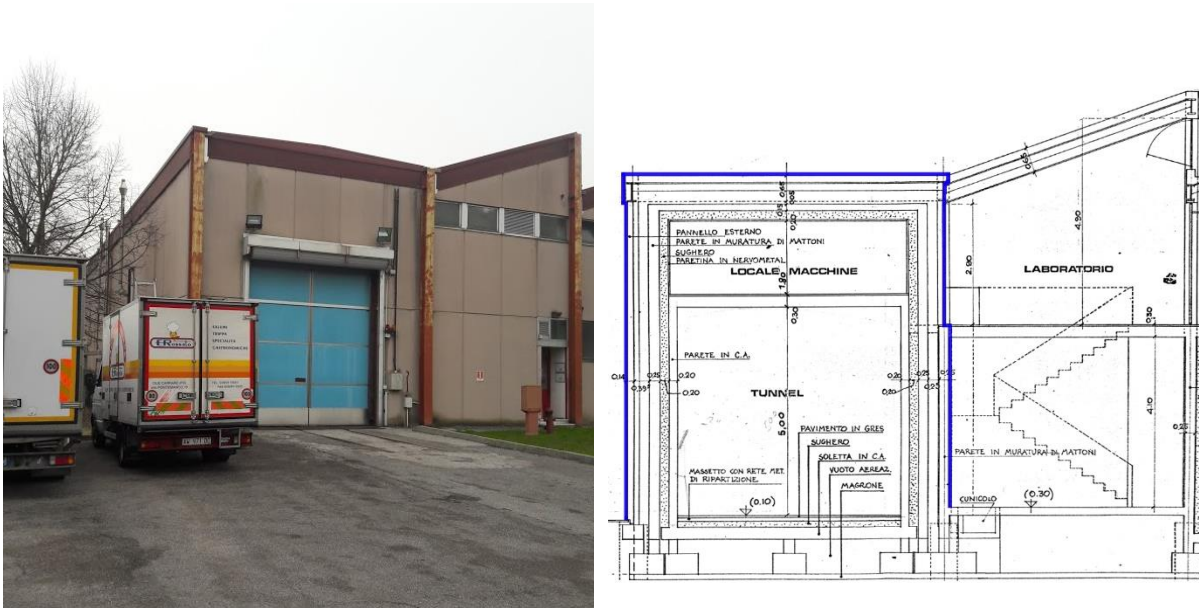

(a) (b)

Figure 2.2 – (a) ATP test station (b) Projects of the ATP test station and adjacent building

The gates are kept completely open to allow the truck to ingress the test station and are opened again once the test is over, thus the test station is provided by an oversized cooling unit which must provide a fast pull down of the internal air even in harsh conditions. The tunnel and the machine room are accessible through an entrance insulated door in the North wall, with an area of 1.8 m^2 (1.8 m height x 1 m width).

(a) (b)

Figure 2.3 – (a) Tunnel of the ATP test station, seen from the east gate (b) Air deflectors installed in the ATP test station

To stabilize and reduce the oscillations of the station's internal air temperature during the test 800 plastic bottles with a capacity of 1.5 L of water are located in the machine room, after the fan rack, for a total of 1200 kg (1200 L) of water to provide the necessary thermal inertia.

In the following tables (Table 2.3- Table 2.12) the stratigraphy of the walls of the ATP station is reported: for the definition of the U-value (Eq. 2.1) the wall construction and the total heat transfer coefficients considering a constant combined (convective and radiative) heat transfer are considered, with α_i = 7.7 $Wm^{-2}K^{-1}$ and α_e = 25 $Wm^{-2}K^{-1}$ for the internal and external surface respectively.

$$U = \frac{1}{\frac{1}{\alpha_i} + R_{TOT} + \frac{1}{\alpha_e}} \quad (2.1)$$

Table 2.3 – Stratigraphy of the Tunnel's north wall

Description	ρ [kg m^{-3}]	λ [$Wm^{-1}K^{-1}$]	c_p [kJ kg K^{-1}]	s [m]	R [W m^{-2} K^{-1}]
Reinforced concrete	2500	2.30	0.88	0.20	0.09
Cork	120	0.05	1.90	0.20	4.00
Brick masonry	1800	0.72	1.00	0.25	0.35
Air vertical layer				0.25	0.23
Brick masonry	1800	0.72	1.00	0.25	0.35
TOTAL				1.15	5.02
U-value [W m^{-2} K^{-1}]	0.19				

Table 2.4 – Stratigraphy of the tunnel's south wall

Description	ρ [kg m^{-3}]	λ [$Wm^{-1}K^{-1}$]	c_p [kJ kg K^{-1}]	s [m]	R [W m^{-2} K^{-1}]
Reinforced concrete	2500	2.30	0.88	0.20	0.09
Cork	120	0.05	1.90	0.20	4.00
Brick masonry	1800	0.72	1.00	0.25	0.35
Air vertical layer				0.25	0.23
Cement mortar	2200	1.40	1.00	0.14	0.10
TOTAL				1.04	4.77
U-value [W m^{-2} K^{-1}]	0.20				

Table 2.5 – Stratigraphy of the tunnel's east/west wall

Description	ρ [kg m^{-3}]	λ [$Wm^{-1}K^{-1}$]	c_p [kJ kg K^{-1}]	s [m]	R [W m^{-2} K^{-1}]
Reinforced concrete	2500	2.30	0.88	0.20	0.09
Cork	120	0.05	1.90	0.20	4.00
Brick masonry	1800	0.72	1.00	0.20	0.28
Air vertical layer				0.25	0.23
Cement mortar	2200	1.40	1.00	0.15	0.11
TOTAL				1.00	4.71
U-value [W m^{-2} K^{-1}]	0.20				

Table 2.6 – Stratigraphy of the tunnel's floor

Description	ρ [kg m^{-3}]	λ [$Wm^{-1}K^{-1}$]	c_p [kJ kg K^{-1}]	s [m]	R [W m^{-2} K^{-1}]
Gres	1500	1.60	0.90	0.05	0.03
Cement block	2000	1.43	1.00	0.10	0.07
Cork	120	0.05	1.90	0.15	3.00
Reinforced concrete	2500	2.30	0.88	0.30	0.13
TOTAL				0.60	3.23
U-value [W m^{-2} K^{-1}]	0.29				

Table 2.7 – Stratigraphy of the tunnel's slab

Description	ρ [kg m^{-3}]	λ [$Wm^{-1}K^{-1}$]	c_p [kJ kg K^{-1}]	s [m]	R [W m^{-2} K^{-1}]
Reinforced concrete	2500	2.30	0.88	0.25	0.11
Nervometal layer	7800	60	0.50	0.05	$8 10^{-4}$
TOTAL				0.30	0.11
U-value [W m^{-2} K^{-1}]	3.57				

Table 2.8 – Stratigraphy of the machine room's north wall

Description	ρ [kg m^{-3}]	λ [$Wm^{-1}K^{-1}$]	c_p [kJ kg K^{-1}]	s [m]	R [W m^{-2} K^{-1}]
Nervometal layer	7800	60	0.50	0.05	$8 10^{-4}$
Cork	120	0.05	1.90	0.20	4.00
Brick masonry	1800	0.72	1.00	0.25	0.35
Air vertical layer				0.25	0.23
Cement mortar	1800	0.72	1.00	0.25	0.35
TOTAL				1.00	4.93
U-value [W m^{-2} K^{-1}]	0.20				

Table 2.9 – Stratigraphy of the machine room's South wall

Description	ρ [kg m^{-3}]	λ [$Wm^{-1}K^{-1}$]	c_p [kJ kg K^{-1}]	s [m]	R [W m^{-2} K^{-1}]
Nervometal layer	7800	60	0.50	0.05	$8 10^{-4}$
Cork	120	0.05	1.90	0.20	4.00
Brick masonry	1800	0.72	1.00	0.25	0.35
Air vertical layer				0.25	0.23
Cement mortar	2200	1.40	1.00	0.14	0.10
TOTAL				0.89	4.69
U-value [W m^{-2} K^{-1}]	0.21				

Table 2.10 – Stratigraphy of the machine room's east/west wall

Description	ρ [kg m^{-3}]	λ [$Wm^{-1}K^{-1}$]	c_p [kJ kg K^{-1}]	s [m]	R [W m^{-2} K^{-1}]
Nervometal layer	7800	60	0.50	0.05	$8 10^{-4}$
Cork	120	0.05	1.90	0.20	4.00
Brick masonry	1800	0.72	1.00	0.20	0.28
Air vertical layer				0.25	0.23
Cement mortar	2200	1.40	1.00	0.15	0.11
TOTAL				0.85	4.62
U-value [W m^{-2} K^{-1}]	0.21				

Table 2.11 – Stratigraphy of the machine room's ceiling

Description	ρ [kg m^{-3}]	λ [$Wm^{-1}K^{-1}$]	c_p [kJ kg K^{-1}]	s [m]	R [W m^{-2} K^{-1}]
Nervometal layer	7800	60	0.50	0.05	$8·10^{-4}$
Cork	120	0.05	1.90	0.20	4.00
Brick masonry	1800	0.72	1.00	0.15	0.21
Air vertical layer				0.25	0.23
Cement mortar	2200	1.40	1.00	0.35	0.25
TOTAL				1.00	
U-value [W m^{-2} K^{-1}]	0.21				

Table 2.12 – Stratigraphy of the insulated doors and gates

Description	ρ [kg m^{-3}]	λ [$Wm^{-1}K^{-1}$]	c_p [kJ kg K^{-1}]	s [m]	R [W m^{-2} K^{-1}]
Fiberglass	1600	0.26	1.26	0.015	0.06
Polyurethane foam	40	0.025	1.80	0.12	4.80
Fiberglass	1600	0.26	1.26	0.015	0.06
TOTAL				0.15	4.92
U-value [W m^{-2} K^{-1}]	0.20				

From the wall characterization, is possible to observe that the U-value of the external walls dividing the internal air volume of the station from the external ambient conditions has a maximum value of 0.21 $Wm^{-2}K^{-1}$.

2.2. **The conditioning system**

The operating scheme of the cooling unit installed in the official ATP test station is reported in Figure 2.4. The evaporators and the expansion valves are located inside of the machine room, while the rest of the cooling unit is located outside, connected to the equipment inside of the machine-room with long pipes. The cooling unit is designed to extract heat from the air volume inside of the test station and reject it to the external environment, in order to ensure the temperature requirements essential to the experimental tests. The synthetic refrigerant utilized by the cooling unit is a near-azeotropic mixture, R404A.

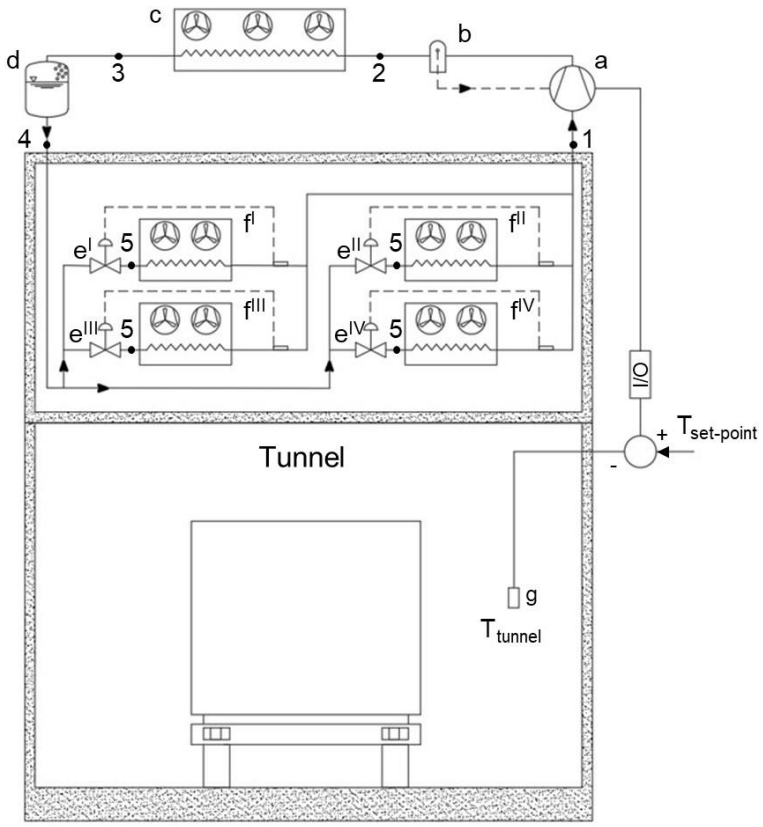

(a) Semi-hermetic compressor

(b) Oil separator

(c) Air-cooled condenser

(d) Liquid receiver

(e) Expansion valve

(f) Air-cooled evaporator

(g) Temperature sensor

Figure 2.4 - Installation of the refrigerating system on the official ATP test station

The compression of the refrigerant from the evaporation pressure to the condensation pressure is achieved by means of a semi-hermetic compressor(a) having a displacement volume of 871.61 cm^3 and operating at fixed speed. The nominal rotatory speed of the compressor at the frequency of 50 Hz is 1450 rpm, and thus the volumetric flowrate elaborated by the compression device is equal to 75.83 m^3h^{-1}. Two identical compressors (Dorin K 2500 CC) are installed in the test station (Figure 2.5a), for two main reasons: to contain the wear of the compressors in the long run, as the compressors operate in turn, and to ensure the continuity of operation of the cooling unit even in the case of malfunctioning of one of the compressors. The sizing of the compressor is performed with data provided by the compressor's manufacturer: at the conditions of evaporation temperature equal to -5 °C, a superheating of 10 K at the evaporator outlet, condensing temperature of 35 °C and no subcooling at the condenser outlet, the compressor can provide a refrigerating capacity of 54.7 kW while drawing an electric power of 16.4 kW and developing a mass flow rate of 1456.7 kg h^{-1}. The refrigerating capacity modulation is achieved with a simple thermostat that turns the compressor ON and OFF, depending on the difference between the temperature measured by the sensor located in the tunnel (g), T_{tunnel}, and the set-point temperature value, T_{tunnel}^{set}.

(a) (b)

Figure 2.5 – (a) Two identical semi-hermetic compressors outside the test station (b) Air cooled condenser and liquid receivers outside of the test station

An oil separator (b) separates the oil from the hot gas in the discharge line of the compressor and return it to the compressor crankcase with a dedicated line. After that, the refrigerant flows in the coils of the air-cooled condenser (Figure 2.5b), located outside of the test station, and rejects heat to the environment (T_{amb}). Two identical liquid receivers with the same capacity of 30 L are located at the condenser outlet and operate as storage tanks, ensuring liquid refrigerant entering the expansion devices. After the liquid-receiver, the refrigerant line is divided into 4 branches, leading to 4 thermostatic expansion valves, which expand the saturated liquid refrigerant to the state of two-phase mixture at the evaporation pressure and modulate to maintain a constant superheating of 10 K at the evaporator outlet.

Four identical finned coil evaporators (LU-VE S3HC 323) are installed in parallel inside of the machine-room of the test station, as reported in Figure 2.6a.

(a) (b)

Figure 2.6 – (a) Installation of the 4 finned coil evaporators inside the machine room (b) Electric resistances for defrost operation

The main dimensions of the cooling coils are reported in Table 2.13.

Table 2.13 - Main dimensions of the 4 identical evaporators

S_e	55.1 m^2
S_i	5.7 m^2
X_f	4.8 mm
N_{ROWS}	6
$\dot{V}_{AIR}$	7200 m^3h^{-1}
$P_{el,fans}$	525 W
Weight	71 kg
Length	0.48 m
Weight	0.49 m
Width	1.973 m

The total nominal cooling power of each evaporator at the conditions of inlet air temperature of 2.5 °C and evaporation temperature of -7.5 °C is provided by the evaporator's manufacturer and is equal to 20.2 kW. The defrost operation is performed in each evaporator by means of electric heaters (Figure 2.6b), each providing a heating power of 7.6 kW during operation; heaters are operated by a timer. The defrost interval is selected according to the seasonal humidity ratio. Under high humidity conditions, each evaporator might defrost up to 8 times per day to avoid ice accumulation.

The air-cooled condenser (Alfa-Laval BCM L 80) is equipped with a single row of three fans (Figure 2.5b), which are pressure controlled.

In order to assess a preliminary performance of the cooling system during operations, two pressure sensors were installed in the compressor's suction and discharge line (Figure 2.7a). The pressure sensor located in the suction line has an accuracy of 0.1% over the reading and evaluates the evaporation pressure considering the pressure loss on the pipes $p_{sucion} = p_{evaporation} - \Delta p_{eva-comp}$. The sensor located in the discharge line has an accuracy of 0.1% on the read value and assesses the condensation pressure lowered by the value of pressure losses between the condenser and the $p_{discharge} = p_{condensation} - \Delta p_{comp-cond}$.

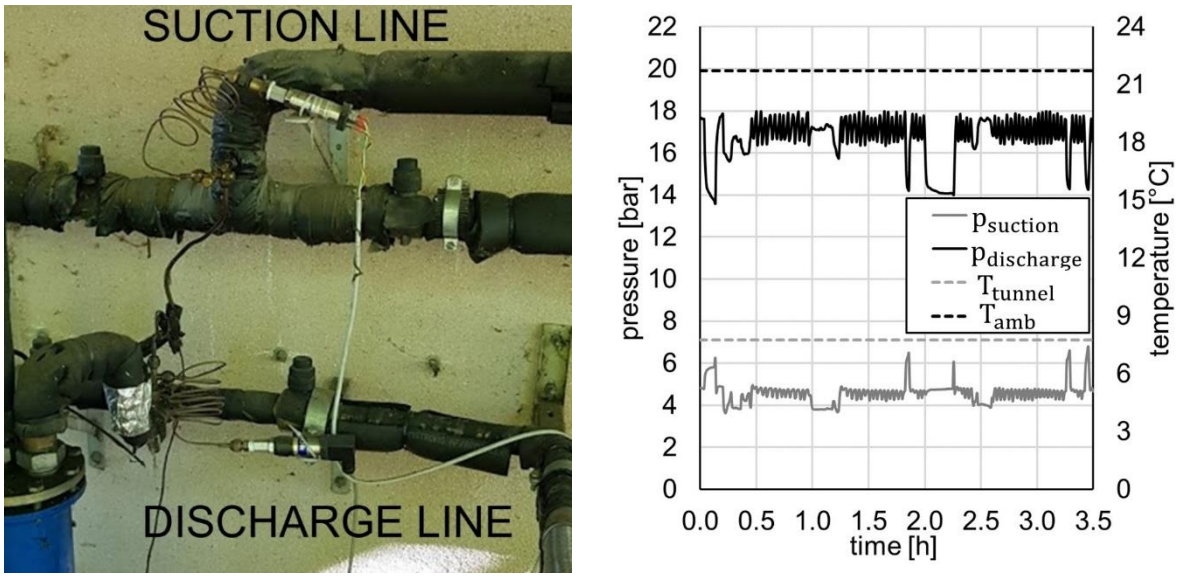

(a) (b)

Figure 2.7 – (a) Location of pressure sensors in the suction and discharge line of the compressors (b) Trend of discharge pressure and suction pressor of the compressor as a function of time

Data collection was carried out during 27th April 2018 and started at 12:30, ending at 16:00, for a total of 3.5 h with a sample acquisition interval of 30 s. During the test, the test station had a mean internal air temperature of 7.7 °C, while the mean ambient temperature of 21.7 °C was provided by the ambient data collected by the weather station of CNR of Padova. The mean discharge pressure was equal to 16.7 bar, corresponding to a saturation temperature of 36.6 °C and the mean suction pressure was equal to 4.6 bar, corresponding to a saturation temperature of -8.2 °C. The trend of the collected pressure and temperature is reported in Figure 2.7 b.

When the test requires indoor temperature higher than the outdoor one, heating is demanded to a rack of fan heaters.

2.2.1. The fan rack of the test station

The refrigerating system is coupled with a fan-rack, as the fans of the evaporators alone would not be able to move enough air volume to ensure the satisfaction of the velocity and temperature

requirements as required by the ATP agreement (paragraph 2.1.5, Annex 1, Appendix 2)[1]. The fan rack is composed by 10 identical fans (Figure 2.8a), and the characteristic curve of each fan is provided by the machine's manufacturer and reported in Figure 2.8b. Each fan has an impeller diameter of 400 mm, impeller's hub diameter of 160 mm, 5 pales, a pitch angle of 32° and a total weight of 36.6 kg.

(a)

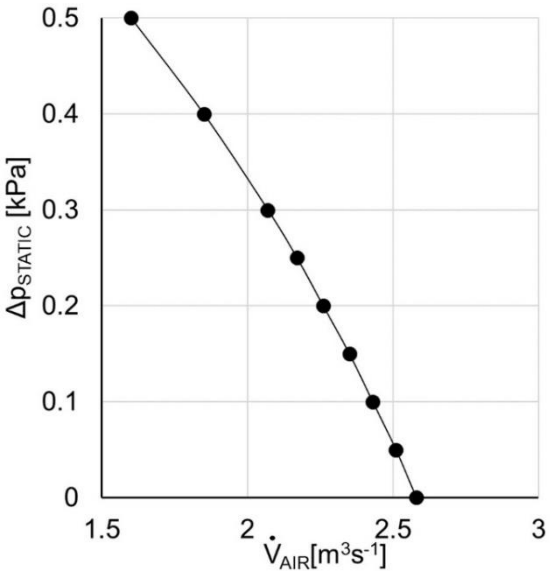

(b)

Figure 2.8 – (a) Fan rack installed in the machine room (b) Characteristic curve of the axial fans, provided by the manufacturer, at the nominal rotatory velocity of 2840 rpm

The nominal rotation velocity is 2840 rpm and the electric power draw is 1.73 kW for each fan, making a total of 17.3 kW of electric power draw for the total fan rack.

2.3. **Measurement in the ATP station**

The ATP station is provided of a total of 96 thermocouples to evaluate the insulated body's internal and external temperature during the test. The temperature sensors are T- type thermocouples. The temperature measurement chain is periodically calibrated using a reference Pt1000 sensor, to guarantee the satisfaction of ATP requirements in terms of total uncertainty. The accuracy of the thermocouples is ± 0.2 °C.

Electric power (see section 2.1.4) is measured with a in-house system with 2% accuracy over the reading. Humidity ratio is monitored with two capacitive sensors (Delta Ohm HD 9009TRR) with 2% of reading accuracy in the measuring range and 4 thin film anemometers (Delta Ohm HD2903TC1.2) monitor the air velocity, with rated accuracy ±(0.15 ms^{-1}+3% of measurement).

2.3.1. ATP test equipment

ATP tests performed to measure, the overall K-value of insulated bodies, require internal heating of the bodies themselves, until the test temperature is stably and uniformly reached, in accordance with the internal heating method described in Section 2, Annex 1, Appendix 2 of ATP[1] (See Appendix A).

Direct current heaters are used, which can be controlled and measured with 2% accuracy over the measured value.

The different type of fan-heaters are listed in Table 2.14:

Table 2.14 – Volumetric flowrate of the different types of fan-heaters

Desciption	N_{fans} [-]	$\dot{V}_{AIR}$ [m^3h^{-1}]
Type 1	1	38.8
Type 2	1	130
Type 3	3	170
Type 4	5	410

The number of fan-heaters employed during the ATP test is evaluated to satisfy the requirement of air movement prescribed by the ATP: it is then function of the air volume and thus of the dimensions of the insulated body, according to Eq. 2.2.

$$\sum_j N_{fan-heater,j}\, \dot{V}_{AIR,j} = (40 \div 70)\, V_i \tag{2.2}$$

The heating power of the fan-heaters is regulated with a PI controller which uses a control loop feedback mechanism to control their supply voltage, as reported in Figure 2.9:

The value of the temperature measured by the thermocouples, T_i is fed to the system which evaluates the error between the setpoint value and the measured value, $e_i = T_i^{set} - T_i$. The value of the error is then utilized to calculate the outlet. Table 2.15 reports the PI parameters as a function of the internal temperature range, which are utilized by the PI system to evaluate the output voltage V_{out}.

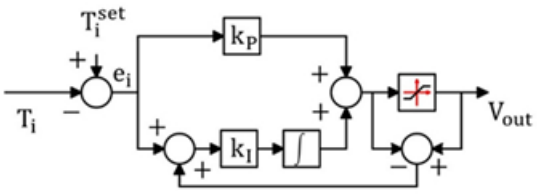

Figure 2.9 – PI controller with anti-windup scheme

Table 2.15 – PID parameters as function of internal temperature range

k_P [-]	k_I [-]	Range
10	1	T_i < 31.5 °C
1	1	$T_i \geq$ 31.5 °C

The value of the outlet tension V_{out} is always comprehended in the range [0 10] so that, the outlet tension is amplified (α) and the total heating power of the fan-heater can be expressed with Eq. 2.3:

$$P_{fan-heater}(t) = P_{ventilation}(t) + \frac{(\alpha V_{out})^2}{R} \quad (2.3)$$

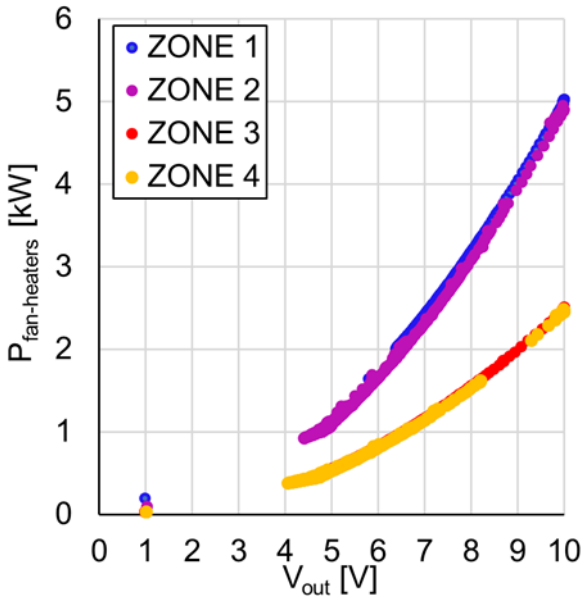

Figure 2.10 – Characteristic curve of outlet tension [0 10] vs. total heating power of the 4 different power stations

The ATP official test station is provided of 4 different power stations where the fan-heaters can draw the necessary electric power. Figure 2.10 provides the relationship between the supply voltage at the PID outlet and the heating power of the fan-heaters.

2.4. Development of the test station numerical model

A numerical model of the official test station was developed with the commercial software TRNSYS v.16 (TRaNsient SYstem Simulation Program) [2], which is provided by "Solar Energy Laboratory of the University of Wisconsin Madison". TRNSYS is an energy simulation program: the software includes a graphical interface, a simulation engine, a large suit of tools and a library of components which are identifies as Types. The dynamic simulation of every system is performed in TRNSYS connecting each system Type/component, according to an input-output logic, as the outputs of one component are graphically connected to the inputs of another. Each type/component of the system can be considered as a "black-box", that processes input data as a function of defined algorithms, starting from the user-defined parameters, and produces output-data.

The numerical model of the analyzed building was implemented by the TRNBuild program, using the multi-zone building type (Type 56). TRNBuild allows the operator to implement the geometrical and physical characteristics of the building envelope, and some parameters can still be adjusted to obtain the desired load profile: ventilation, infiltration ad internal gains. The building model developed with

TRNBuild was then included in a TRNSYS project. To be able to simulate the model, it is also necessary to include the information of weather conditions, which was taken form on of the TRNSYS meteorological libraries for the city of Venezia, which is the closest city to Padova on the ones available on TRNSYS libraries. The modellization of the building of the ATP test station was done according to the following steps:

1. Definition of the thermal zones
2. Definition of the walls' physical properties and orientations
3. Entering the necessary data to calculate the variables of the system
4. Description of the building structures

The first step is the definition of the number of thermal zones: an unique thermal zone accounting for the total air volume of the station was defined. The software requires also as input the capacitance, defined as total thermal capacitance of air zone plus that of any mass not considered as walls (i.e. forniture), the initial temperature and relative humidity of the air zone, and the humidity model, simple (capacitance) or detailed (buffer storage) model. TRNBuild defines as default the capacitance equal to 1.2 times the internal air volume, however, in the ATP station model this value had to be increased considering all the equipment inside of the station, according to Table 2.16:

Table 2.16 – Total capacitance considered for the TRNBuild model

Component	Weight [kg]	Capacitance [kJ K^{-1}]
Internal air volume	1296	1296
Evaporators mass	284	109.3
Fan rack total mass	360	324
Water bottle	1200	5023.2
TOTAL		6752.5

The effective thermal capacitance of the zone is then roughly 5.2 times the one given by the air volume alone. After the definition of the thermal zone and the total capacity, the software requires the assignment of the surface enclosing the inner volume. Each surface must be properly allocated in the space of the building with its size, gross area and type defining whatever the wall is external, internal, adjacent or boundary.

Table 2.17 – Tunnel's walls in TRNBuild

Wall	Orientation	Gross Area [m^2]	Type
Floor	Horizontal	152.6	Boundary
North wall	North	131.9	Boundary
Insulated door	North	1.8	Boundary
South wall	South	133.7	External
East wall	East	7.7	External
Insulated gate	East	19.6	External
West wall	West	6.7	External
Insulated gate	West	16.7	External
Slab		140.4	Internal

Table 2.18 – Machine room's in TRNBuild

Wall	Orientation	Gross Area [m^2]	Type
North wall	North	58.5	Boundary
Insulated door	North	1.8	Boundary
South wall	South	60.3	External
East wall	East	11.1	External
West wall	West	15.1	External
Ceiling	Horizontal	161	External

The surface definition for the tunnel and machine room walls is provided in Table 2.17 and 2.18 respectively.

After that, parameters related to heating, cooling, ventilation, infiltration, humidity, internal gains need to be implemented in the TRNBuild numerical model. The design parameters of the system can be supplied in three ways: by a constant value of the set-point, by means of a programmable daily or weekly schedule, or by the connection with an external input text file. The model was initially utilized to evaluate the monthly cooling demand of the ATP station: for this purpose, the heat load profile of the station was modelled according to Table 2.19:

Table 2.19 – Weekly schedule profile of the official ATP test station

Day(s)	Time	Cooling I/O	Doors status
Monday-Thursday	00:00-08:00	ON	Closed
	08:00-09:00	OFF	Opened
	09:00-17:00	ON	Closed
	17:00-18:00	OFF	Opened
	18:00-00:00	ON	Closed
Friday	00:00-08:00	ON	Closed
	08:00-09:00	OFF	Opened
	09:00-00:00	ON	Closed
Saturady-Sunday	00:00-00:00	ON	Closed

Table 2.19 describes the weekly schedule of the ATP test station. In the times when the cooling unit is ON, the fan-rack is intended to be in ON state constantly absorbing 17.3 kW, the fan-heaters of the 4 power station are modelled to provide the total maximum heating power of 15 kW and the fans of the 4 evaporators are constantly absorbing a total of 2.1 kW, giving a total heat load of 34.4 kW, in order to consider the worst case scenario. The internal surface heat transfer coefficient is modelled assuming a constant internal air velocity of 1.5 ms^{-1}, as a mean of the upper and lower limit of air velocity prescribed by ATP regulation [1]. Assuming for the internal air a convective turbulent flow where the characteristic length is the internal length of tunnel and machine-room, i.e. 28 m, the internal convective coefficient α_i is evaluated using a forced convection over a flat plate correlation[3] and is found to be equal to 4.9 $Wm^{-2}K^{-1}$ when the doors are closed and the fan-rack is certainly moving the internal air. When the doors are opened and the ventilation is OFF the internal heat transfer coefficient is evaluated with a natural convection over a plate correlation [3], obtaining a value of 1.86 $Wm^{-2}K^{-1}$. For the infiltrations heat load, the mass-flowrate was evaluated with the correlation of Foster et al. [4], according to Eq. 2.4:

$$\dot{V}_{inf} = 0.211\, A_{op}\, (gH)^{\frac{1}{2}}\, \left(\frac{\rho_i - \rho_o}{\rho_i}\right)^{\frac{1}{2}} \cdot \left(\frac{2}{1+\left(\frac{\rho_i}{\rho_o}\right)^{\frac{1}{3}}}\right)^{\frac{2}{3}} \quad (2.4)$$

The volumetric flow rate of external air infiltrating the ATP test station during door opening operations if expressed as a function of the opening area, height of the gates and internal and external density of air. The total infiltrating flow rate is given by the sum of the two volumetric flow rates given by the east and west gates. When doors are closed the test station is assumed to be perfectly sealed. The cooling power demand is defined as the cooling power the system must provide to continuously ensure the maintenance of the set-point temperature of 7.5 °C when doors are closed and cooling unit switched ON.

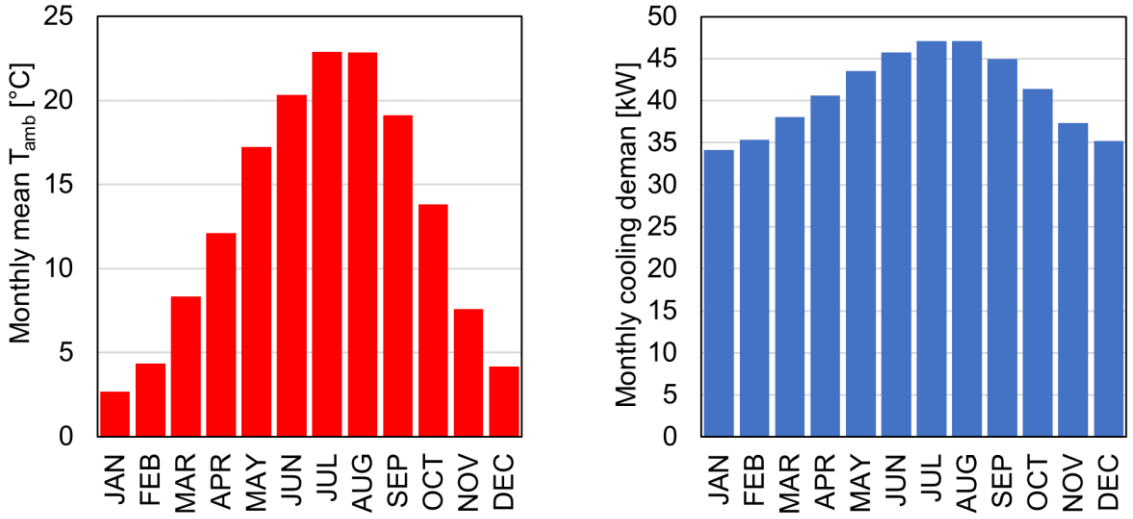

Figure 2.11 – Mean monthly (a) external ambient temperature (b) cooling demand of the ATP test station evaluated by the software TRNSYS

Figure 2.11a provides the value of monthly average ambient temperature, while Figure 2.11b provides the monthly mean cooling power demand. The maximum of cooling power demand is obtained in August, with a value of 47.1 kW. If the instantaneous value every hour is considered however, a peak of 59.7 kW is obtained, which justify the size of compressor and evaporators, described in the previous section.

Furthermore, on April 2017, the tunnel was heated up to a stable temperature of 30.5 °C. Once steady state condition was achieved, the cooling unit was set ON and the experimental data of the internal air temperature being pulled down from the value of 30.5 °C to the value of 7.5 °C were experimentally collected. During the pull-down operation the doors were closed and a total of 4 refrigerated truck were inside of the body. From the specifics of the truck, the weight of each truck was known and a corresponding capacitance was deducted, that had to be added to the previous total capacitance required by the model as described in Table 2.16. The model validation is provided in the following Figure 2.12 and it is possible to observe that simulated data are in good accordance with the one collected experimentally.

The tunnel simulation demonstrates that cooling is required all over the year, because of internal gains. The peak demand is estimated in 47.1 kW. These calculations are required as a new AC system is planned to be built in the next year, to comply with F-gas regulation and to achieve better energy efficiency.

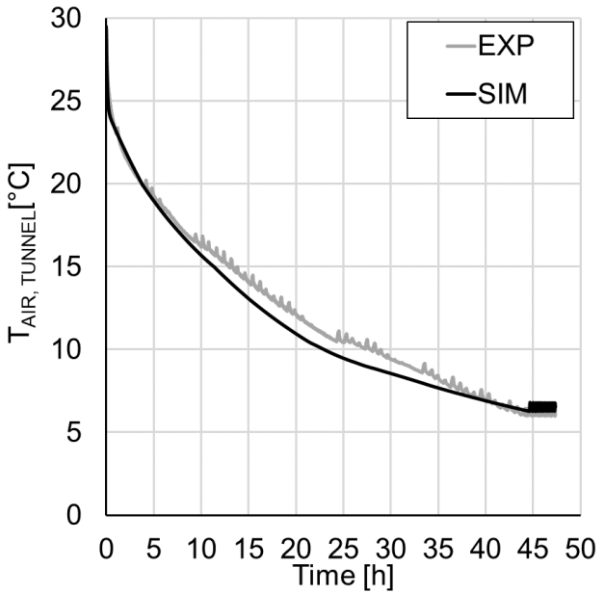

Figure 2.12 – Numerical model validation, simulated and experimentally collected internal air temperature during the pull down operation

References

[1]] United Nations, Agreement on the international carriage of perishable foodstuffs and on the special equipment to be used for such carriage (ATP), UNECE Transport Division, Geneva, Switzerland, 1970.

[2] TRNSYS - © 2006 by the Solar Energy Laboratory, University of Wisconsin-Madison

[3] ASHRAE. ASHRAE Fundamentals Handbook (SI), Chapter4, 2009.

[4] Foster, A.M., Barrett, R., James, S.J., Swain, M.J., 2002, Measurement and prediction of air movement through doorways in refrigerated rooms. Int. J. Refrigeration 25, pp.1102-1109

3. Modelling & experimental validation of the insulated box

In this section, the development and validation of a full-dynamic 0-D numerical model of the insulated body is presented. The model is able to reproduce the actual performance of an insulated body without detailed information on the structure or properties of the material used for the construction. The model is intended to be coupled with a refrigeration unit model (chapter 5), to foresee the truck performances under different boundary conditions.

The model is developed thanks to the experimental activity carried out in the official ATP test station, where experimental data are collected during the ATP test and following step test of several insulated bodies. As the ATP test provides the static characterization of the insulated box (K-value), the following step-test provides the dynamic characterization, summarized by the characteristic time τ of the dynamic response.

A full dynamic 0-D numerical model of the insulated body of a brand new refrigerated van was developed and validated against experimental data. The model was then utilized to evaluate the thermal performance of the refrigerated van during a long distance delivery mission, investigating the influence of solar absorption coefficient, mission profile and walls thermal mass on the cooling energy demand of the insulated body during the mission.

3.1. Experimental characterization of the insulated box

The insulated body of a refrigerated truck is the envelope containing the air volume where perishable freights are located during a mission. For a given truck, the average cooling demand depends on the external conditions and on the mission profile: solar radiation, ambient temperature, vehicle velocity etc. A deep knowledge of the dynamic behaviour of the wall structure is of vital importance to correctly predict the peak of cooling demand during a mission and to analyse how the insulated body reacts to thermal inputs, in order to correctly design and size the refrigerating unit. The static characterization of the insulated body structure is determined by the overall heat transfer coefficient K, which identifies the insulated performance of the box and reflects the vehicle's insulation design (i.e. thermal properties, aging, wear, vehicle shape, manufacturing process etc.). The dynamic characterization of the insulated body is determined by the characteristic time of its dynamic response.

With the purpose of evaluating the dynamic response of several insulated bodies to a sudden increase of heating power during the steady state condition achieved in the ATP test, a total of 45 step tests were conducted on different types of refrigerated vehicles under test in the official ATP test station.

3.1.1. Experimental system apparatus

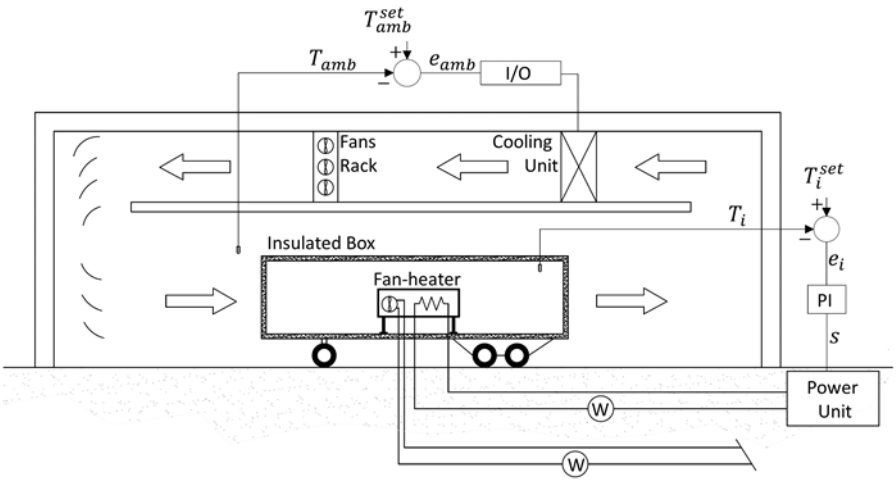

Figure 3.1 – Experimental apparatus employed during the tests

As discussed in the previous chapter, in order to carry out the ATP test with the internal heating method [1] (See Appendix A), fan heaters whose supply voltage (and consequently heating power) is modulated by a PI controller are installed inside of the insulated body during the test. To perform the step test, an automatic system using the software LABVIEW was developed: the system reads the PI output voltage , V_{out}, and the user can set the time for the step test, t_{STEP}, as input and provides an output voltage following the schedule provided in Table 3.1. The output voltage is than used to drive the power units connected to the fan heaters.

Table 3.1 – Schedule of the automatic system developed with LABVIEW

Time	Output voltage	Type of Test
$t < t_{STEP}$	V_{out}	ATP test
$t \geq t_{STEP}$	$1.2 \cdot V_{out}(t_{STEP})$	Step test

For each test, the value of t_{STEP} was chosen to ensure the achievement of steady state condition in the ATP test for at least 3 hours. During the time preceding the step test time, the PI controller provided as output the voltage required to achieve a stable temperature of 32.5 °C, and this signal is passed without modification to the power units. After the step time, the automatic system suddenly increased the pilot voltage of the fan heaters to a value equal to 120% of the PI output at that time, thus ensuring a sudden increase of heating power. The signal is then maintained constant regardless of the PI control signal. The trend of internal air temperature $T_i^{EXP}$and heating power $\dot{Q}_h^{EXP}$of the fan heaters experimentally collected during a typical test is provided in Figure 3.2.

As it can be observed from this figure, the entire test can be divided into three major zones:

1. ATP test: In this zone, the PI controller modulates the heating power of the fan heaters to achieve a stable internal air temperature of 32.5°C. Both heating power and internal air temperature have a dynamic trend.
2. Steady state condition of the ATP test: Once the heating power variation in one hour is less than 3%, steady state condition is achieved: the value of heating power $\dot{Q}'_h$ and internal air temperature T'_i are computed to evaluate the overall heat transfer coefficient of the insulated box, according to the definition given by the ATP agreement [1].
3. Step test: In this zone, the heating power of the fan heaters is suddenly increased to the value $\dot{Q}''_h$. The internal air temperature dynamically responds to this sudden increase of heating power to reach the new value of steady state condition T''_i which depends on the insulating performance of the box and the heating power after the step increase.

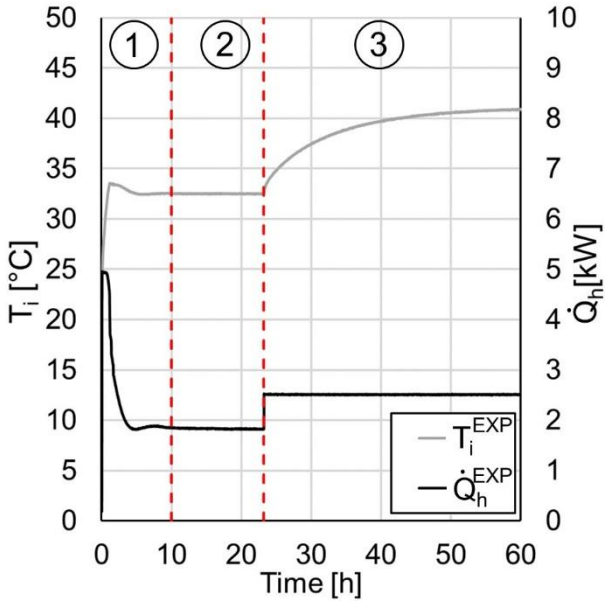

Figure 3.2 - Trend of the internal air temperature and heating power during the experimental test: (1) ATP test (2) ATP test steady state conditions (3) step test

The value of the internal air temperature achieved in the steady state condition after the step increase of heating power, T''_i, can be evaluated with Eq. 3.1, overall heat transfer coefficient is independent on the internal temperature value in this range:

$$T''_i = T'_i + \frac{\dot{Q}''}{K\,S_m} \tag{3.1}$$

where K is the overall heat transfer coefficient of the insulated body, measured during the steady state condition prior to the step test, S_m is the mean exchanging surface of the insulated body calculated as the geometrical mean between the internal and external surfaces of the box and $\dot{Q}''$ is the heating power of the fan-heaters after the step input.

During the experimental tests, it has been observed that, for the insulated box of a refrigerated vehicle, the transient region in which the system is responding dynamically can be in turn divided into 2 sub-

zones: a first sub-zone where the system responds rapidly to the power increase (Figure 3.3a) and a second sub-zone where the system is responding slowly to the sudden increase of power (Figure 3.3b). In the following analysis, the internal air temperature is considered in non-dimensional terms, according to Eq. 3.2:

$$T_{adm} = \frac{T_i - T'_i}{T''_i - T'_i} \tag{3.2}$$

The rapid response (Figure 3.3, red line) is considered in a range between the beginning of the step test and once the internal air temperature reaches 10% of the total temperature increase. On the other hand, the slow response (Figure 3.3, purple line) is considered in a range between the 20% of the total temperature increase and the end of the test.

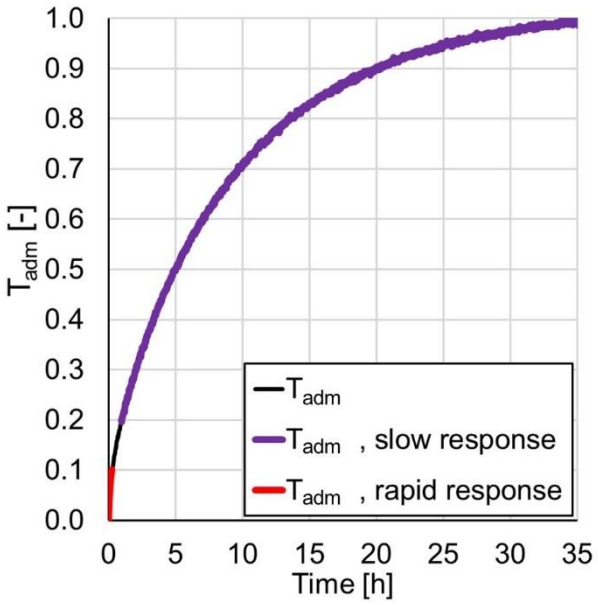

Figure 3.3 – Trend of the non-dimensional internal air temperature T_{adm} during the step test: highlight on rapid response and slow response

Both the response can be described as two different first order system responses, which development in time can be expressed as follow:

$$T_i(t) = T'_i + (T''_i - T'_i)(1 - e^{-\frac{t-\tau_D}{\tau}}) \tag{3.3}$$

In order to fit the experimental data, a best-fit exponential curve was constructed according to Eq. 3.4: the best-fit process consists into the research of a value of τ and τ_D that minimizes the error between the model's chosen function (Eq. 3.3) and the experimental data, under the constraint $T_{adm} < 0.1$ for the fast response and $T_{adm} > 0.2$ for the slow response:

$$\min\left\{\frac{\sum_{j=1}^{N_{data}} |T_{i,j} - T_{i,model,j}|}{N_{data}}\right\} \tag{3.4}$$

Where τ is the response's characteristic time and $\tau_D$is the time-delay.

The results of the best fit procedure are reported in Figure 3.4. The fast response shows a time constant one magnitude order lesser than the slow response. It is clear then, that the slow response is the dominant in the long run and thus was chosen as representative of the test.

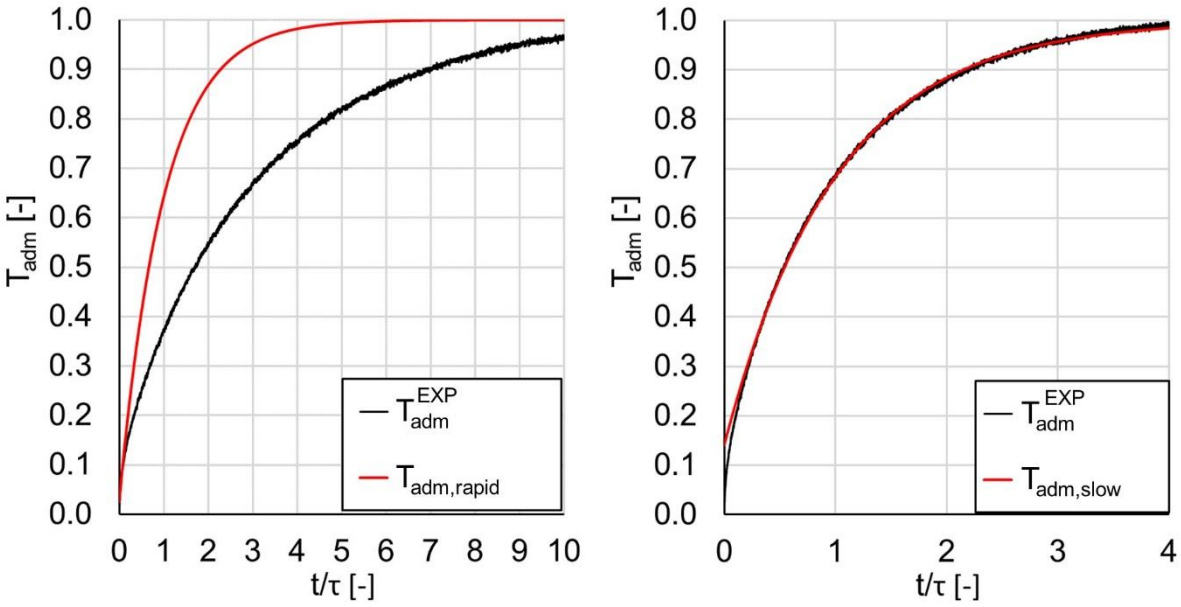

Figure 3.4 - Approximation of the process curve reaction to a first order linear system: (a) rapid response (b) slow response

3.1.2. Data collection and analysis

Following the procedure previously illustrated, a total of 45 step tests were conducted on different types of insulated bodies: depending on the internal air volume of the tested box, which provides a quantification of its dimension, it was possible to classify the type of refrigerated vehicles in three major classes, according to Table 3.2.

Table 3.2 – Classification of the type of trucks into three major classes

Class	**V_i [m^3]**
Small vehicle	5-35
Medium vehicle	40-65
Large vehicle	80-90

For each step test then, the characteristic time τ of the slow response was associated with the internal air volume of the insulated body V_i, as reported in Figure 3.5.

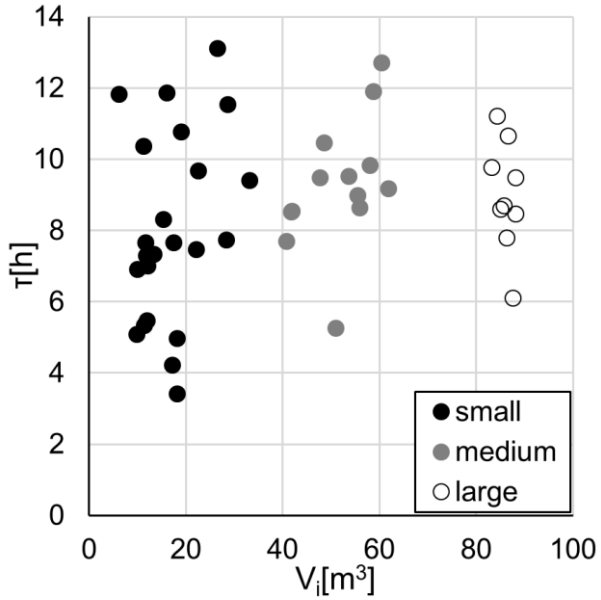

Figure 3.5 – Slow response characteristic time τ as a function of internal air volume V_i

Considering the three groups of vehicles previously mentioned, a volume-average value of the characteristic time $\bar{\tau}$ was estimated and reported in Table 3.3. The high dispersion of data around the mean value observed in Figure 3.5, can be ascribed to different reasons: different type of tested trucks, belonging to different manufacturers and thus assembled with different technologies. Not only the layers composing the insulated box could be different but the cooling unit and the purpose of the truck as well, thus leading to a different wear and aging of the insulated box [2]. The aging of the insulated body may play a major role.

Table 3.3 – Mean characteristic time of the three classes of refrigerated vehicles

Class	$\bar{\tau}[h]$
Small vehicle	8.3
Medium vehicle	9.4
Large vehicle	9.0

While the data are not sufficient to highlight a clear trend of the time response as a function of the vehicle size, they are valuable to assess the order of magnitude of the characteristic time for these systems, which vary between 5 and 13 hours. These values justify the effort in developing a dynamic model for the refrigerated box, as the presence of a slow transfer function between the external thermal loads and the cooling unit can strongly affect the time development of the cooling demand and its peak values.

3.2. Development of the insulated body numerical model

After the dynamic characterization of several insulated bodies of different types of refrigerated vehicles, the experimental data collected during the ATP and following step test of a brand new refrigerated van were used to develop a full dynamic numerical model of its insulated body. The numerical model was developed with the software MATLAB and was validated against experimental data previously collected.

Literature review showed that different authors have reported various studies presenting numerical models of refrigerated transport system in order to evaluate the system's performance during operation: Jolly et al.[3] developed a mathematical model to simulate the steady state performance of a shipping container refrigeration system. Sub models of compressor, evaporator, condenser and thermostatic expansion valve were created and later coupled by appropriate mass and energy transfer relation to form the full model. The model proved to be useful in the performance evaluation of different refrigerant in such systems but being in steady state conditions it was unable to evaluate the effect of the dynamically changing of external ambient conditions. Li et al.[4] considered the varying ambient temperature and developed a dynamic numerical model of the insulated body of a refrigerated vehicle coupled with the numerical model of a cooling unit, implementing an optimization algorithm in order to investigate on the optimal temperature bounds to regulate the cargo space temperature. The same authors later used the same numerical model to study the transient behavior of the cooling system during cooling/heating-mode switch cycling operations [5]. Tso et al.[6] developed a mathematical model of the refrigeration unit in a typical electricity-driven refeer, which considered the effects of hot gas bypass and suction modulation control on performance in partial load, but lacked a validation because of absence of experimental data and was restricted to steady state conditions. S.K. Chatzidakis et al.[7] studied a dynamic model based on a transient finite difference method to simulate a classical ATP test chamber coupled with a typical specimen refrigerated vehicle to be tested. The same authors also modelled the isothermal tanks that are widely used for the transport of perishable liquid foodstuffs like milk, wine, juice, etc… [8].

In majority of food refrigeration systems, heat is transferred primarily by convection: air temperature and its homogeneity are directly governed by the patterns of airflow. Different studies have shown a significant level of spatial temperature variability in some food refrigeration systems [9, 10, 11] with non-uniform airflow as a major cause of this variability. The air distribution system must provide sufficient airflow to absorb energy from heat sources as walls, door and often products itself to avoid unacceptable temperature increase: the optimizing of these systems is not an elementary problem and may require extensive experimentations. For this purpose, different authors made use of computational fluid dynamics (CFD) simulations to study the characteristics of airflow inside of the insulated body of a refrigerated vehicle [12,13]. Furthermore, temperature spatial variability is also affected by the frequent door openings refrigerated food vehicles are subject during their travel. In a survey carried by James et.al [14], the author stated that small-refrigerated vehicles that conduct multi-drop deliveries can be subjected to as many as 50 door openings, where there is heat ingress directly from outside and from personnel entering to select and remove products.

Tso et al.[15] used a commercial CFD program and modelled the heat and mass transfer during the door openings of a refrigerated vehicle, studying the impact on the internal space air temperature. A

series of experiments was carried out to study the effect of door openings with unprotected doors, with air curtains and with plastic strip curtains. The CFD simulations generally overestimated the temperature rise by between 3 and 4 °C which was believed to be due the effect of condensing water vapour in experimental situation. Moureh et al.[16] used Fluent with RSM turbulence model to predict the airflow pattern with a 3-D configuration of a typical refrigerated vehicle loaded with two rows of pallets. Later on, Moureh and Flick[17] used the numerical approach developed in the previous study to characterize the influence of an air-duct system and the narrow air space separation (1-2 cm) between pallets and walls. Tapsoba et al.[18] also used CFD with the RSM turbulence model to predict the 3-D airflow pattern within a refrigerated vehicle, with and without an air-duct system, loaded with two rows of slotted pallets.

While a lot of effort is used in modelling the internal air flow pattern and the cooling system performance, only few study focused on the development of a reliable dynamic model of the refrigerated body, even though it is a key element to relate the external loads to the actual heat flow on the insulated body internal surface.

For example, Estrada-Flores [19,20] discussed the dynamic response of diverse insulating walls, comparing different 1D numerical models approaches. Lumped models of a layered insulating wall were demonstrated inferior to Finite Elements Methods (FEM) discretization when dynamic response accuracy was considered. Despite the good capability of FEM to reproduce both steady and dynamic response, the presence of local thermal bridges and irregularities [21], such as structural elements or plate anchors inside the layered wall force the use of a full 3D model to obtain reliable results.

The numerical model developed in this study presents a novel approach to model the average transient response of the insulated body. A 0-D lumped parameter model is used to characterize the refrigerated box structure. In the next sections, the model is tuned and successively validated over experimental data. In this way, the actual performance of the structure can be reproduced without the need for the detailed drawing of the structure or the knowledge of the actual properties of the material used for the construction.

3.2.1. Case study

A refrigerated truck body with an internal air volume of 9.8 m^3 has been considered and experimentally characterized in the present study. The considered truck body was produced by ISOKIT s.r.l. and tests were performed less than one month after the end of the production. The insulated body's main dimensions are reported in Table 3.4.

Table 3.4 – Main dimensions of the insulated body

Length [m]	Value
H_e	2.0
L_e	3.0
B_e	2.0
H_i	1.8
L_i	2.9
B_i	1.9
Surface [m^2]	
S_e	32.0
S_i	27.9
S_m	29.9
Volume [m^3]	
V_i	9.8
V_e	12.0
V_{wall}	2.2

Based on widespread technology, walls are made up of three layers consisting of a polyurethane foam sandwiched between two thin fiberglass-based layers, reinforced with wooden and metallic structural component as needed to obtain the requested sturdiness. The floor includes an additional layer of plywood plate, necessary to meet the requested mechanical resistance. Complete stratigraphy of the walls was provided by the insulated bod's manufacturer and is presented in Table 3.5.

Table 3.5 – Stratigraphy of the 6 walls of the insulated body

Type of wall	Constituting elements
Lateral wall	Fiberglass: 1.5 mm Polyurethane: 67 mm Fiberglass: 1.5 mm
Floor	Fiberglass: 1.5 mm Plywood plate: 18 mm Polyurethane: 79 mm Fiberglass: 1.5 mm
Roof	Fiberglass: 1.5 mm Polyurethane: 97 mm Fiberglass: 1.5 mm
Front wall	Fiberglass: 1.5 mm Polyurethane: 67 mm Fiberglass: 1.5 mm
Rear wall	Fiberglass: 1.5 mm Polyurethane: 67 mm Fiberglass: 1.5 mm

The truck body was first investigated under steady state conditions, to quantify its global heat transfer coefficient K, as defined by ATP agreement (Figure 3.6).

During the initial part of the test, the heating power is set to its maximum level by the PI controller, corresponding to $\dot{Q}_{h,nom}$= 1.7 kW. As the difference between the measured internal air temperature and the set-point temperature of 32.5°C decreases, the PI controller modulates the value of the heating power until it reaches a steady state value of 0.27 kW, once the set-point temperature has been reached.

In this test, steady state condition is achieved after 3 hours from the beginning of the test, assuming as reference for stability a drift of the heating power less than 3% in one hour. The global heat transfer coefficient K (Figure 3.6b) is then calculated according to Eq 3.5, as defined by ATP agreement:

$$K = \frac{\dot{Q}_h}{S_m \, |T_{amb} - T_i|} \tag{3.5}$$

The values of heating power, internal and external temperatures are averaged over a 30 min period, once the steady state condition is achieved. A value of 0.36 W m^{-2} K^{-1} for the insulated body was

evaluated, thus classifying the refrigerated truck body as heavily insulated equipment (K≤ 0.40 W m^{-2} K^{-1}) according to the ATP standards body types. After 7 hours from the beginning of the test, 4 of which under stable conditions, a step test (Figure 3.7), where a Southden increase in heating power is applied, was performed to document the dynamic response of the system. The trend of the non-dimensional temperature T_{ADM} is presented in Figure 3.7a: as previously mentioned, the trend of the experimental process reaction curve can be approximated as a first order linear system response with a characteristic time of 5.1h as reported in Figure 3.7b.

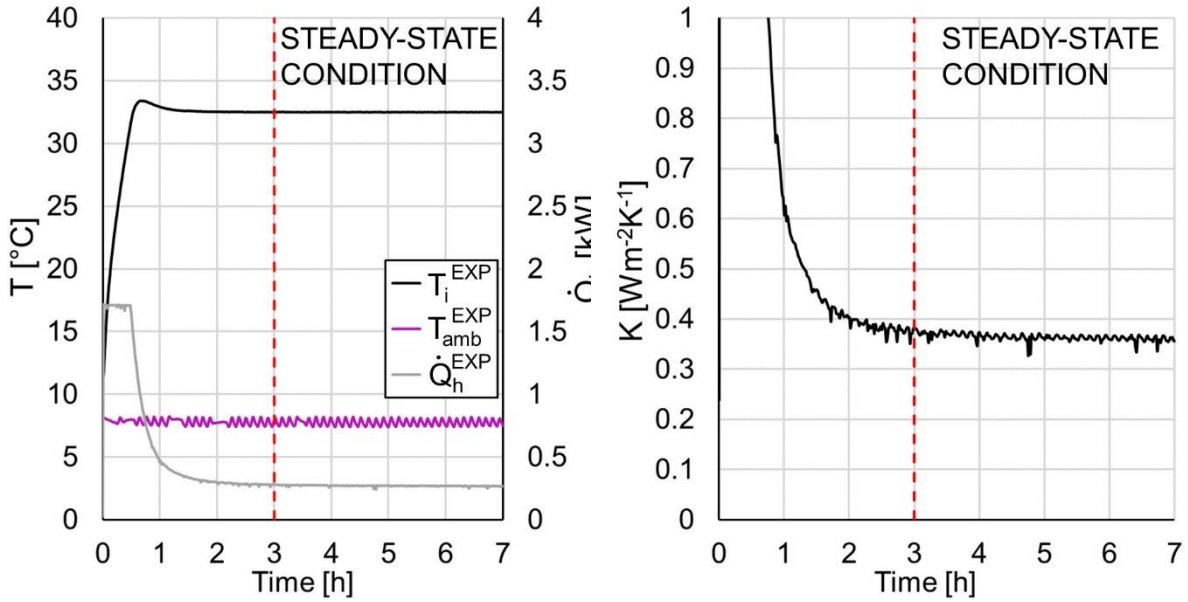

(a) (b)

Figure 3.6 – Experimental data collected in the ATP test (a) Internal air temperature, test station's internal temperature and heating power (b) Overall heat transfer coefficient

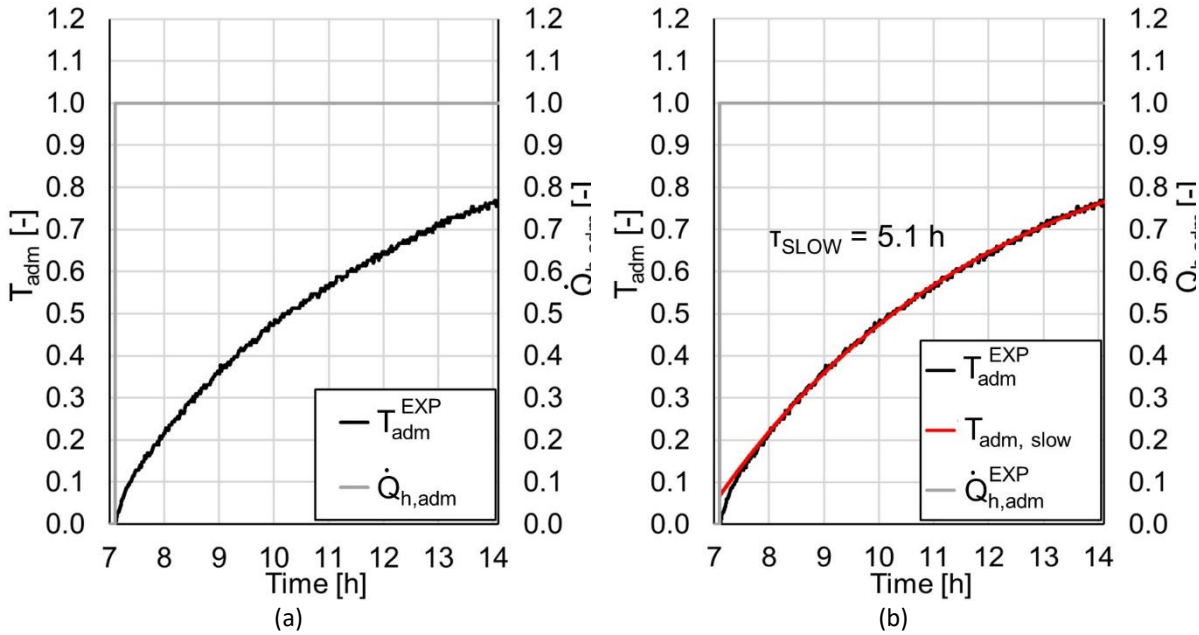

(a) (b)

Figure 3.7 – Non-dimensional trend of internal air temperature and heating power during the step test (a) experimental values (b) experimental values and first order linear system

3.2.2. Numerical model development

In order to develop a simple and reliable numerical model able to correctly reproduce the dynamic thermal behavior of the system composed by the insulated body walls, the internal air and the additional equipment or goods inside of the box, a lumped capacitance zero dimensions transient modelling method was chosen, solving for the node temperatures as a function of time

The whole insulated box was modelled as a 0-D model defined by a series of resistances and capacities. With the aim of increasing the capability of the equivalent formulation to reproduce the actual average response of the insulated box, thus including the impact of both distributed and localized effects on the average internal temperature, a series of lumped resistance and capacities was used. The extreme nodes of this series represent the internal and external average surface temperature of the box. In the present case, preliminary studies, demonstrated that the use of 12 capacities ($C_0, \dots, C_{11}$) and 11 resistances ($R_1, \dots., R_{10}$) were enough to reproduce the experimental response of the box, as presented later in section 3.2.3.

The total structure thermal resistance and thermal capacity are then calculated as the algebraic sum of the components:

$$C_w = \sum_{j=0}^{11} C_j \tag{3.6}$$

$$R_w = \sum_{j=1}^{11} R_j \tag{3.7}$$

Using a thermal-electric circuit analogy, the whole system can be represented with a thermal network composed of electrical resistance and capacitance, as can be seen in Figure 3.8, which provides the illustration of the box model and provides a better illustration of the heat transfer phenomena taken into account in the system.

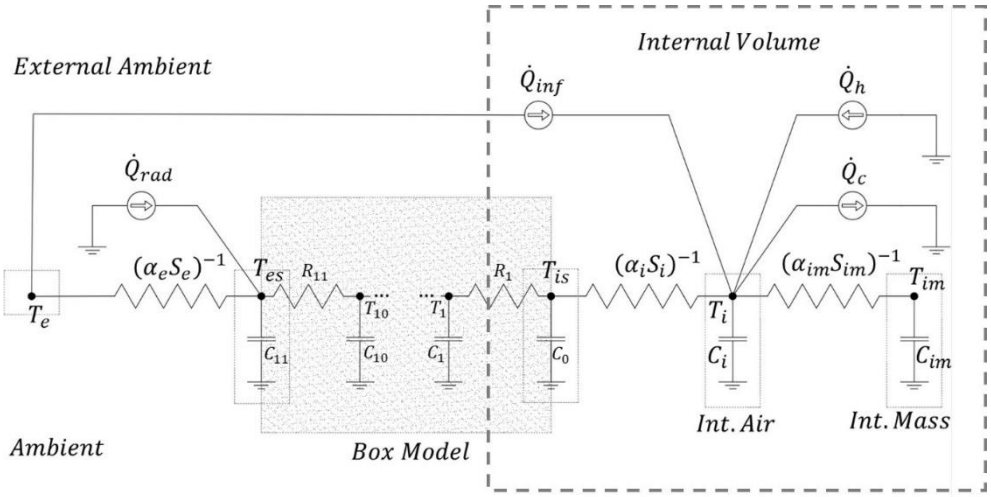

Figure 3.8 - Thermo-electric circuit analogy of the system: Insulated box model and internal and external elements.

The model on the external side account for the convection and radiation exchanges, insisting on the average external surface temperature T_{es}. The average air volume, at temperature T_i, is instead

influence by the infiltration load ($\dot{Q}_{inf}$), heating or cooling power ($\dot{Q}_h$, $\dot{Q}_c$) and convection with the internal wall temperature. A further convection term was considered to model the exchange between the air and other capacities inside the box, such as heating or cooling equipment or transported goods, represented by the capacity C_{im} at temperature T_{im}.

The linear differential system defined by Eq.s 3.8-3.12 provides the energy balance of the internal air (Eq. 3.8), the interior and exterior surface heat balance governing equations (Eq. 3.9 and 3.11 respectively), the equivalent refrigerated box model thermal balance (Eq. 3.10) and the energy balance between the internal air and the internal mass (Eq. 3.12).

$$C_i \frac{dT_i}{dt} = \left(\dot{Q}_h - \dot{Q}_c\right) + \alpha_i S_i (T_{is} - T_i) + \alpha_{im} S_{im} (T_{im} - T_i) + \dot{Q}_{inf} \tag{3.8}$$

$$C_0 \frac{dT_{is}}{dt} = \alpha_i S_i (T_i - T_{is}) + \frac{1}{R_1}(T_1 - T_{is}) \tag{3.9}$$

$$C_j \frac{dT_j}{dt} = \frac{1}{R_{j+1}}\left(T_{j+1} - T_j\right) + \frac{1}{R_j}\left(T_{j-1} - T_j\right) \ , \ j = 1 \dots 10; \ \dots$$
$$\dots \text{ with } T_0 = T_{is} \text{ and } T_{11} = T_{es}; \tag{3.10}$$

$$C_{es} \frac{dT_{es}}{dt} = \frac{1}{R_{11}}(T_{es} - T_{10}) + \alpha_e S_e (T_{amb} - T_{es}) + \dot{Q}_{rad} \tag{3.11}$$

$$C_{im} \frac{dT_{im}}{dt} = \alpha_{im} S_{im} (T_i - T_{im}) \tag{3.12}$$

The convective heat transfer coefficient α_i is assumed to have a constant value deduced with measurements of the internal surface temperature during the ATP test, while on the external surface the convective heat transfer coefficient α_e is computed from a convection over a plate correlation [22], due to its dependence to the vehicle velocity during operation. The conductive resistance of the wall is considered as a unique conductive resistance for the whole insulated body $R_{w,}$ accounting for the overall insulating capacity of the box.

$\dot{Q}_{rad}$ is the net solar gain (Eq. 3.13), given by four different contribution: the direct solar radiation, the diffusive incident solar radiation, the radiation heat exchanged between the surface and the sky and between the surface and the ground [23]:

$$\dot{Q}_{rad} = \sum_{u=1}^{6} S_u \left[a_s \left(\vec{I}_{dir} \cdot \hat{n}_u + I_{diff} \right) + \sigma\varepsilon \left(\frac{(1+\hat{n}_u \cdot \hat{k})}{2} \left(T_{sky}^4 - T_{es}^4 \right) + \frac{(1-\hat{n}_u \cdot \hat{k})}{2} \left(T_{amb}^4 - T_{es}^4 \right) \right) \right] \tag{3.13}$$

where u=1..6 refers to the six external surfaces and their respective orientation $\hat{n}_u$ and $\hat{k}$ is the normal vector toward sky globe. Truck orientation was assumed to be constant with respect to the solar radiation, with the front of the refrigerated box normally oriented North. The fictive sky temperature is calculated by assuming the sky to be an ideal black surface and can be determined by [24]. Assuming

an unpainted Glass-Fiber Reinforced Plastic (GFRP) surface, surface absorptivity a_s was set to 0.15, and surface emissivity ϵ was set to 0.90 according to [25].

The infiltration heat load $\dot{Q}_{inf}$ is given by the leakage of outside air into the insulated body during the opening of the vehicle's doors or due to the imperfect seal of the doors during operation: the volumetric flowrate $\dot{V}_{inf}$ of external air entering the vehicle body is modelled after the study of Micheaux et al.[26]. During the door opening operation the volumetric flowrate $\dot{V}_{inf}$ is evaluated assuming an instantaneous and complete door opening while during transportation, when the door is closed, the volumetric flowrate entering the internal space corresponds to an air change per hours of 0.02 h^{-1} [3], , which correspond to $\dot{V}_{inf} = 0.02\ [h^{-1}]\ V_i$.

$\dot{Q}_h$ and $\dot{Q}_c$ represent respectively the heating and cooling thermal sources inside the insulated box. The control system is modelled for both the heat sources as a PI control with output $s \in [0..1]$. A simple anti wind-up scheme was implemented to limit the maximum values of the integral part. The PI controller logic is presented in Figure 3.9.

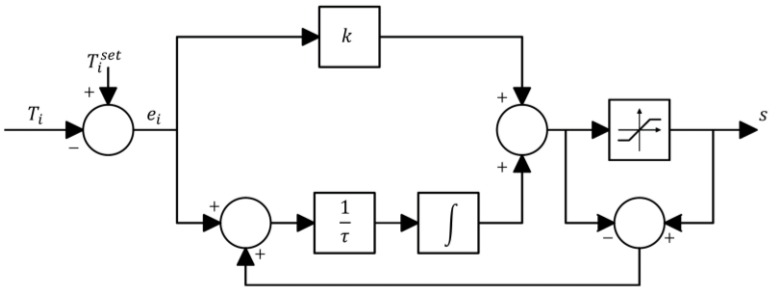

Figure 3.9 - PI controller scheme

3.2.3. Tuning of the numerical model

The parameters required as input to the numerical model are the thermal capacity and thermal resistance of the walls. Initially these values were assumed from the average wall thickness and composition of the insulated box walls (Table 3.5). The value of 632.3 kJ K^{-1} for the total wall thermal capacity was computed from the average wall composition, assuming for the polyurethane foam $C_p^{foam} = 1450$ J kg^{-1} K^{-1}; $\rho^{foam} = 35$ kg m^{-3} and $C_p^{f.glass} = 1260$ J kg^{-1} K^{-1} $\rho^{f.glass} = 1700$ kg m^{-3} for the fiberglass as follow:

$$C_W^{av} = \sum_{j=1}^{n} S_j \delta_j C_{p,j} \tag{3.14}$$

where j refers to the generic layer composing the walls of the insulated body. The value of 863 x 10^{-4} K W^{-1} for the thermal resistance R_w^{av} of side wall of the truck body was experimentally measured by means of heat flow meter apparatus on a 500mm x 500mm x 70mm samples. This apparatus allows determination of the thermal resistance with an accuracy of 2%.

Figure 3.10a and 3.10b provides the trend of temperature prediction if the average wall characterization were to be used to characterize the equivalent refrigerated box model in equations 3.8-3.12, given as input the heating power $\dot{Q}_h$ measured during the experimental activities.

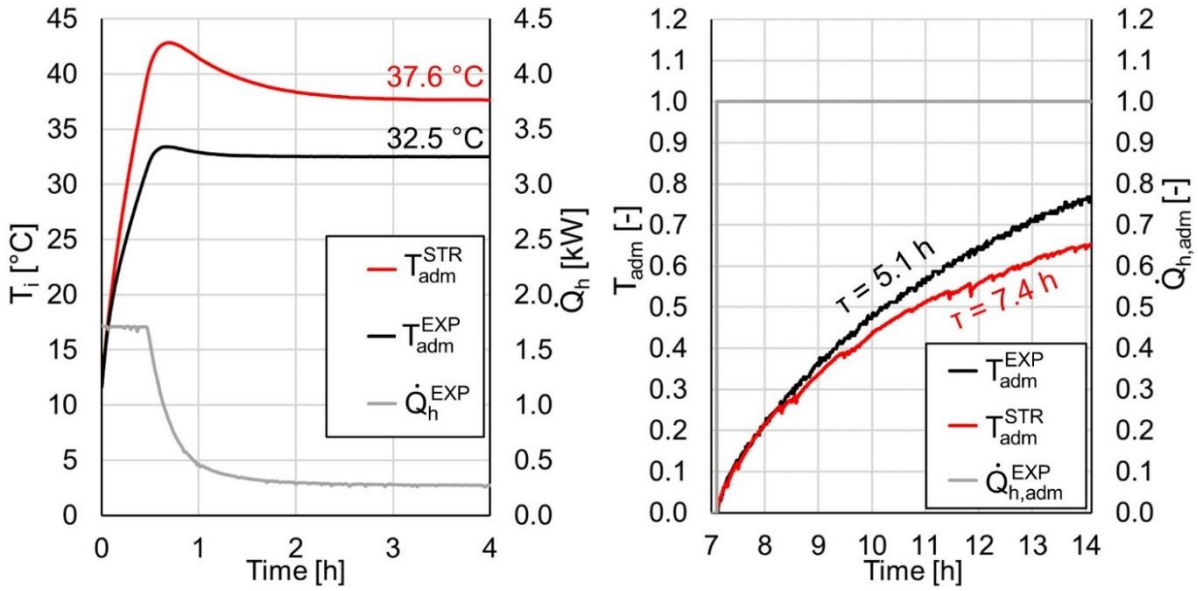

Figure 3.10 – (a)Experimental and numerical results during the ATP test using the average wall composition (b) Experimental and numerical results during the step tests using the average wall composition

It can be observed that the steady state condition is achieved at 37.6°C instead of 32.5°C and the maximum difference between temperature prediction and experimental value is equal to 9.5 °C during the dynamic evolution of the internal air. Similar results are obtained in the simulation of the step-response (Figure 3.10b) using the thermal properties evaluated from the average wall thickness characterization: it can be observed that the non-dimensional trend of the step response is slightly different from the experimental trend, having a characteristic time of 7.4h instead of 5.1h. The stratigraphy data lead to significantly overestimate the insulation capacity and underestimate the characteristic time.

This confirms that the overall thermal capacity, as well as the insulation characteristics, cannot be reliably derived from the wall average composition (i.e. stratigraphy), since a great part of the insulated box mass is made by wooden and metal localized reinforcement.

The data collected during experimental activity were used to tune and validate the model in both dynamic and steady-state conditions. The use of experimental data allowed to obtain a reliable model, avoiding the need for detailed description of the box structure and materials, and the resolution of a 3D thermal model accounting for all the thermal pairs and bridges of the structure.

The value of the wall's thermal capacity C_w and conductive resistance R_w were then optimized to fit experimental data. Others variable optimized were the thermal capacity C_{im} and the convective heat loss factor $\alpha_{im}S_{im}$ of the internal mass inside of the insulated box, i.e. internal cladding of the walls, fan-heaters and evaporator, which were included into the model as the internal mass of equation 3.12. The optimal value of these 4 parameters has been found through formulation of an optimization problem in Matlab aimed at minimizing mean quadratic error between the measured and simulated temperature of the internal air during the test. These 4 lumped parameters represent the equivalent

values of the physical parameter to be used in the lumped model in order to catch the real behaviour of the truck body.

$$\text{Find } [C_w\ R_w\ C_{im}\ (\alpha_{im}S_{im})] \text{ which minimize } \ MSE = \frac{\int_0^{t_{max}} (T_i - T_i^{EXP})^2 d\tau}{t_{max}} \tag{3.15}$$

under the following constraint: $\dot{Q}_h(t) = \dot{Q}_h^{EXP}(t)$; $T_{amb}(t) = T_{amb}^{EXP}(t)$. The simulations were initialized to their experimental value at the beginning of the test where available. The internal mass temperature T_{im}, which was initialized to the experimental value of the inside air temperature given the absence of a temperature measurement of the fan-heaters and evaporator, while the inside wall nodes, which were initialized by assuming a linear temperature profile between the internal and external surface at the beginning of the test.

The value of 8.7 W m^{-2} K^{-1} for the external surface heat transfer coefficient was calculated using a correlation for convection over a flat plate [22]; as a function of air velocity, which was assumed to be constant and equal to 2 m s^{-1} during the test. As for the value of the internal surface heat transfer coefficient, the value of 7.5 W m^{-2} K^{-1} was deduced from the measurements of the internal surface temperature during the experimental test and was found to be in accordance with the value of 8 $Wm^{-2}K^{-1}$ evaluated from Comini et al. [27].

Table 3.6 – Numerical model's optimum parameters

Parameter	Definition	Value
C_w	Wall thermal capacity	632.3 kJ K^{-1}
R_w	Wall resistance	863 x 10^{-4} K W^{-1}
C_{im}	Internal mass thermal capacity	29.6 kJ K^{-1}
$\alpha_{im}S_{im}$	Internal mass conductance	371.8 W K^{-1}

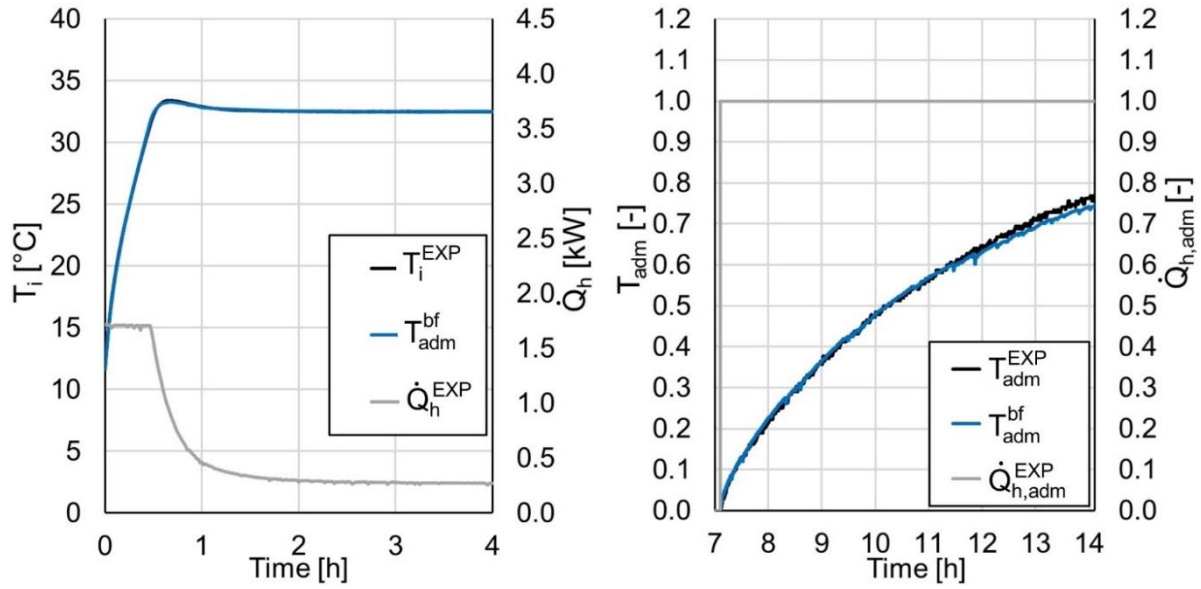

(a) (b)

Figure 3.10 – (a)Experimental and numerical results during the ATP test using the best fit values (b) Experimental and numerical results during the step tests using the best fit values

The prediction of internal temperature by the model was compared with the experimental data (Figure 3.10a), finding that the model results are in an excellent agreement with the experimental temperatures and getting a maximum difference between simulated and experimental internal temperature lower than 0.3 K.

3.2.4. Model validation and discussion

Experimental data were collected during a step test, performed in order to validate the optimum parameter set up, as described in the previous section. The temperature predicted by the model, compared with the experimental data collected during the step test is reported in Figure 3.10b. The numerical model was able to predict the dynamic evolution of the internal temperature, having a difference between the predicted temperature and the experimental temperature always below 0.1 K. While the results of the best fitting can be related to the nominal dimensions, as stated before, the direct characterization of the vehicle parameters from the average walls composition can lead to significant errors, as the thermal bridges and the structural components are ignored.

Table 3.7 shows the average wall composition data (av) in comparison with the best fit values (see Table 3.6).

Table 3.7 - Comparison between global optimum wall parameters and the average wall composition data

Parameter	Definition	Best fit	av	Δ
C_w	Wall thermal capacity	632.3 kJ K^{-1}	333.28 kJ K^{-1}	47 %
R_w	Wall resistance	863 x 10^{-4} K W^{-1}	1052 x 10^{-4} K W^{-1}	-23 %

The best fit value of thermal mass is almost two times higher compared to the value obtained from the average wall characterization, as it includes the additional mass inside the truck body envelope, i.e. wooden and metal localized reinforcements. This additional mass inside the truck body structure not only increases the value of thermal mass but also introduces thermal pairs and bridges, causing an overall reduction in thermal resistance.

3.3. **Modelling of a long road delivery mission**

The dynamic numerical model of the insulated body developed and validated in the previous section was utilized to investigate the dynamic behaviour of a refrigerated vehicle during a transport mission. The developed mission consists of a single day mission where the truck has to travel from a distributor's premises to another.

The external conditions, i.e. the hourly ambient temperature, relative humidity and intensity of solar radiation are provided by the climate data available in Energy Plus [28]. A reference summer day of the standard climatic year of Athens has been chosen to represent a high load condition.

The refrigerated cargo is modelled as the internal mass of Eq. 4.12 and consists of 1000 kg bovine carcasses, having a specific heat capacity of 3.25 kJ kg^{-1} K^{-1} [29] and a convective heat transfer coefficient which is equal to 8 $Wm^{-2}K^{-1}$ [30] during transport operation.

The cooling unit's maximum power of 2575 W, evaluated at the at 0 °C and 30 °C internal and external temperature respectively, was chosen from a commercial catalogue by Carrier [31].

3.3.1. Mission definition

Mission was designed to reproduce a long-distance delivery, and is described by setting the vehicle speed, the state of the cooling system (operating or not), the opening of the doors and the fraction of the prescribed cargo. Mission variables are reported in Table 3.8.

Precooling operation must take place before the mission: the air inside of the insulated body is pulled down to its set point value for long enough to reach a steady state condition. After the precooling operation, the refrigerated vehicle is loaded with the refrigerated cargo. During loading (and unloading) operation, the cooling unit is kept off and the insulated box is put in contact with a controlled environment at $T_{amb} = T_i^{set}$ (thus nullifying the thermal load given by the leakage flow), since the goods are loaded into the enclosure directly from a cold store, where they had been precooled. In order to make the simulated mission as real as possible, at least one stop must be planned. During stops the cooling unit is assumed to be active. On the other hand, when the refrigerated vehicle is parking at the owner's premises and empty, the cooling unit is kept off.

Table 3.8 – Mission profile: velocity; cooling unit operation time; cargo fraction; door opening time

Time [hr]	v [km h^{-1}]	Cooling I/O	Load	Door status
06:00 – 07:00	0	OFF	0 %	Closed
07:00 – 09:00	0	ON	0%	Opened
09:00 – 10:00	0	OFF	Linearly increasing from 0 % to 100 %	Closed
10:00 – 15:00	70	ON	100 %	Closed
15:00 – 16:00	0	ON	100 %	Closed
16:00 – 19:00	70	ON	100 %	Closed
19:00 – 20:00	0	OFF	Linearly decreasing From 100 % to 0 %	Opened
20:00 – 22:00	0	OFF	0 %	Closed

Initial conditions of the model were obtained by simulating the empty truck still under the variable ambient conditions for a time long enough for the solution to be independent from the initial conditions. Simulations were run to discuss the thermal dynamic loads of the truck during the mission.

3.3.2. Simulation results

The simulation model allowed to identify how the dynamic load and the mission profiles affect the actual cooling power demand inside the truck. Three heat fluxes were chosen to describe the system behaviour: the cooling power demand $\dot{Q}_c$, the conduction heat flux between the internal and the external surface of the box $\dot{Q}_{cnd} = \frac{1}{R_w}(T_{es} - T_{is})$, and the heat flux on the external surface given by the ambient conditions $\dot{Q}_e = \dot{Q}_{conve} + \dot{Q}_{rad}$, which can be obtained as the sum of the convective, $\dot{Q}_{conve} = \alpha_e S_e (T_{amb} - T_{es})$, and of the radiating heat flux (Eq.3.13). All these fluxes are reported in Figure 4.11. Figure 4.11a compares the conduction flux between the interior and the exterior of the insulated box and the cooling demand of the refrigerating system. The average heat conduction is quite constant during the day, and approximatively equal to 300 W. The cooling demand flows closely this value, except between 7:00 to 8:00 and 10:00 to 11:00, when the refrigeration unit is cooling the air inside of the box to the set value. Despite the refrigeration unit is oversized and can provide a much larger power than the average conduction load, which for the considered mission is 253 W, the pull-down time at the beginning of the mission is significant (75'), justifying the sizing proposed by the commercial catalogues for a similar truck body. While the conduction heat flow through the box walls is quite constant, the fluxes on the external side of the wall change significantly during the mission, as reported in Figure 3.11b.

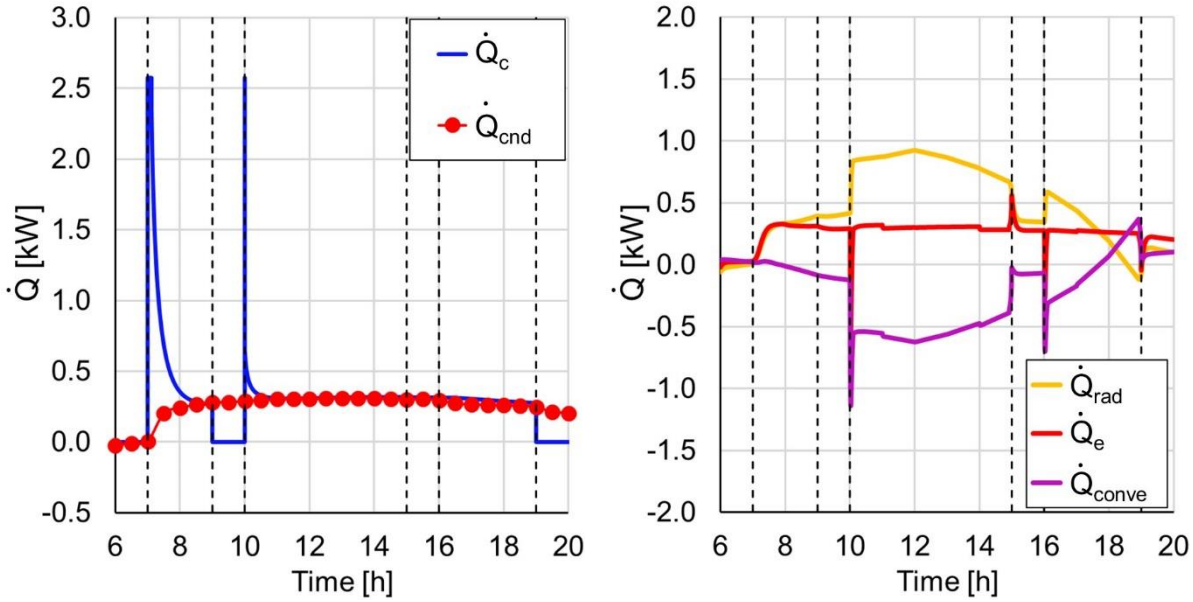

(a) (b)

Figure 3.11 – (a) Cooling power demanded by the insulated body and conductive flux through the walls. (b) External heat fluxes during the mission

Radiation and convection act for the great part of the day counterbalancing each other: the solar radiation increases the surface temperature above the ambient temperature; this leads to an increase both in the convective and in the radiative exchange with the ambient, although the two contributes have different signs.

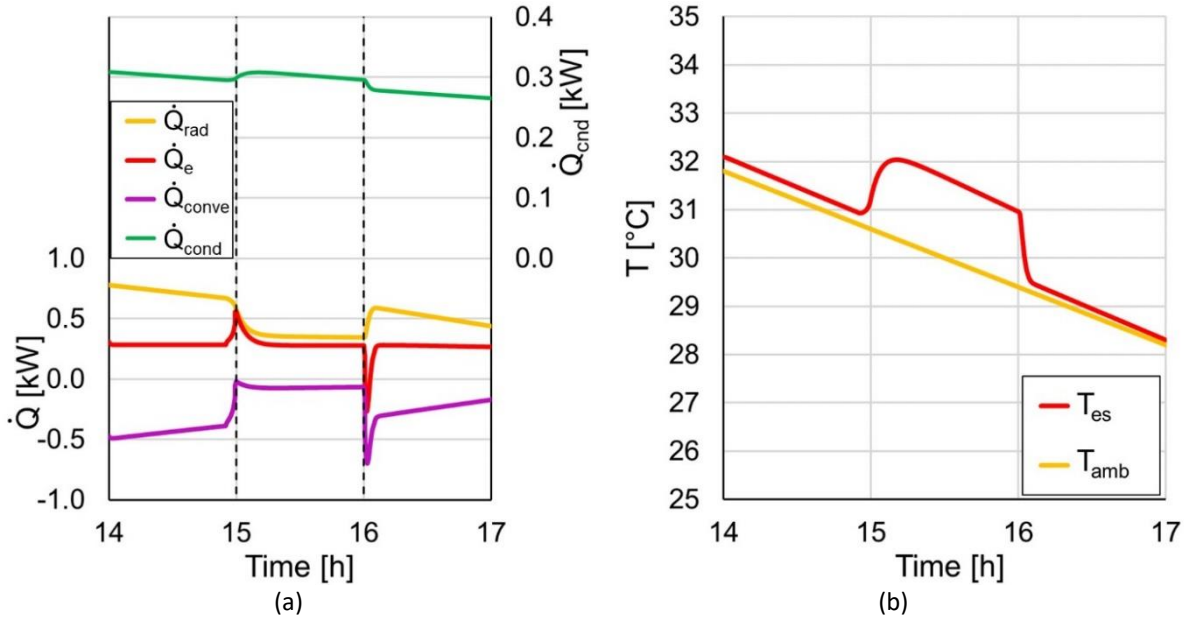

(a) (b)

Figure 3.12 – (a) Radiation and convective heat transfer rate (b) External wall temperature

Figure 3.12 details the heat flux and the temperatures on the external wall between the 14:00 and the 17:00. When the vehicle is moving the external wall temperature (T_{es}) reaches its equilibrium at about +0.3°C above the ambient temperature (Figure 3.12b). On the other hand, when the vehicle is not

moving (15:00 – 16:00) the solar radiation heat transfer ($\dot{Q}_{rad}$) becomes dominant over convection ($\dot{Q}_{conve}$) leading to a new equilibrium at +1.7 °C, as visible in Figure 3.12b. The peak in the net external flux $\dot{Q}_e$ at 15:00 is related to the wall thermal capacity, thus not impacting on the conduction flux: the trend of the conductive heat through the box walls is visible in Figure 3.12a, increasing its value by 13 W and reproducing the same trend of the external wall temperature T_{es}.

3.3.3. Comparison between a mass and a massless model

The thermal mass of the walls of a refrigerated vehicle determines the amount of thermal energy which may be stored within the structure and provides the thermal inertia against the external temperature fluctuations, making it an important characteristic for transient thermal behaviour. In order to make considerations on the effect of thermal mass on the cooling energy required during the mission and on the dynamic load, the results of a wall-massless model (obtained by imposing C_j=0 (j=1…11) on Eqs. 3.8-3.12 are considered.

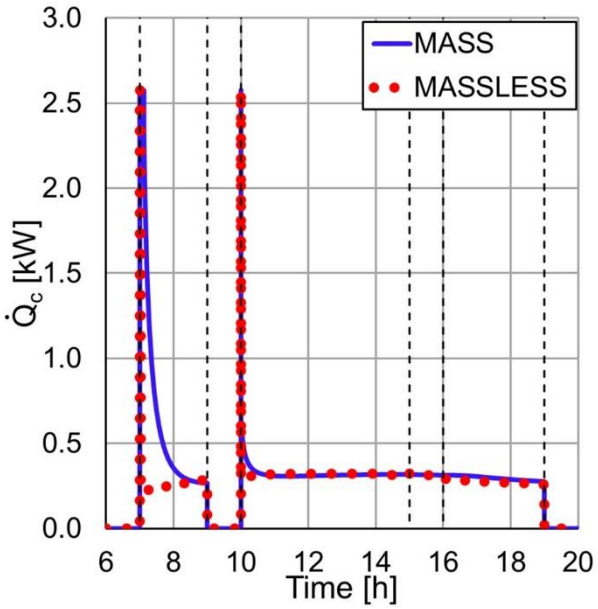

Figure 3.13 - Comparison between the demanded cooling power by the mass and massless model

Figure 3.13 provides the comparison between the cooling power required by the body truck as resulting from the mass and massless model. The main difference between the power trends can be seen during the pull-down operations: while the massless-model begins to modulate the cooling demand almost immediately, the modulation of the cooling power required by the mass-model takes about 75 minutes. This is due the fact that the mass model must also extract the heat stored into the walls and the dynamic response of the system is highly influenced by the thermal inertia, which is obviously not present on the massless-model. Consequently, the cooling energy demand resulting from a massless model will be smaller than the cooling energy demanded obtained with a model that considers the mass of the walls: in this case, it was found to be 25% lower. Simulations show that, while during the mission the cooling power required by the insulated body resulting from the two

models is pretty much the same (h.11-h.19), a huge difference between the dynamic behaviour can be noticed during the pull-down operation.

In general terms, in a complete mission analysis, the adoption of a massless model would result in neglecting pull down operations following the inactivity of the trucks, for instance during week end, or door opening in uncontrolled environment, for example for loading or unloading operations or deliveries. As the pull-down plays a major role in the total cooling energy requirement, using a massless model would lead to a significant error in the evaluation of energy consumption, making clear that the thermal mass of the walls in a transient simulation is essential.

3.3.4. Influence of the surface absorption coefficient, a_s

In order to reduce the load imposed by the solar radiation, the insulated body's external wall should be characterized by a low value of solar absorption coefficient. Ageing and soiling of the insulated body could lead some increase of this coefficient. Furthermore, branding and other non-technical motivation can lead to the choice of externally coloured surface, increasing the absorption coefficient even in brand new and clean trucks.

To study the influence of the solar absorption coefficient on the cooling demand of the insulated body, three different values were considered:

- a_s=0.15, for a clean white external surface [25].
- a_s=0.50, assumed value for a very dirty white external surface.
- a_s =0.9, assumed value for painted black external surface.

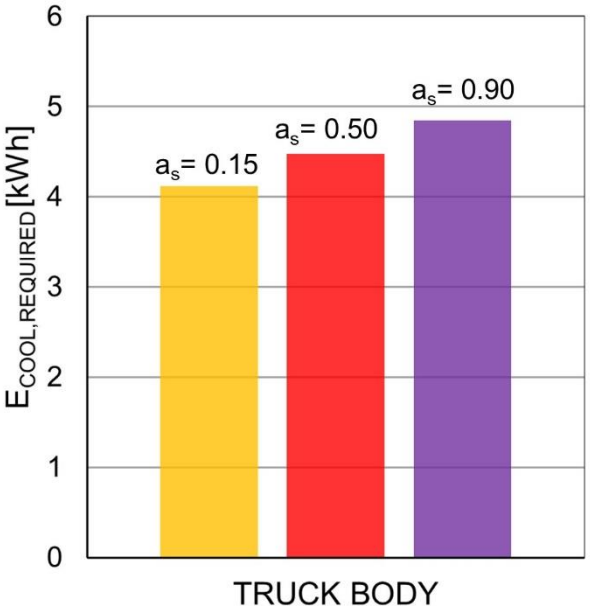

Figure 3.14 – Cooling energy demand of the insulated box during the mission for three different solar absorption coefficients

Figure 3.14 reports the trend of the cooling demand required by the insulated box to complete the considered mission for three different values of solar absorption coefficient. With a solar absorption

coefficient equal to 0.5 instead of 0.15, the cooling energy demand increases by 8% while if the solar absorption coefficient is equal to 0.9 instead of 0.15 the increase of cooling energy demand corresponds to 15%. This increase is due to the overheat of the walls during the mission caused by a higher radiation heat transfer absorbed by the wall itself.

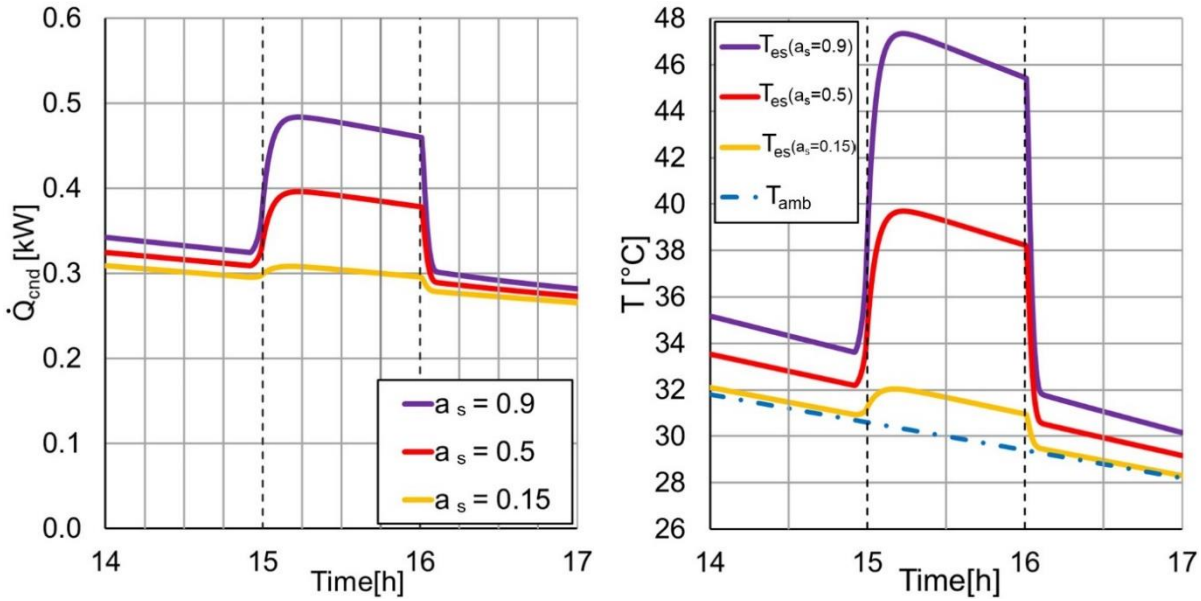

(a) (b)

Figure 3.15 - Trend during the stop time of the reference vehicle for 3 different values of solar absorption coefficient of a) conductive flux through the walls and b) external surface temperature

The overheat of the walls due to a higher value of solar absorption coefficient can be seen in Figure 3.15 for both conduction heat load and external wall temperature. When the vehicle is moving, the turbulent convective coefficient is high enough to allow an almost complete rejection of the solar heat flux to the ambient with small temperature difference ($T_{es} - T_{amb} \cong 0.3$ °C), thus reducing the impact of different radiation load on the conductive flux (Figure 3.15a for Time < 15:00 hr. and Time > 16:00 hr.). On the other hand, when the vehicle is stopped (hr. 15:00-16:00), the decrease in the convection coefficient leads to a higher overheating and higher sensitivity to the solar absorption coefficient. Due to the increase of the absorption coefficient from 0.15 to 0.9, the cooling energy increases by 8% (see Figure 3.14) but the conduction heat flowrate increases by 57% (see Figure 3.15a).

3.4. Conclusions

This chapter provides the dynamic characterization of the insulated body of a refrigerated vehicle. The experimental data collected were used to develop a 0D lumped model of the insulated body, which was used to describe the impact of the environment and mission profile on the actual cooling demand. Experimental data from ATP test were used to train the model, which was then validated with a further dataset measured during a step test.

The dynamic model is able to correctly predict the thermal response of the insulated body to an external solicitation, which is of crucial importance during the dimensioning and sizing of a cooling unit in refrigerated transport applications. The numerical model was achieved by formulating a 0-

dimensional lumped capacity method, which is one of the simplest and computationally most efficient method utilized in the study of the transient thermal behaviour. The model validation showed an excellent agreement between simulated results and experimental data, with a maximum difference in the predicted average internal temperature equal to 0.3 K.

These are the main results:

- The first important result was obtained during the numerical tuning of the dynamic model: it was found that the overall thermal capacity as well as the insulation characteristics cannot be derived from the stratigraphy of the wall: they would provide a rough approximation which can lead to significant errors. The best-fit value of thermal capacity was found to be 47% higher than the one derived from stratigraphy while the best-fit value of thermal resistance was evaluated by 23% lower than the one obtained by stratigraphy.
- The simulation model allowed to identify how the dynamic load and the mission profiles affect the actual cooling power demanded by the refrigerated space during the mission: it was possible to see that the average heat conduction through the walls of the insulated body was quite constant during the day, with a value of 300 W, while the cooling power followed it closely, except for the times when the refrigeration unit had to cool down the air inside the box and inner cladding of walls to the set value. Radiation and convection heat flowrates over the external surface of the insulated body varied significantly during the mission when the truck is moving, counterbalancing each other for the great part of the day.
- This study provided a sensitivity analysis of the model to the solar absorption coefficient a_s, by considering the simulation of the same mission with 3 different value of solar absorption coefficient for a cleaned white surface, very dirty white surface and a black painted surface. It was possible to find a maximum increment of 15% for the cooling energy demand when the external black surface body was considered. Eventually, the dependence of the model from the thermal mass of the walls was studied: results provided by a mass and a massless model were compared finding that, while the energy (power) required during the pull-down operation is much lower for a massless model, the peak of cooling demand and the mean cooling demand during the mission are pretty much the same.
- The present study suggests a first theoretical step towards a better understanding and prediction of the dynamic thermal behaviour of the insulated body of a refrigerated vehicle, which is of crucial importance to minimize the energy consumption during a mission. The method proposed in this work gives also a substantial improvement in modelling performance with a negligible increase of computer effort, since it utilizes a low-order lumped capacity method. It also evaluates the heat flowrates and the cooling energy required by the insulated body during a mission, while maintaining the set-point temperature.

In order to discuss more complex and general missions and to relate the mission profile to the cooling unit energy performance and control strategy, further development are presented in the following chapters, comprehending:

- Dynamic simulation of a cooling unit, the dynamic of the internal air as effect of the unit cycles, door opening, load lay-out and vehicle speed changes;

- Simulation of coupled heat and mass transfer phenomena during a mission, given by door opening operations in a non-controlled environment (i.e. external ambient conditions) which will cause not only a temperature variation but also a variation in relative humidity inside of the insulated truck body. This will allow to include dehumidification process on the cooling unit model

References

[1] United Nations, Agreement on the international carriage of perishable foodstuffs and on the special equipment to be used for such carriage (ATP), UNECE Transport Division, Geneva, Switzerland, 1970.

[2] C. Capo, J.M. Petit, R. Revellin, J. Bonjour, G.Cavalier, Ageing of in-service refrigerated transport vehicles: a statistical analysis, proceedings of th 25th IIR International Congress of Refrigeration, Montreal, Quebec, Canada, 2019.

[3] P.G. Jolly, C.P.Tso, Y.M. Wong, S.M Ng, Simulation and measurement on the full-load performance of a refrigeration container system in a shipping container, International Journal of Refrigeration 23(2000) 112-126.

[4] Li B, Otten R, Chandan V, Mohs WF, Berge J, Alleyne AG (2010) Optimal on-off control of refrigerated transport systems. Control Eng Pract 18(2010):1406–1417.

[5] Bin Li, Neera Jain, William F. Mohs , Scott Munns , Vikas Patnaik , Jeff Berge & Andrew G. Alleyne (2012) Dynamic modeling of refrigerated transport systems with coolingmode/heating-mode switch operations, HVAC&R Research, 18:5, 974-996.

[6] Tso C. P., Wong Y. W., Jolly P. G., and Ng S. M., 2001, “A comparison of hot-gas by-pass and suction modulation method for partial load control in refrigerated shipping containers,” Int. J. Refrig., 24, pp. 544–553.

[7] Chatzidakis, S. K., Athienitis, A. and Chatzidakis, K. S. (2004), Computational energy analysis of an innovative isothermal chamber for testing of the special equipment used in the transport of perishable products. Int. J. Energy Res., 28: 899-916.

[8] S.K. Chatzidakis, K.S. Chatzidakis, A heat transfer simulation study of a multi-compartment isothermal liquid foodstuff tank tested according to the international ATP agreement, Energy Conversion and Management 46(2) (2005) 197-221.

[9] S. Estrada-Flores, D.J. Tanner, N.D. Amos, Cold chain management during transport of perishable products, Food Australia 54(7) (2002) 268-270.

[10] N. Amos, D.J. Tanner, Temperature variability during refrigerated vessel shipment of fresh produce, in : Porceedings of the 21st International Congress Refrigeration, 2003, ICR 0250, 8 pp.

[11] D.J. Tanner, N.D. Amos, Temperature variability during shipment of fresh produce, Acta Horticulturae 599 (2003), 193-203.

[12] N.J. Smale, J. Moureh, G. Cortella, A review of numerical models of airflow in refrigerated food applications, International Journal of Refrigeration, Volume 29, Issue 6, 2006, Pages 911-930.

[13] Han, J. , Zhao, C. , Yang, X. , Qian, J. and Xing, B. (2016), Computational Fluid Dynamics Simulation to Determine Combined Mode to Conserve Energy in Refrigerated Vehicles. J Food Process Eng, 39: 186-195.

[14] James, S.J., C. James, and J.A. Evans. 2006. Modelling of food transportation systems—a review. International Journal of Refrigeration 29(6):947–57.

[15] C.P. Tso, S.C.M. Yu, H.J. Poh, P.G. Jolly, Experimental study on the heat and mass transfer characteristics in a refrigerated truck, Int J Refrigeration 25 (2002) 340-350.

[16] J. Moureh, N. Menia, D. Flick, Numerical and experimental study of airflow in a typical refrigerated truck configuration loaded with pallets, Computers and Electronics in Agriculture 34 (2002) 25-42.

[17] J. Moureh, D. Flick, Airflow pattern and temperature distribution in a typical refrigerated truck configuration loaded with pallets, International Journal of refrigeration 27 (2004) 464-474.

[18] M. Tapsoba, J.Moureh, D.Flick, Airflow pattern in an enclosure loaded with pallets: the use of air ducts, Eurotherm seminar 77, Heat and Mass transfer in Food Processing, June 20-22, Parma, Italy, 2005.

[19] Estrada-Flores, S. Evaluation of dynamic models for refrigeration system components: a thesis presented in partial fulfilment of the requirements for the degree of Doctor of Philosophy in Process and Environmental Technology at Massey University.

[20] Estrada-Flores, S., Cleland, A. C., & Cleland, D. J. (1995, August 20-25). Modelling of thermal behaviour of walls for low temperature applications: sandwich panel type. Paper presented at the 19th International Congress of Refrigeration, The Hague, Netherlands.

[21] Estrada-Flores, S. and Eddy, A. The use of thermography to aid design of refrigerated road vehicles. Proc. "Innovative Equipment and Systems for Comfort and Food Preservation", 2006. International Institute of Refrigeration. Auckland, NZ.

[22] ASHRAE. ASHRAE Fundamentals Handbook (SI), Chapter4, 2009.

[23] ASHRAE. ASHRAE handbook: HVAC applications. Atlanta (GA): ASHRAE, 1999.

[24] United States Department of Energy (DOE): EnergyPlus Engineering Reference Version 8.2: The Reference to EnergyPlus Calculations. The Reference to EnergyPlus Calculations, 2015, p.92-94.

[25] S. Rossi, P. Bison, A. Bortolin, G. Cadelano, G. Ferrarini, A. Libbra, A. Muscio. In field evaluation of the absorption coefficient of the external surface of the insulated box in a refrigerated vehicle. Proceedings of the 2nd IIR International Conference on Sustainability and the Cold Chain, Paris, April 2013.

[26] T Lafaye de Micheaux, M Ducoulombier, J Moureh, V Sartre, J Bonjour. Experimental and numerical investigation of the infiltration heat load during the opening of a refrigerated truck body. International Journal of Refrigeration, Elsevier, 2015.

[27] G.Comini, G.Cortella, O.Saro, Finite element analysis of coupled conduction and convection in refrigerated transport, International Journal of Refrigeration 18: 123-131,,1995.

[28] Energy Plus Weather Data, EnergyPlus. <https://energyplus.net/weather location/europe_wmo_region_6/GRC//GRC_Athens.167160_IWEC >.

[29] ASHRAE. 2006. Refrigeration Handbook, Chapter R09, Thermal properties of foods. Atalanta, GA, USA: American Society of Heating, Refrigerating and Air-Conditioning Engineers.

[30] Harris, M. B., Carson, J. K., Willix, J., & Lovatt, S. J. (2004). Local surface heat transfer coefficients on a model lamb carcass. Journal of Food Engineering, 61, 421-429.

[31] Carrier. Light commercial vehicle refrigeration unit < https://www.carrier.com/truck-trailer/en/it/products/it-truck-trailer/lcv/pulsor-300/> , 2018, p.1.

4. Development of a new cooling unit using CO_2 as the working fluid for refrigerated transport application

In this chapter, a preliminary evaluation of the theoretical performance of a new cooling unit which utilizes carbon dioxide as the working fluid is provided. After the introduction of the cooling unit's operating scheme, which can operate according to a classical low pressure receiver cycle, an ejector cycle and an ejector cycle using an auxiliary evaporator, a numerical model is developed with the software MATLAB to assess the performance of the system operating in steady state condition. To evaluate the performance of the system with a more accurate numerical model able to simulate the operation of the system even in dynamic conditions, the software AMESim was utilized to develop a new numerical model the refrigerating system.

4.1. The use of carbon dioxide in refrigerated transport

The choice of refrigerant in refrigerated transport cooling systems is undergoing a though revision, as an indirect consequence of the phase down of synthetics refrigerants imposed by the F-gas regulation. R-404A and R-134a, which are synthetic refrigerants traditionally used in truck and trailer cooling units [1], are likely to be phased out almost completely in all commercial applications as part of the service ban. As the global warming gains relevance, efforts towards developing environmentally friendly refrigeration solutions are constantly taking place. CO_2, as a non-toxic and non-flammable refrigerant, is a promising substitute due to its low GWP but, with a critical temperature of only 30.9 °C, transcritical operation is necessary for adequate heat rejection to the ambient air in hot climates. Working across the critical point implies high thermodynamic losses, which consequently lower the COP, and makes the technology sensitive to the discharge pressures at high ambient temperature [2]. As the transcritical cycle involves large throttling losses, in recent years many improvements have been implemented in CO_2 system, including parallel compression, heat recovery and use of two-phase ejectors for expansion work recovery [3] since the high working pressures and in particular the high pressure differences between the heat absorption and heat rejection sides make R744 an ideal fluid for expansion work recovery. The use of CO_2, according to transcritical cycles when required by heat sink temperature, has been widely and successfully applied to heat pumps and commercial refrigeration system in the last twenty years ([4],[5]).

Numerical modelling offers an economic alternative to experiments and provides a reliable tool in energy system design, from evaluating and optimizing the system response to the development and testing of different control strategies. Dynamic simulation is an efficient approach to study the transient performance and optimize the structural parameters of the system as well as operation conditions while steady state simulations put particular emphasis on static parameters such as cooling capacity and COP. Generally, transient models can be categorized into two classes: inductive and deductive models [6]. The inductive models are based on a mathematical relation between the input and output variables of the system while deductive models are based on conservation equations of mass, momentum and energy and can be classified as global models and discretized models. In a dynamic model of a refrigerating system, the numerical model of the compressor and expansion valve is typically obtained with algebraic equations determined with inductive models; The numerical model

of the heat exchangers is instead achieved using a finite-volume distributed parameter or a moving-boundary lumped-parameters approach [7].

Literature review shows that several authors developed dynamic or steady-state numerical models to evaluate the performance of a refrigerating unit operating with CO_2 as the working fluid. Rasmussen (2002) [8] presented a model of a transcritical CO_2 vapor compression cycle: the system presented consisted of a gas-cooler, an evaporator, an internal heat exchanger, an expansion valve and a reciprocating compressor. The expansion valve and compressor were modelled with algebraic relations, while the heat exchangers were modelled with the moving-boundary lumped-parameters approach. An experimental facility was set up to validate the dynamic model and the simulations results resulted in having a good agreement with the experimental data, showing that the transient behaviour could be accurately estimated by the proposed dynamic model. Minetto (2011) [9] presented a study of a heat pump system used for residential hot water heating featuring two finned coil evaporators connected in parallel. A model was set up to determine the optimum gas cooler pressure for a constant water delivery temperature by varying the air inlet temperature between -5 °C and 25 °C, proving that the overall heat pump model accurately predicted the experimental results. Shi et al. (2010) [10] developed a dynamic model of a transcritical CO_2 cooling unit using the commercial software *Dymola* to assess the system performance in the absence of physical prototypes.

Litterature review shows that is possible to find very few studies on numerical model predicting the performance of a CO_2 refrigerating system for refrigerated transport application: Lawrence et al.(2018) [11] developed a numerical model, using the software EES, to predict the performance of a transcritical CO_2, multi-temperature, mobile refrigerated container system. The model was developed to investigate the application of CO_2 ejector technology to smaller-scale system and the system performance was simulated at very harsh working conditions (ambient temperature of 57 °C and -20°C for the lower temperature evaporator air). The numerical model was first utilized to compare the performance of a conventional direct expansion booster cycle using all microchannel finned coil heat exchangers with the same cycle using all round-tube plate fins heat exchanger instead, showing an increase of 6.2% of COP when the microchannel heat exchangers were implemented. After that, the performance of the system utilizing an internal heat exchanger and a two-phase ejector was simulated, finding a 68.6% improvement in COP compared to a classical direct expansion cycle operating at the same harsh conditions. Their system, however, was developed for refrigerated containers in military application, which are typically employed for ship or rail based refrigerated transport or can be stored for an extended period.

The system presented in this chapter is developed for road refrigerated transport: developing a cooling unit for this application can be challenging, as the relatively small cooling power requested might inhibit the application of complex solutions utilized by commercial refrigeration as they lose the cost-effectiveness due to the reduced scale. In addition, the unit weight is a key parameter for the technology acceptance in road transport.

4.2. System layout

The system presented in this study (Figure 4.1) is mainly designed to extract heat from the cargo space of a refrigerated vehicle and reject it to the external environment: depending on the ambient

temperature, T_{amb}, the system can operate in both subcritical and transcritical mode. Furthermore, beside maintaining a correct set-point temperature even in cold climate and satisfying the requirement of defrost operation which is needed in the case of below zero evaporation temperature, the system is also able to provide heat to the cargo space (working as a heat pump).

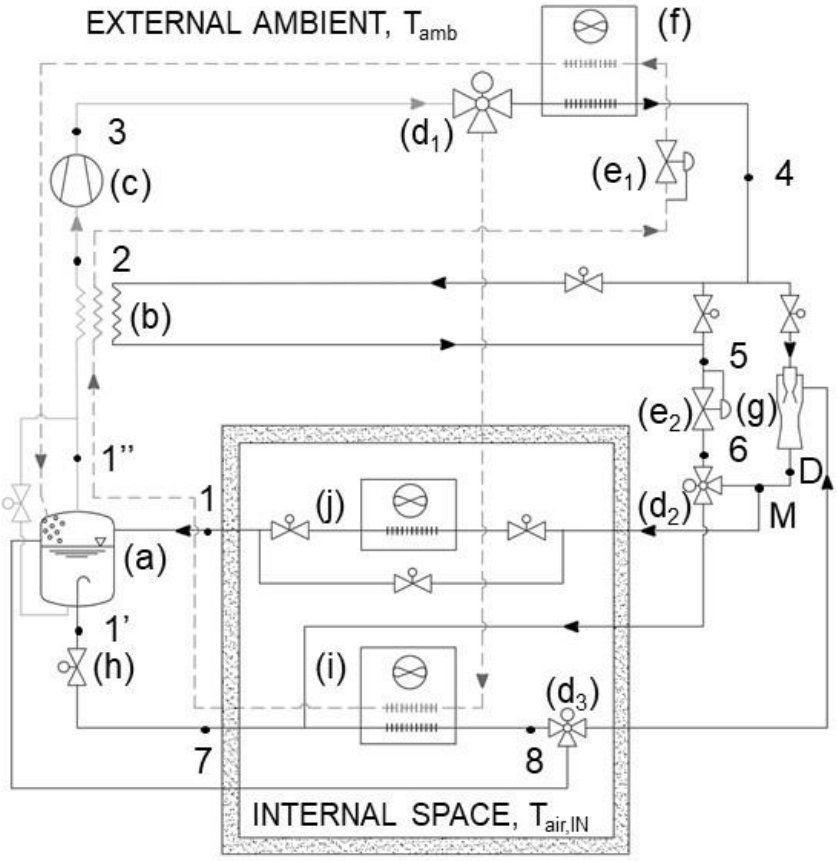

Figure 4.1 - Schematic of the setup. ——Refrigerant flow in both cooling and heating mode ——Refrigerant flow in cooling mode - - - - -Refrigerant flow in heating mode

The main components of the system are: a liquid-vapor separator (a), a regenerative heat exchanger (b), a semi-hermetic compressor (c), two three-way valves (d_1,d_2), two expansion/back pressure valves (e_1,e_2), a finned-coil gas-cooler/condenser (f), a fixed-geometry two-phase ejector (g), a manual expansion valve (h) and two finned-coil evaporators (i,j). The system is also provided of several circulation valves allowing to modify the path of the refrigerant flow to switch between operating configurations. The geometric dimensions of the main components of the system are reported in Table 4.1.

Table 4.1 – System component sizing at the nominal condition: T_{eva} =-5 °C, $T_{gc\text{-}out}$ = 33°C, $T_{air,IN}$ = 0°C

Component	Dimensions
Semi-hermetic compressor	Swept volume, $\dot{V}_s = 2.39\ m^3h^{-1}$
Finned coil evaporator	$A_e = 36.4\ m^2$, $\dot{m}_{air} = 4800\ m^3h^{-1}$, $\dot{Q}_{eva,nom} = 10\ kW$
Regenerative heat exchanger	$A = 0.39\ m^2$, $\dot{Q}_{IHX,nom} = 3\ kW$
Two-phase ejector	nozzle throat diameter $d_{th} = 1\ mm$, VEJ1 [12]

4.3. **Cooling mode**

In cooling mode operation, the cooling unit can operate in three different configurations: according a traditional cycle using a back-pressure valve for expansion (see section 4.3.1) and according to an ejector cycle, using the parallel between a back-pressure valve and a fixed geometry two phase ejector for expansion work recovery (see section 4.3.2). The ejector cycle can be further modified and include the use of an auxiliary evaporator in the line between the outlet of the expansion devices and the liquid-vapour separator (see section 4.3.3), providing the last operating configuration.

4.3.1. Operation according to the traditional cycle

The reference is a traditional Low Pressure Receiver (LPR) cycle: the refrigerant in the state of saturated vapor (1”) is drawn from the liquid-vapour separator and superheated in the regenerative heat exchanger (2) before being compressed in the semi-hermetic compressor. After leaving the semi-hermetic compressor (3), the carbon dioxide is cooled first in the gas-cooler/condenser (4) and later in the regenerative heat exchanger (4). The refrigerant is then expanded to the evaporation pressure by the back-pressure valve and the resulting two-phase mixture (7) is then diverted to the fin and tube evaporator by means of a three-way where evaporates before entering the liquid-vapor separator by another three-way valve.

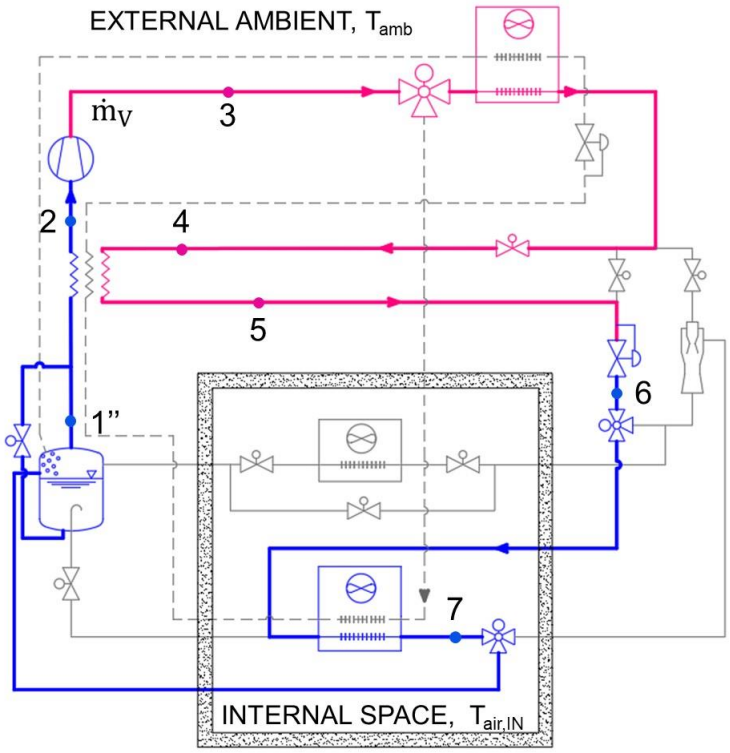

Figure 4.2 – Configuration of the refrigerating system operating in cooling mode according to a traditional cycle configuration

4.3.2. Operation according to the ejector-expansion cycle

In the ejector-expansion transcritical cycle configuration, reported in Figure 4.3, the refrigerant in the state of saturated vapor (1") is drawn from the liquid-vapor separator and is compressed (3) in the semi-hermetic compressor; no superheat takes place in the regenerative heat exchanger, as the refrigerant flow in the high pressure side is inhibited. After the compression, the refrigerant is cooled down (4) in the gas-cooler/condenser. Since the two-phase ejector operates with a fixed geometry, a by-pass branch with an expansion/back-pressure valve is provided, in the case the mass flowrate leaving the gas-cooler/condenser $\dot{m}_V$ exceeds the mass flow rate at the ejector motive nozzle $\dot{m}_{EJ}$. The mass flow rate at the outlet of the ejector $\dot{m}_E$ and mass flow rate leaving the expansion/back-pressure valve (6), $\dot{m}_{BP}$, are then mixed together (M) before the resulting two-phase mixture is returned in the liquid-vapor separator (1), bypassing the auxiliary evaporator. On the other hand, the saturated liquid (1') extracted from the liquid-vapor separator is expanded (7) by means of a manual throttling valve and the two-phase mixture evaporates to the state of superheated vapor (8) flowing in the finned coil evaporator heat exchanger coils, before entering the ejector suction nozzle. As the evaporation pressure can be manually set by means of the manual throttling valve, this cycle presents a degree to optimize the system's performance.

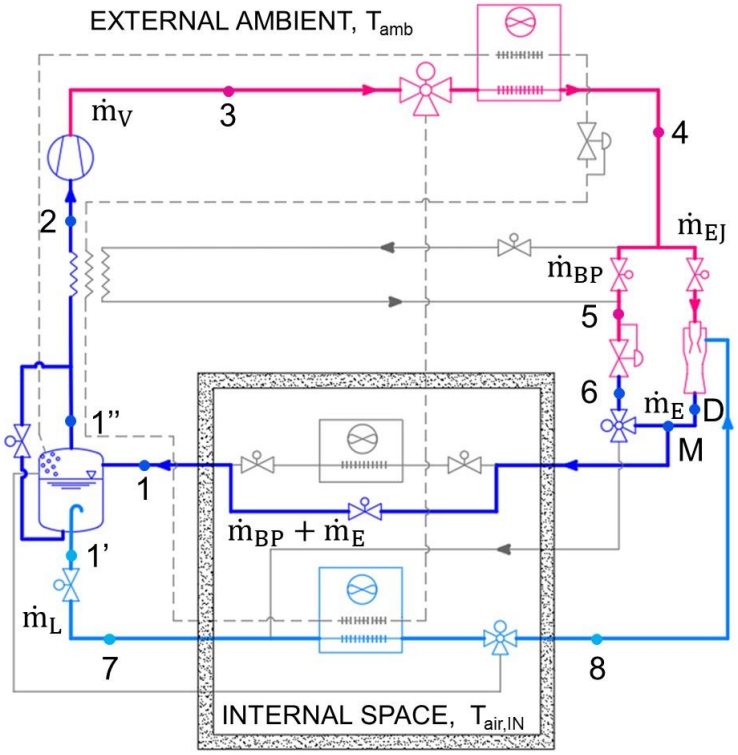

Figure 4.3 - Configuration of the refrigerating system operating in cooling mode according to an ejector cycle configuration with a single evaporator

4.3.3. Operation according to the ejector expansion cycle using the auxiliary evaporator

The ejector configuration using the auxiliary evaporator schematic is reported in Figure 4.4. The operation of this cycle is similar to the one using a single evaporator, however, in this configuration the two-phase mixture at the outlet of the expansion devices (M) enters the finned-coil evaporator previously by-passed. The auxiliary finned-coil evaporator evaporates the two-phase mixture from the vapour quality x_M to the vapour quality x_1 required by the liquid-vapour separator: the system is then allowed to find a different operating condition depending on the heat exchanger's performance, providing a second degree of freedom to optimize the system in addition to the set-point of the manual throttling valve in the liquid line.

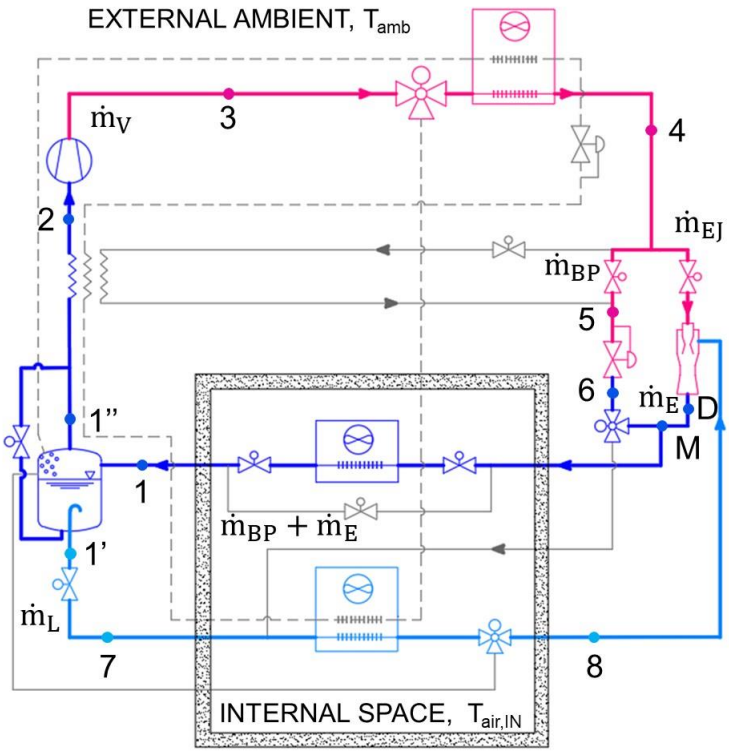

Figure 4.4 - Configuration of the refrigerating system operating in cooling mode according to an ejector cycle configuration using an auxiliary evaporator

4.4. **Heating mode**

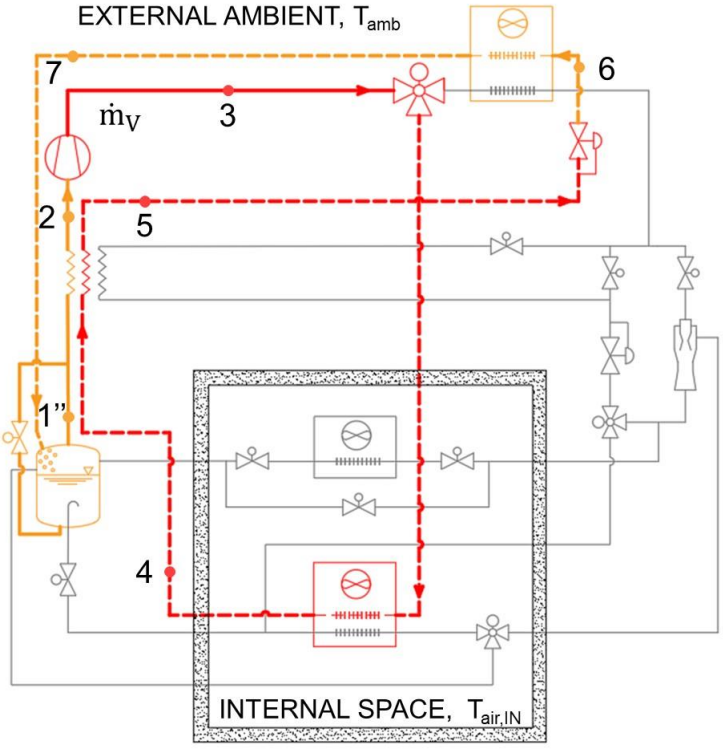

Figure 4.5 - Configuration of the refrigerating system operating in heating mode according to a heat pump configuration

In the heating mode operation, the refrigerant in the state of saturated vapour (1”) enters the suction line of the compressor and is superheated (2) in the regenerative heat exchanger before being compressed in the semi-hermetic compressor (3). After that, through the 3-way valve, the refrigerant flows in the heating line and enters in the finned-tube evaporator, now functioning as a gas-cooler/condenser and rejects heat to the cargo space. After being cooled down (4), the refrigerant flows in the regenerative heat exchanger and is additionally cooled down (5) before the refrigerant is expanded in the expansion/back-pressure valve (6). The two-phase mixture then enters the gas-cooler/condenser, now functioning as an evaporator, before the superheated vapour is directed back in the liquid-vapor separator (7).

4.5. Numerical model of the refrigerating system using the software MATLAB

Despite being able to operate in both heating and cooling mode, as previously discussed, the thermal performance of the system is evaluated only in cooling mode as it represents the main operation mode in refrigerated transport application.

A numerical model of the refrigerating system operating in steady state condition is developed with the software MATLAB: thermophysical properties of CO_2 and air, assumed to be in dry state, are evaluated with REFPROP. Localized and distributed pressure losses of the air and the refrigerant flowing throughout the pipes of the system are neglected as well as heat losses from the system to the external environment, except the heat rejection in the gas-cooler/condenser. Expansion processes at the back-pressure/expansion valves and throttling valve are considered isenthalpic and the presence of oil blending with the refrigerant is neglected.

The numerical model of the semi-hermetic compressor is obtained with empirical correlations: the values of volumetric efficiency η_V and overall compression efficiency η_C are deriverd from the compressor data supplied by its manufacturer, Dorin CD 360 H, (Figure 4.6) and are used to compute the value of mass flow rate developed by the compressor $\dot{m}_V$ and electric power draw P_{el}.

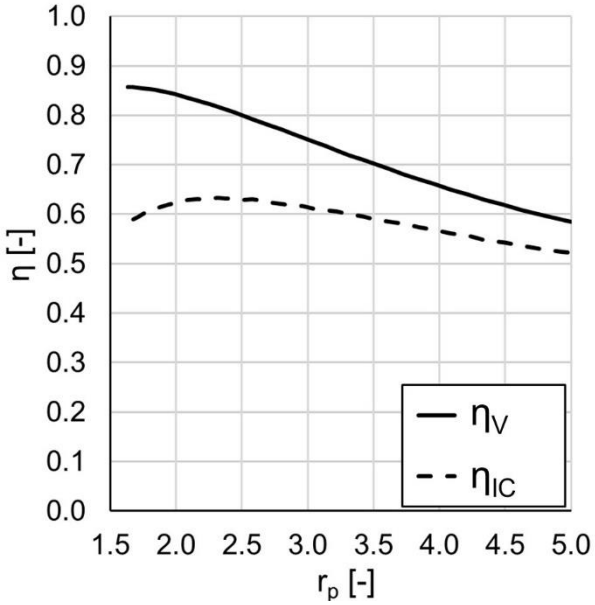

Figure 4.6 – Trend of volumetric efficiency and overall compression efficiency of the semi-hermetic compressor as a function of pressure ratio

The value of the mass flow rate developed by the compressor (Eq. 4.1) and the value of electric power draw (Eq. 4.2) are expressed as a function of the operating conditions alone (compressor inlet conditions and pressure ratio r_p), since the compressor works at fixed speed.

$$\dot{m}_V = \rho_{IN} \dot{V}_s \eta_V \tag{4.1}$$

$$P_{el} = \dot{m}_V \frac{\Delta h_{IS}}{\eta_C} \tag{4.2}$$

The gas-cooler/condenser is considered an ideal heat exchanger with continuous regulation, thus the refrigerant outlet temperature $T_{g-c,out}$ and operative high-pressure p_{g-c} are defined as a function of external temperature T_{amb}, in accordance with Dugaria et al.(2018) [13] in three working zone: subcritical, transcritical and supercritical. When T_{amb} is lower than 17 °C, the system operates in subcritical mode and the refrigerant temperature at the outlet of the condenser is evaluated assuming 7 K as approach point temperature difference ΔT_{ap} (between CO_2 at the outlet and air inlet) and a subcooling ΔT_{sc} of 3 K. Above the ambient temperature T_{amb} of 27 °C, $T_{g-c,out}$ is calculated started from T_{amb} assuming a ΔT_{ap} of 3 K and the high pressure p_{g-c} is optimized in order to obtain the maximum COP of the refrigeration system, in accordance with the study of Chen et al.(2005)[14]. Between 17 °C and 27 °C temperature, $T_{g-c,out}$ and pressure p_{g-c} are defined to provide a smooth transition between the two control logics.

The two-phase ejector performance is modelled in accordance with the study of Banasiak el al. (2015)[12], which provides the performance mapping for a fixed-geometry vapor ejector and corresponding interpolation functions. Motive nozzle mass flow rate $\dot{m}_{EJ}$ and ejector entrainment ratio, which is defined as the ratio between the suction nozzle mass flowrate $\dot{m}_L$ and the motive nozzle mass flow rate [12] ($\phi = \dot{m}_L / \dot{m}_{EJ}$), are expressed as function of motive nozzle inlet pressure and density, suction nozzle inlet pression and ejector outlet pressure.

The simulation of fin-and-tube evaporator is achieved with a macroscopic model which aims to determine the total capacity of coil, as introduced by Jolly et al. (2000) [15]. The evaporator coil is approximated to a counter-flow heat exchanger and the total heat transfer area is divided into a two-phase region ($A_{e,2ph}$) and a superheated region ($A_{e,sh}$), as reported in Figure 4.7a.

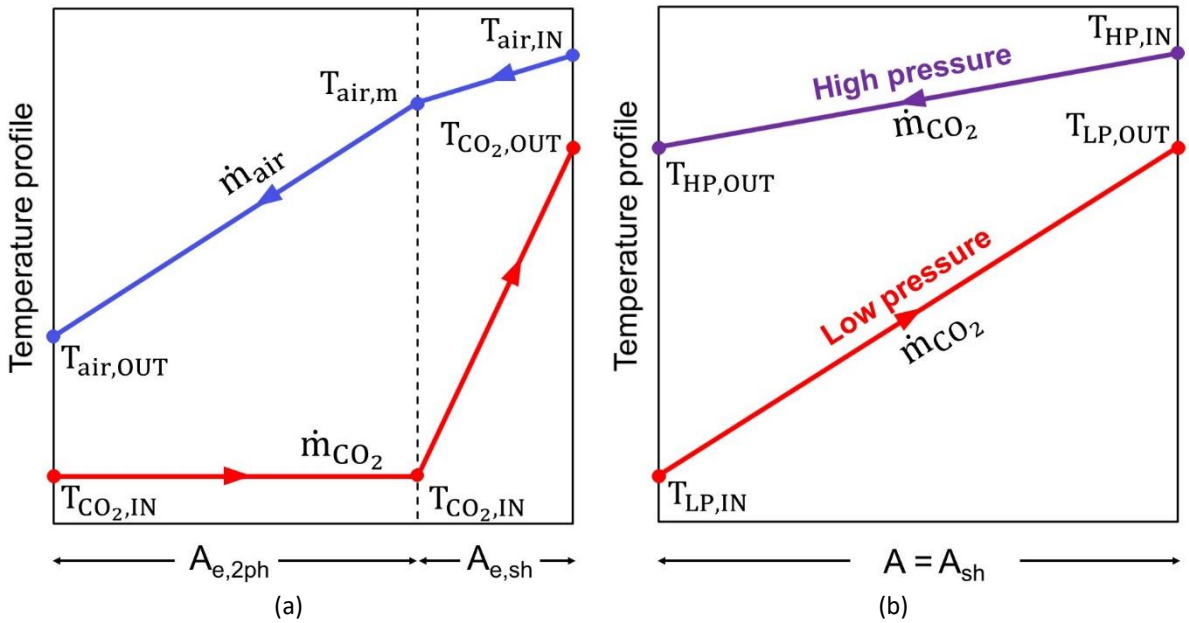

Figure 4.7 – Subdivision of the total heat transfer area according to (a) evaporator heat exchanger model (b) regenerative heat exchanger model

The input required to the coil model are the evaporator heat transfer area A_e, the overall heat transfer coefficient at the two-phase region $K_{e,2ph}$, the overall heat transfer coefficient at the superheated region $K_{e,sh}$, the mass flow rate of refrigerant $\dot{m}_{co_2}$, the mass flow rate of air $\dot{m}_{air}$, thermophysical properties of the two fluids at the inlet of the heat exchanger. The governing equations of the heat exchanger's macroscopic model (Eq. 4.3-4.8) are solved under the constraints of $A_e = A_{e,2ph} + A_{e,sh}$.

In the two-phase region, assuming a constant evaporation temperature due to the neglect of pressure losses, the heat gain by the refrigerant, $\dot{Q}_{eva,2ph}$, is given by Eq. 4.3.

$$\dot{Q}_{eva,2ph} = K_{e,2ph} A_{e,2ph} \frac{T_{am} - T_{air,OUT}}{\log\left(\frac{T_{air,m} - T_{CO_2,IN}}{T_{air,OUT} - T_{CO_2,IN}}\right)} \tag{4.3}$$

The heat gain by the refrigerant in the two-phase region is also be expressed by Eq. 4.4

$$\dot{Q}_{eva,2ph} = \dot{m}_{CO_2}\left(h_{SV}\left(T_{CO_2,IN}\right) - h_{CO_2,IN}\right) \tag{4.4}$$

While the heat loss by the air in the two-phase region is given by Eq. 4.5.

$$\dot{Q}_{eva,2ph} = \dot{m}_{air}\left(h_{air,m} - h_{air,OUT}\right) \tag{4.5}$$

Similarly, in the superheat region, the heat gain by the refrigerant, $\dot{Q}_{eva,sh}$, is given by Eq. 4.6.

$$\dot{Q}_{eva,sh} = K_{e,sh} A_{e,sh} \frac{(T_{air,IN} - T_{CO_2,OUT}) - (T_{air,m} - T_{CO_2,IN})}{\log\left(\frac{T_{air,IN} - T_{CO_2,OUT}}{T_{air,m} - T_{CO_2,IN}}\right)} \quad (4.6)$$

And the heat gain by the refrigerant in the superheat region is then also expressed by Eq. 4.7

$$\dot{Q}_{eva,sh} = \dot{m}_{CO_2}(h_{CO_2,OUT} - h_{SV}(T_{CO_2,IN})) \quad (4.7)$$

While the heat loss by the air in the superheat region is given by Eq. 4.8.

$$\dot{Q}_{eva,sh} = \dot{m}_{air}(h_{air,IN} - h_{air,m}) \quad (4.8)$$

The total capacity of the coil is then given by the sum of the refrigerating capacity evaluated in the two-phase region and the refrigerating capacity evaluated in superheat region, according to Eq. 4.9:

$$\dot{Q}_{eva} = \dot{Q}_{eva,2ph} + \dot{Q}_{eva,sh} \quad (4.9)$$

The evaporator model's outputs are the state of the air and the refrigerant at the outlet of the heat exchanger, the ratio between the two-phase and the single-phase areas and the overall capacity $\dot{Q}_{eva}$. The simulation of the regenerative heat exchanger is performed with the same approach, considering a null two-phase area, as the refrigerant at the inlet of the heat exchanger is already in the state of saturated vapor. In the heat exchanger model, the air side heat transfer coefficient is calculated based on the proposal of McQuiston et al. (1981) [16], while the refrigerant side heat transfer coefficient in the two-phase region is calculated from Chen's et al. (1963) [17] correlation and in the single-phase flow region Dittus-Boelter (1987) [18] correlation.

4.5.1. Simulation of the traditional cycle

Figure 4.8 provides the flowchart of the numerical model of the system operating in cooling mode according to the traditional low-pressure receiver cycle. In the numerical model of this cycle, the condition of steady state condition is derived from mass and energy conservation equation in the liquid-vapour separator, which is given by Eq. 4.10:

$$\frac{dE}{dt} = \dot{m}_V h_7 - \dot{m}_V h_{SV} - \dot{m}_R h_{SL} \quad (4.10)$$

Where $\dot{m}_R$ is the mass of saturated liquid flowing in the recirculation branch, designed to ensure the oil return at the compressor. For the sake of simplicity no recirulated mass flow rate is assumed ($\dot{m}_R = 0$) thus the steady state condition, $dE/dt = 0$, is achieved with the condition $h_7 = h_{SV}$ which equals to saturated conditions at the evaporator outlet. The condition of unitary vapor quality at the outlet of the evaporator coil then represents the constrain while the evaporation pressure can change in order for the system to be in steady state condition. Once the ambient temperature T_{amb} is given, the high-pressure value p_{g-c} and refrigerant temperature $T_{g-c,out}$ at the point 4 at the outlet of the gas-cooler/condenser are computed. After that, the model performs a first guess of the evaporation

pressure p_{eva}, identifying the point 1" of saturated vapor. The knowledge of the state 1" at the inlet of the regenerative heat exchanger, allows the evaluation of the state 2, state 5 and performance parameter $\dot{Q}_{IHX}$, ε_{IHX} through the regenerative heat exchanger model. After the identification of the state 2, the compressor model provides the evaluation of the state 3, mass flow rate $\dot{m}_V$ and electric power draw P_{el} according to Eq. 4.1 and Eq. 4.2: Point 6 is then determined, setting the same specific enthalpy as point 5 but a different pressure (p_{eva}). The evaporator model provides the refrigerating capacity $\dot{Q}_{eva}$, the outlet air temperature $T_{air,OUT}$ and the state of the refrigerant at the outlet of the evaporator (point 8) given the inlet conditions of both refrigerant and air. The outlet vapor quality is then compared to the saturation condition imposed by the stationary hypothesis, and the evaporation pressure p_{eva} corrected accordingly until convergence criteria are met. The COP of the system is then defined as the ratio between the refrigerating capacity provided by the evaporator and the electric power draw at the compressor, according to Eq. 4.11:

$$COP = \frac{\dot{Q}_{eva,}}{P_{el}} \tag{4.11}$$

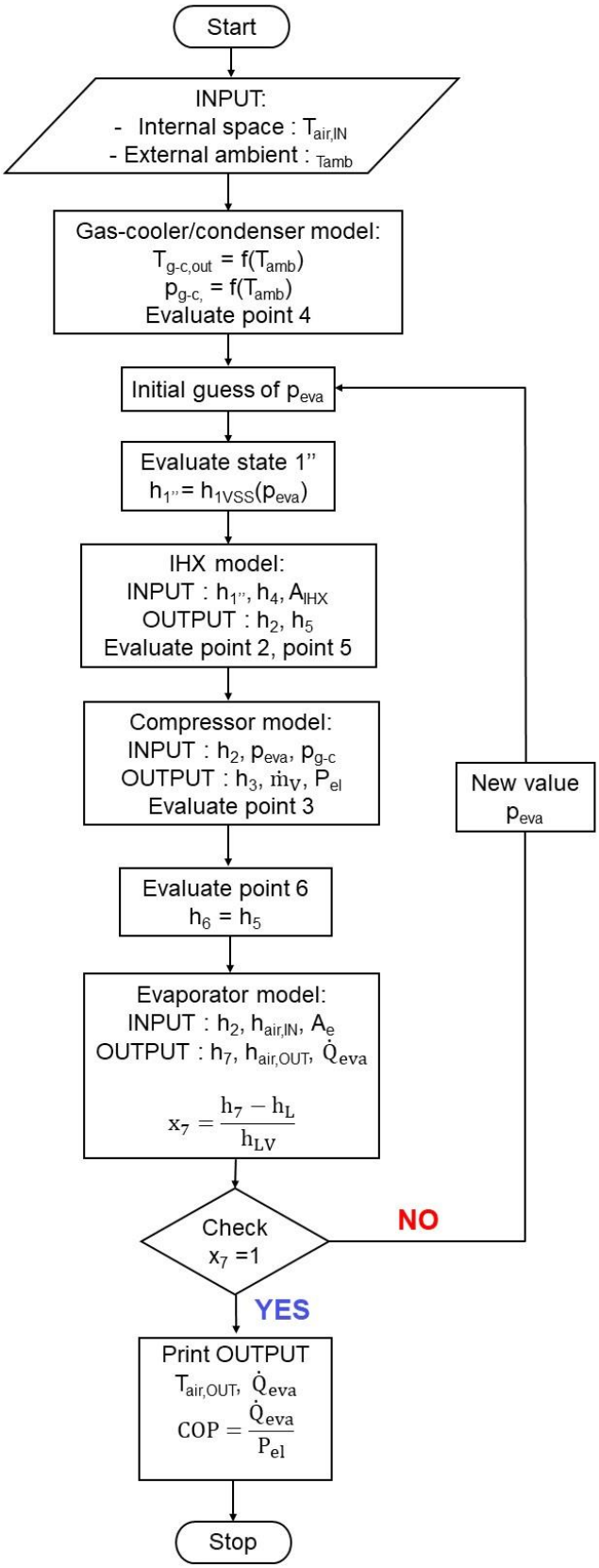

Figure 4.8 – Flowchart of the numerical model of the traditional cycle configuration

4.5.2. Simulation of the ejector cycle with a single evaporator

In the numerical model of this cycle, the evaporation pressure p_{eva} and the receiver pressure $p_{receiver}$ are different and the first can be set through a manual throttling valve located between 1' and 7. The steady state condition can be expressed as previously by means of the liquid-vapor separator equilibrium. Once T_{amb} is decided, the model identifies the value of the high-pressure p_{g-c} and point 4 at the outlet of the gas-cooler/condenser. In this configuration, the regenerative heat exchanger is bypassed, according to the findings of Elbel et al. (2004) [19]. A first guess of the liquid-vapor separator pressure is performed and point 1',1" of saturated liquid and vapour conditions are computed. Since there is not superheating in the regenerative heat exchanger, point 2 is equal to point 1" at the inlet of the compressor, allowing the evaluation of mass flow rate $\dot{m}_V$, electric power draw P_{el} and state 3 through its model (Eq. 4.1-Eq. 4.2). Since all the input necessary to the two-phase ejector model are now known, mass flow rate at the motive nozzle $\dot{m}_{EJ}$ and entrainment ratio ϕ are calculated. The mass flow rate at the suction nozzle is evaluated trough the definition of entrainment ratio (Ebel S., Hrnjak P. 2008 [20]), being equal to $\dot{m}_L = \phi\, \dot{m}_{EJ}$. State 7 at the inlet of the evaporator is determined with an isenthalpic transformation from point 1' and thus through the evaporator model $\dot{Q}_{eva}$ and evaporator outlet state 8 are obtained. At this point, since the ejector has fixed geometry, if the mass flow rate developed by the semi-hermetic compressor $\dot{m}_V$ exceeds the value of the mass flow rate at the motive nozzle of the ejector $\dot{m}_{EJ}$, the exceeding mass flow rate $\dot{m}_{BP} = \dot{m}_V - \dot{m}_{EJ}$ is by-passed to the back-pressure/expansion valve. The outlet conditions (point D) of the ejector are decided by Eq. 4.12, obtained by the coupling of mass and energy conservation law:

$$h_D = \frac{h_4 + \phi h_8}{1+\phi} \tag{4.12}$$

After that, the mass flow rate at the outlet of the back-pressure valve (state 6) is mixed with the mass flowrate at the outlet of the ejector $\dot{m}_E = \dot{m}_{EJ} + \dot{m}_L$ (state D) and mass an energy conservation balance is formulated, obtaining the state M and thus the vapor quality of the resulting two-phase mixture x_M. At the same time, the vapor quality x_1, required to achieve the mass conservation in the liquid-vapor separator (Eq. 4.13) between the lines 1, 1' and 1" can be expressed as:

$$x_1 = \frac{1}{1+\frac{\dot{m}_L}{\dot{m}_{EJ}}\phi} \tag{4.13}$$

The trend of the quality x_1 and x_M as a function of the receiver temperature is presented in Figure 4.10. As the auxiliary evaporator is bypassed in this configuration, the constraint $x_M = x_1$ has to be enforced to reach the steady condition. Then, the error between the computed value x_M and the expeced equilibrium value x_1 is used to correct the initial guess on the receiver pressure, converging to the solution by means of interative calculation (see flowchart in Figure 4.9). The COP of the system is then given by the same definition provided in Eq. 4.11.

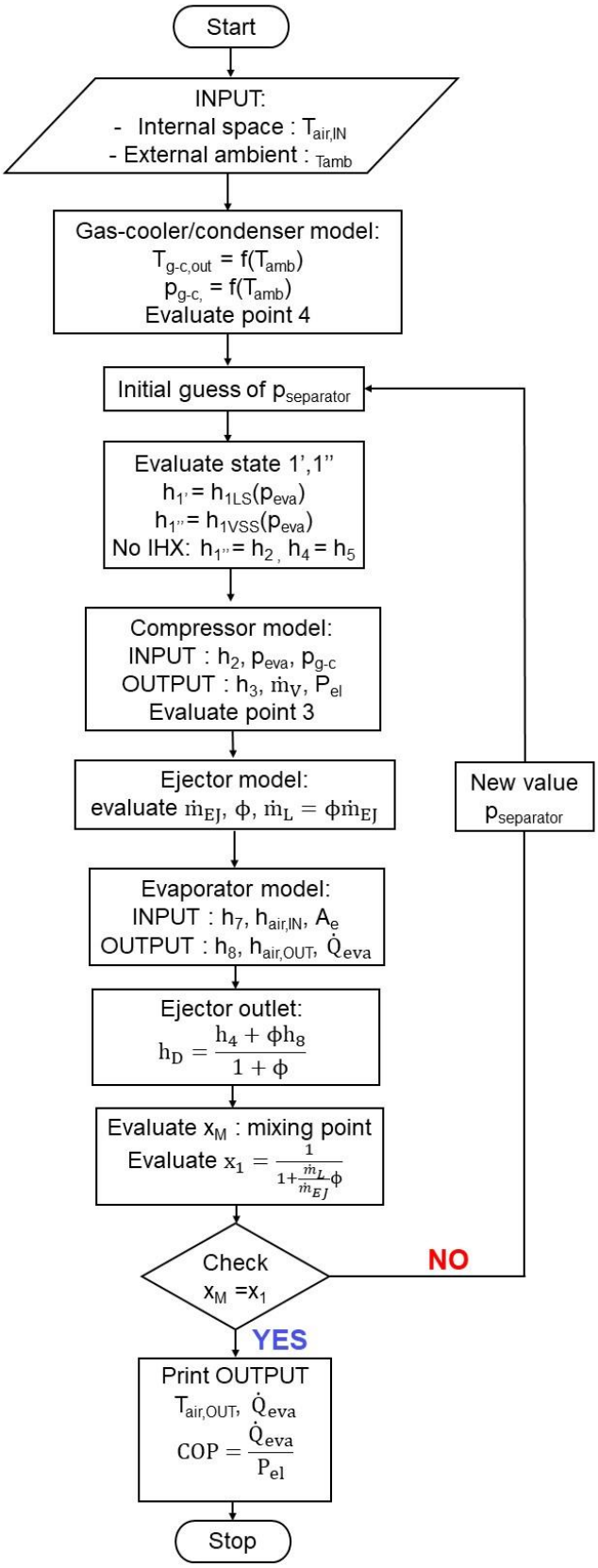

Figure 4.9 – Flowchart of the numerical model of the ejector cycle configuration

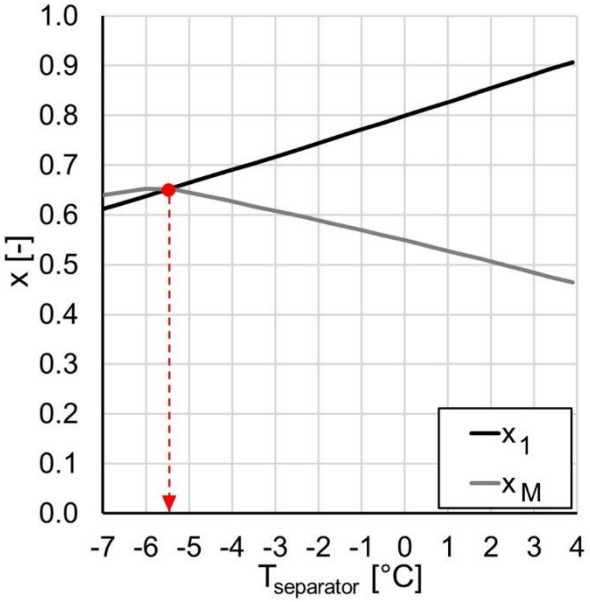

Figure 4.10 – Trend of the vapour quality x_1 and x_M as a function of the separator operating temperature and identification of the steady state working point

4.5.3. Simulation of the ejector cycle using the auxiliary evaporator

The simulation of the ejector cycle is achieved with the same numerical model of the ejector cycle using a single evaporator. The simulation of the auxiliary evaporator, however, is not achieved using the numerical model of the evaporator. Instead, the cooling capacity provided by the auxiliary evaporator, $\dot{Q}_{AUX}$, and the air outlet temperature, $T_{air,OUT,AUX}$ are evaluated using the mean logarithmic temperature difference method and the first law of thermodynamics according to Eq. 4.14 and 4.15.

$$\dot{Q}_{AUX} = (\dot{m}_E + \dot{m}_{BP}) h_{LV} (x_1 - x_M) \tag{4.14}$$

$$\dot{Q}_{AUX} = KS_{AUX} \Delta T_{ml,AUX} \tag{4.15}$$

Where h_{LV} is the vaporization specific heat evaluated at the liquid-vapour separator operating temperature, which equals to the auxiliary evaporator's evaporation temperature as pressure losses are neglected. The heat gain by the refrigerant $\dot{Q}_{AUX}$ in the auxiliary evaporator, ensures the vapour quality increase from the value x_M to the value required by the liquid-vapour separator to reach steady state condition x_1. Depending on the geometrical features of the auxiliary evaporator (i.e. KS_{AUX}), the working temperature (and thus pressure) of the separator obtained in the ejector cycle, can be increased up to a maximum given by the evaporator's inlet air temperature $T_{air,IN}$.

The coefficient of performance of the refrigerating system operating in this configuration is then given considering the total refrigerating capacity given by both evaporators, according to Eq. 4.16:

$$COP_{EJ\ AUX} = \frac{\dot{Q}_{eva} + \dot{Q}_{AUX}}{P_{el}} \tag{4.16}$$

4.6. Numerical results of the model developed with the software MATLAB

In the refrigerated transport industry, the test conditions for measuring the effective refrigerating capacity of a cooling unit are defined by the ATP regulation [21]. According ATP, in order to measure the effective refrigerating capacity of a 0° C class refrigerated vehicle, the internal cargo space temperature and external ambient temperature must be maintained at -2 °C and 30 °C respectively.

In this section, the thermal performance of the system will be evaluated at -2 °C for the air entering the evaporator coil and 30 °C for the inlet air to the gas-cooler/condenser. However, due to the high variability of the external environment condition in refrigerated transport conditions, a range of external ambient temperature will be considered as well.

4.6.1. Traditional cycle configuration

For this configuration, assumed as reference for the refrigerating system, the numerical model assessed for evaporator inlet air temperature equal to -2 °C and gas-cooler/condenser inlet air temperature (i.e. external ambient temperature T_{amb}) equal to 30 °C, as prescribed by the ATP regulation, a refrigerating capacity of the system $\dot{Q}_{eva}$ equal to 5.49 kW, an electric power draw at the semi-hermetic compressor P_{el} equal to 2.80 kW, corresponding thus to a coefficient of performance $COP = 1.96$. The p-h diagram of the refrigerating system operating at the reference conditions according to the traditional cycle and the trend of refrigerating capacity and COP with a varying ambient temperature and a fixed evaporator air inlet temperature (-2 °C) are provided in Figure 4.12.

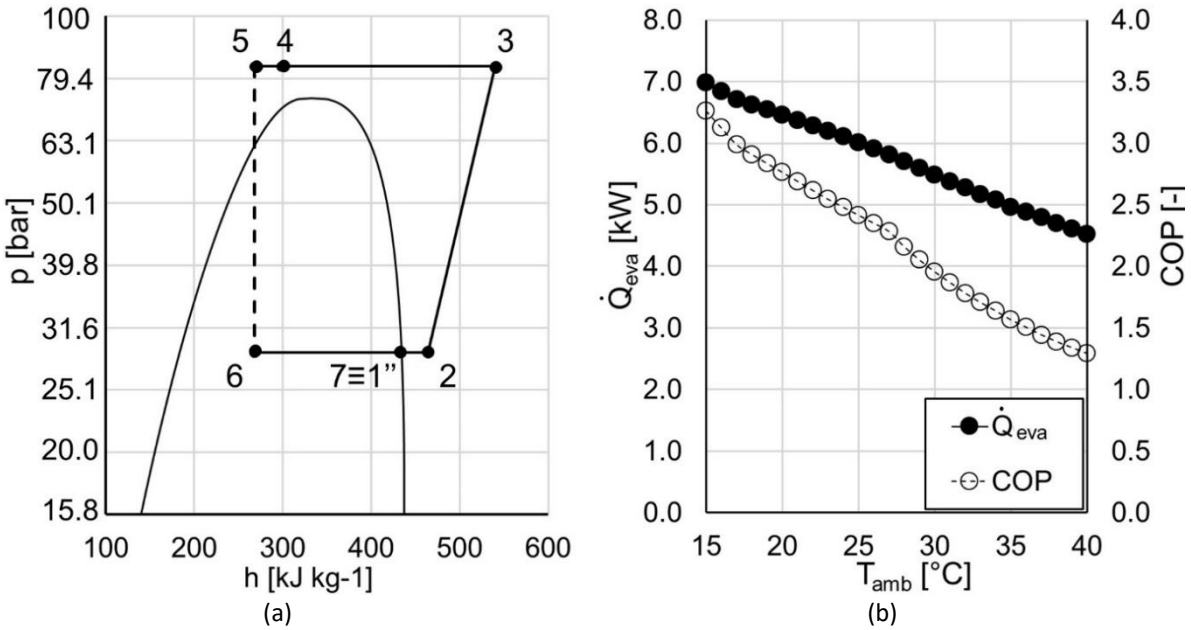

Figure 4.12 – (a) p-h diagram of the reference cycle operating at standard conditions (b) trend of refrigerating capacity and COP at fixed evaporator inlet air temperature and varying ambient temperature

4.6.2. Ejector cycle configuration

In this configuration, since the evaporation pressure is a free parameter which can be set by a manual throttling valve (see section 4.3.2), the optimum evaporation pressure which maximize the COP was

chosen, solving $(\partial \mathrm{COP_{EJ}}) \,/\, (\partial \mathrm{p_{eva}}) = 0$, where $\mathrm{COP_{EJ}}$ refers to the COP of the ejector cycle. Table 4.2 provides the comparison between the results obtained in the simulation of the traditional cycle and the ejector cycle at the same reference conditions of internal space temperature equal to -2 °C and external ambient temperature equal to 30 °C.

Table 4.2 – Comparison between the performance of the system operating according the traditional cycle and ejector cycle: $\mathrm{T_{air,IN}} = -2°\mathrm{C}$, $\mathrm{T_{amb}} = 30\ °C$

Variable	Traditional config.	Ejector config.	Unit
T_{eva}	-6.97	-7.30	°C
p_{eva}	28.8	28.6	bar
$T_{separator}$	-6.9	-5.5	°C
$p_{separator}$	28.8	30.1	bar
$T_{air,OUT}$	-5.4	-5.5	bar
$\dot{Q}_{eva}$	5.49	5.74	kW
P_{el}	2.80	2.82	kW
COP	1.96	2.04	-
$\dot{Q}_{IHX}$	1	-	kW
ε_{IHX}	0.6	-	-
$\dot{m}_{V}$	118.8	152.2	kg h^{-1}
$\dot{m}_{EJ}$	-	115.6	kg h^{-1}
$\dot{m}_{BY-PASS}$	-	36.5	kg h^{-1}
ϕ_{EJ}	-	0.7	-
Δp_{lift}	-	1.49	bar

It can be observed that the ejector cycle presents an increase of 4.5% of refrigerating capacity and 4% increase of COP compared to the traditional cycle configuration. This is due to the fact that in the ejector cycle, a higher operative pressure at the liquid-vapor separator is obtained due to the pressure lift provided by the ejector itself, ensuring a lower electric power draw at the compressor, coupled by an higher cooling capacity.

The comparison between the refrigerating capacity and COP with a fixed internal air temperature and a varying ambient temperature for the two configurations is also provided in Figure 4.13.

Once different ambient temperatures are considered (Figure 4.13) it can be observed that the ejector system increases its advantage over the traditional system up to a maximum of 11.5% and 14.8%, for COP and refrigerating capacity respectively, for T_{amb}=38 °C. The model also allows to calculate the functional limits of the two-phase ejector: the system operating according to the ejector cycle can

reach a steady state equilibrium only for ambient temperature higher than 28 °C: below this limit, the liquid volume fraction at the mixing point M is higher than the expected for every feasible receiver pressure.

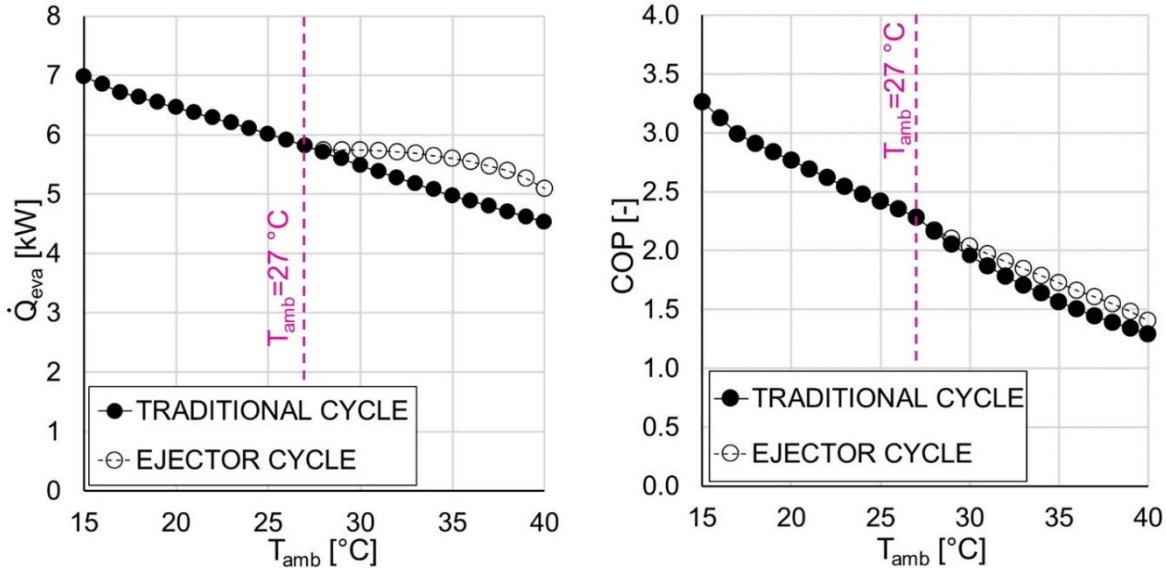

Figure 4.13 – Comparison between the simulation results obtained for the traditional cycle and ejector cycle (a) refrigerating capacity (b) COP

4.6.3. Ejector cycle configuration using the auxiliary evaporator

The thermal performance of the system operating according to the ejector cycle can be improved with the use of an auxiliary evaporator in the line of the refrigerant returning to the liquid-vapor separator after the expansion, which evaporates part of the liquid out of the ejector, before it reaches the liquid separator. The heat absorbed by the refrigerant in the auxiliary evaporator $\dot{Q}_{AUX}$ ensures the vapor quality increase (from x_M to x_1) in the temperature range between the separator working point (-5.5 °C for the case of T_{amb}=30 °C) and the evaporator air inlet temperature (-2 °C) as shown in the shaded area in Figure 4.14a.

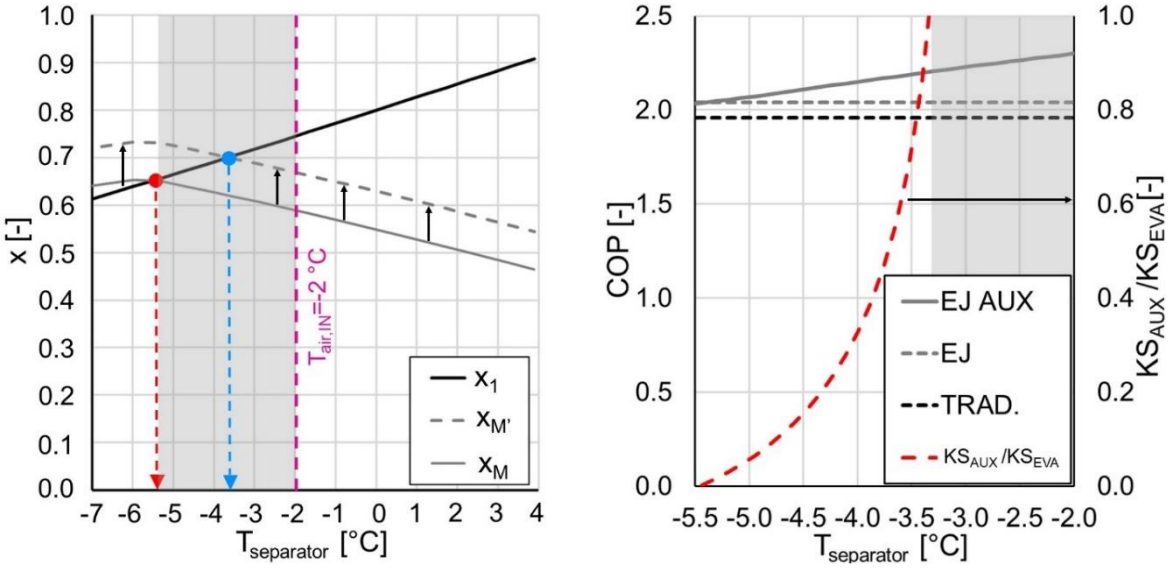

(a) (b)

Figure 4.14 – (a) Separator's operating pressure increase possible area using the auxiliary evaporator (b) Advantage on COP given by the ejector cycle with an auxiliary evaporator

The trend of the COP of the refrigerating system using the ejector configuration and ejector cycle with auxiliary evaporator compared with the COP of the system operating according to a traditional cycle is reported in Figure 4.14b. As it can be observed, COP increases nearly linearly as the receiver temperature (and thus pressure) increases. The practical consequence of this configuration is the reduction of the temperature difference between the refrigerant and the air at the inlet of the evaporator. In the same figure, it is also possible to observe the trend of the ratio between the required overall heat transfer coefficient of the two evaporators KS_{AUX} and KS_{EVA} for the same range of temperatures $T_{separator}$, assuming the same air flow rate of the main evaporator, 4800 m^3h^{-1}, for the auxiliary evaporator. The values of ratio between the product of overall heat transfer coefficient and exchanging area (KS) for the auxiliary evaporator and the main one, which assesses the comparison between the geometric dimensions of the two heat exchangers, value of COP in the case of ejector cycle using the auxiliary evaporator for different liquid-vapour separator operative temperatures and the corresponding percentage advantage over the traditional configuration are reported in Table 4.3.

Table 4.3 - Performance of the ejector cycle using the auxiliary evaporator for a varying dimension of the auxiliary evaporator (KS_{AUX})

$T_{separator}$ [°C]	KS_{AUX}/KS_{EVA}	$COP_{EJ\ AUX}$	$\Delta COP_{\%}$
-5.4	0.002	2.04	3.8 %
-5.0	0.07	2.07	5.4 %
-4.5	0.16	2.11	7.2 %
-4.0	0.33	2.15	8.9 %
-3.5	0.69	1.27	10.4 %

-3.3	1.12	2.21	11.1 %
-3.1	3.64	2.22	11.9 %

It is possible to observe that the numerical model assesses a theoretical increase of 11.1% on COP if the auxiliary evaporator is sized with the same geometry as the main one (KS_{AUX}=1.12 KS_{EVA} in Table 4.3). Assuming this sizing of the auxiliary evaporator, the comparison between the refrigerating capacity and COP, for a fixed internal space temperature of -2 °C and a varying ambient temperature, for all three possible operating configurations of the refrigerating system is provided in Figure 4.15.

It can be observed that the use of the auxiliary evaporator can extend the operation range of the two-phase ejector cycle even for an ambient temperature lower than 28 °C, providing a constant advantage of 10-13% for both COP and refrigerating capacity over the traditional cycle configuration.

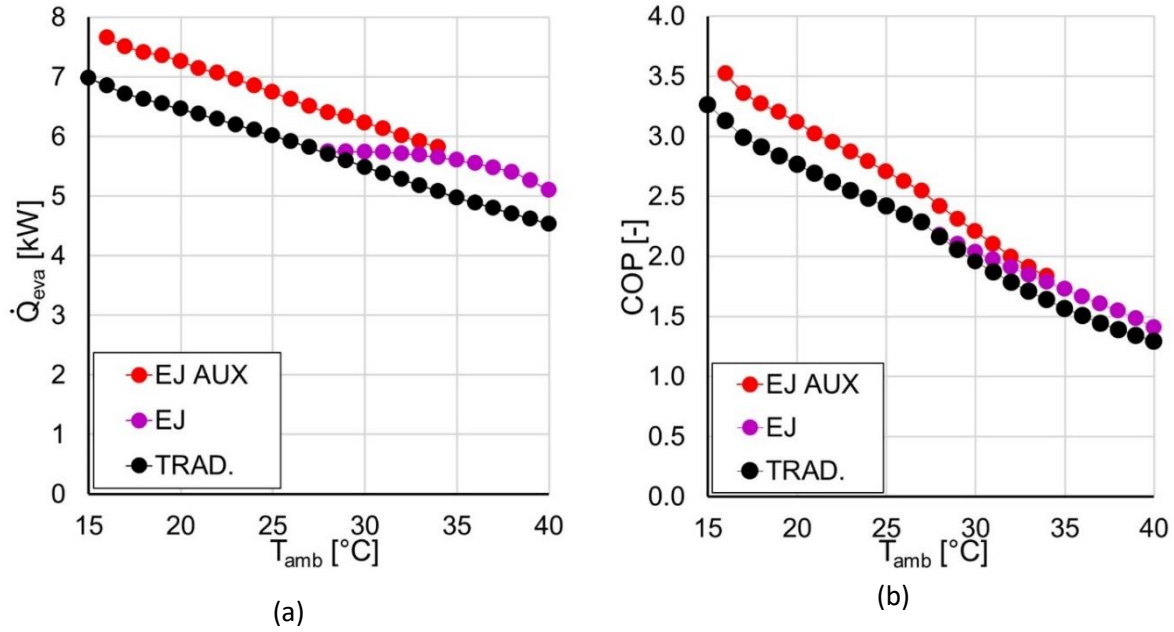

(a) (b)

Figure 4.15 – Numerical results and comparison between the three configuration of the refrigerating system (a) refrigerating capacity (b) COP

4.7. Numerical model of the refrigerating system using the software AMESim

After the development of the steady state numerical model of the refrigerating system, a full dynamic model of the same refrigerating system was developed with the software AMESim v.17. Differently from the previous model, which assesses the theoretical performance of the system operating in steady state conditions, the numerical model presented in this section allows the investigation of the dynamic behaviour of each component of the cooling unit, as the dynamic evolution of every state variable of the system is provided. Moreover, with the software AMESim v.17, a more accurate modelling approach is possible, as the following features are introduced:

- Pressure losses of the refrigerant flowing throughout the pipes of the heat exchangers are considered
- Expansion processes in the back pressure and manual throttling valves of the systems are not considered isenthalpic ideal processes: an actual sub-model of the valve evaluates the localized pressure loss as a function of the actual crossing area of the valve and accounts for the effect of a localized restriction on the flow of the refrigerant
- The gas-cooler/condenser is modelled as an actual heat exchanger and not as an ideal one: to ensure the operation of the high pressure side in optimal conditions, the fans' rotation velocity (and thus developed air mass flow rate) and the back-pressure valve cross area are modulated by a PI controller, which ensure the maintenance of the set point values of temperature and high operative pressure of the refrigerant at the outlet of the heat exchanger
- Air humidity at the inlet of the evaporator and gas-cooler/condenser is considered and thus both sensible and latent heat exchange are evaluated. Moreover, the simulation of the heat exchangers of the system are not obtained with a macroscopic model but with a more detailed 1-D numerical model, where the device is approximated with a counter-flow heat exchanger and is discretized in 6 elements. Each element is modelled with a lumped capacitance which considers the refrigerant flow, the thermal mass of the tubes and fins and the air flow
- The liquid-vapour separator is modelled with an actual internal volume and the height of liquid refrigerant inside of the volume is a function of the refrigerant charge of the system.

The numerical model is developed with the two-phase flow library which is composed of basic elements that are designed to model the transient behaviour of internal and external flow, i.e. refrigerant and air. The numerical model is developed under the following assumptions: the components modelling the refrigerant side are based on a homogeneous fluid model, considering the two-phases to flow as a single phase possessing mean fluid properties. The homogenous fluid model considers no slip between the two-phases (liquid and vapour phases possess the same velocity) and thermodynamic equilibrium between liquid and vapour phases. The internal flow in one-dimensional and external flow is zero-dimensional, since air mass flow rate and its distribution are imposed. Refrigerant pressure losses and heat transfer coefficients are evaluated with empirical correlations extracted from literature and the effect of gravity is neglected by the model.

The two-phase flow library also provides the thermophysical properties of carbon dioxide and air: the thermodynamic properties of CO_2 are evaluated with Modified Benedict Webb Rubin (MBWR) equation [22], considering the pressure as a function of the fluid's density and temperature, while the air is considered as a mixture, composed by a combination of pure fluids weighted by its concentration.

Basic elements are coupled to develop the sub-model of the main components of the system, which are connected to form the complete numerical model of the refrigerating unit. The system includes mass flow devices (compressor, expansion devices, two-phase ejector) and energy flow devices (evaporator, gas-cooler/condenser, internal heat exchanger): as the dynamics of the mass flow devices are generally an order of magnitude faster than those of the heat exchangers, according to Rasmussen et al.[23], the compressor, expansion devices and two-phase ejector are considered static components and are modelled using steady-state empirical equations. On the other hand, the modelling of the heat exchangers, which are characterized by a more complex nature, is conceived with a discretization of the devices into smaller volumes, each treated with a lumped parameters approach. The pressure drops of the refrigerant flowing through the pipes connecting different components is neglected, as the assumption of short pipes is made, being the system conceived as a compact unit.

Table 4.4 reports the system's main components characteristic dimensions, which are chosen among real components available on the market.

Though a dynamic model is developed, in this section, the thermal performance of the refrigerating system once steady state condition is achieved is presented. The full dynamic simulation of the system will be presented in the next chapter (see chapter 5) where will be coupled with the unsteady simulation of the insulated body (presented in chapter 3) to simulate a typical delivery mission.

Table 4.4 – Main components' main dimensions

Component	Dimension
Semi-hermetic compressor	Displacement volume, $\mathrm{V_d} = 27.47\ \mathrm{cm^3}$
(Dorin CD 360 H)	Nominal rotation velocity, $\mathrm{n} = 1450\ \mathrm{rpm}$
Finned-coil gas-cooler/condenser	External convective area, $\mathrm{A_e} = 37.6\ \mathrm{m^2}$
(LU-VE SAV5R 4511)	Internal convective area, $\mathrm{A_i} = 4.9\ \mathrm{m^2}$
	Fans power draw, $\mathrm{P_{fans,g-c}} = 0.12\ \mathrm{kW}$
	Nominal air flowrate, $\dot{\mathrm{V}}_{\mathrm{air}} = 3050\ \mathrm{m^3 h^{-1}}$

Finned-coil evaporator	External convective area, $A_e = 39.4\ m^2$
(LU-VE F35HC 215)	Internal convective area, $A_i = 3.8\ m^2$
	Fans power draw, $P_{fans,g-c} = 0.35\ kW$
	Air flowrate, $\dot{V}_{air} = 4800\ m^3 h^{-1}$
Fixed-geometry two-phase ejector	Throat diameter, $d_{th} = 1\ mm$
Internal heat exchanger	Exchanging area, $A_{IHX} = 0.39\ m^2$
Low-pressure receiver	Internal volume, $V_{LPR} = 30\ l$

4.7.1. Low pressure receiver numerical model

In two-phase flow applications, the low-pressure receiver is a device used to separate liquid from the vapor, storing excess of refrigerant mass to ensure system capacity over a wide range of operating conditions while preventing liquid flow back and consequent damage to the compressor. The sub-model of the liquid-vapor separator is conceived assuming an adiabatic constant cross-sectional area receiver: the pressure is considered homogeneous in the entire volume and the densities of both liquid and vapor phase are considered homogeneous as well in their respective volumes. The governing equations (Eq. 4.17- Eq. 4.18) of the sub-model are obtained with the formulation of mass and energy conservation principles in the low-pressure receiver's control volume:

$$V_{LPR} \frac{d\bar{\rho}_{LPR}}{dt} = \dot{m}_{in} - \dot{m}_L - \dot{m}_V \tag{4.17}$$

$$V_{LPR} \left(\bar{\rho}_{LPR} \frac{d\bar{h}_{LPR}}{dt} - \frac{d\bar{p}_{LPR}}{dt} \right) = \dot{m}_{in} \left(h_{in} - \bar{h}_{LPR} \right) - \dot{m}_L \left(h_L - \bar{h}_{LPR} \right) - \dot{m}_V \left(h_V - \bar{h}_{LPR} \right) \tag{4.18}$$

The average refrigerant pressure $\bar{p}_{LPR}$ and specific enthalpy $\bar{h}_{LPR}$ are used to compute the state of the refrigerant leaving the receiver (in the state of saturated liquid, $\dot{m}_L$, and vapor, $\dot{m}_V$, respectively). The percentage of liquid volume inside of the receiver is then evaluated with Eq. 4.19, which is used to determine the height of the liquid-vapour interface H_{LV}.

$$r_{LPR} = \frac{\bar{\rho}_{LPR} - \rho_V}{\rho_L - \rho_V} \tag{4.19}$$

4.7.2. Semi-hermetic compressor numerical model

The semi-hermetic compressor is modelled as a fixed-displacement compressor. The parameters required as input are the value of volumetric efficiency η_V and overall efficiency η_C, which are

computed from data supplied by the compressor manufacturer, the compressor's displacement V_d and the nominal rotatory speed n. Given the state of the refrigerant at the inlet, the compressor provides the value of developed mass-flowrate $\dot{m}_V$ (Eq. 4.1), electric power draw $P_{el,comp}$ (Eq. 4.2) and the state of the refrigerant at the outlet.

4.7.3. Evaporator numerical model

The finned-coil heat exchanger is approximated to a simple straight tube in tube counter-flow configuration. The counter-flow design is then discretized into 6 longitudinal lumped volumes (Figure 4.16): for each discretized volume it is possible to identify three nodes: a node referring to the refrigerant flow (C_r), a node referring to the state of tube wall and fins (C_w) and a node referring to the state of the air (C_a). The number of discretized elements, N, was decided with a preliminary sensitivity study where N was increased until the solution demonstrated insensitivity to the variation of number of elements. The geometric dimensions of the heat exchanger were equally distributed in each lumped element, which in turn is composed by three basic components: an internal flow component accounting for the refrigerant flowing inside of the pipes, a thermal capacity element accounting for the thermal mass of the heat exchanger structure and an external flow component accounting for the air flowing outside of the pipes.

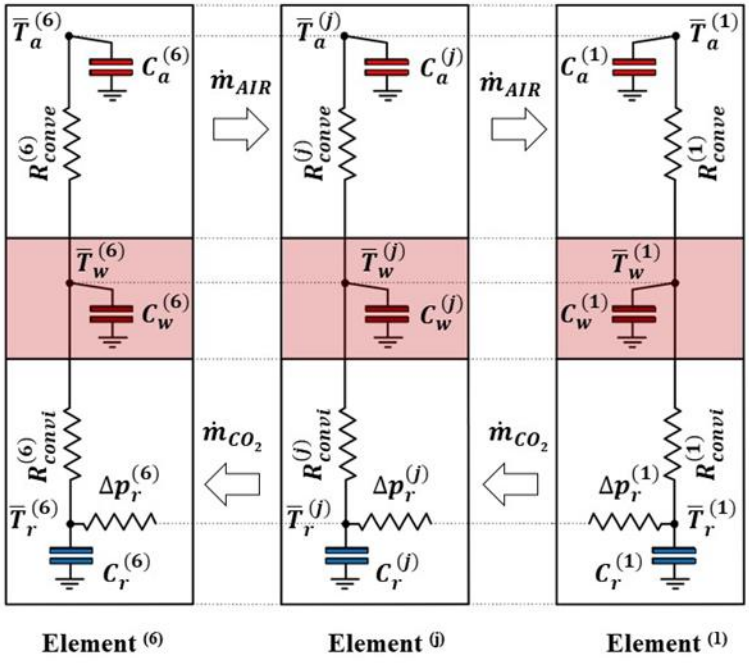

Figure 4.16 - Equivalent counter-flow heat exchanger discretization lumped-parameters system

The internal flow is considered one-dimensional and fluid properties vary only in the direction of the flow. Each internal flow component is composed by a capacitive element (C), which computes the value of pressure and density in the associated volume, and a resistive element (R) which evaluates the dissipations given by the pressure losses. As result, the dynamic trend of the mean thermodynamic properties of the refrigerant flowing inside of the j-th tube element ($\overline{T}_r^{(j)}$, $\overline{p}_r^{(j)}$, $\overline{h}_r^{(j)}$) are obtained. In

the resistive element, the total pressure gradient Δp_r is computed from the algebraic sum of the friction pressure drop and the acceleration pressure drop due to a change in the fluid's density along the flow axis, while the contribution of the gravity to the total pressure gradient is neglected. The internal convective heat flux $\dot{Q}_{convi}^{(j)}$ is obtained with Eq. 4.20:

$$\dot{Q}_{convi}^{(j)} = \alpha_i^{(j)} A_i^{(j)} (\overline{T}_W^{(j)} - \overline{T}_r^{(j)}) \quad (4.20)$$

Where α_i is the internal convective heat transfer coefficient, computed from empirical correlations available on literature which will be explained later in this section. As the energy transferred from the refrigerant to the tube wall and fins is equal to the energy taken away by the air and the energy kept in the wall and fins because of their thermal inertia, the wall and fins are lumped together using a single thermal capacity element. The thermal-capacity component accounts for the thermal structure of the heat exchanger quantifies the mean wall temperature $\overline{T}_W^{(j)}$ through Equation 4.21, obtained by the formulation of energy conservation principle with the assumption of mono-dimensional heat flow, as conduction heat flow through wall elements is neglected:

$$C_W^{(j)} \frac{d\overline{T}_W^{(j)}}{d\tau} = \dot{Q}_{convi}^{(j)} - \dot{Q}_{conve}^{(j)} \quad (4.21)$$

The external flow component assesses the mean thermodynamic properties of the air flowing outside of the j-th tube element ($\overline{T}_a^{(j)}$, $\overline{p}_a^{(j)}$, $\overline{h}_a^{(j)}$), assuming a zero-dimensional flow and negligible conduction in the airflow direction. Since pressure losses in the air flow are neglected, the pressure has the same value in each element ($\overline{p}_a^{(1)} = \overline{p}_a^{(j)} = \overline{p}_a^{(6)}$), while the convective heat flow is computed through Eq. 4.22:

$$\dot{Q}_{conve}^{(j)} = \alpha_e^{(j)} A_e^{(j)} (\overline{T}_a^{(j)} - \overline{T}_W^{(j)}) \quad (4.22)$$

All the empirical correlations computed to evaluate the heat transfer rate and the pressure drop of the refrigerant are available in Table 4.5.

Table 4.5 – Empirical correlations utilized in the case of evaporator submodel

	Heat transfer coefficient	Pressure drop
Air	Colburn j-factor [24]	
CO_2 subcritical, two-phase evaporation	VDI for horizontal tube, 1992 [25]	Friedel, 1979 [27]
CO_2 subcritical, single phase	Gnielinski, 1976 [26]	Churchill, 1979 [28]

The input required by the sub-model are the geometric dimensions of the heat exchanger and the state of the two fluids, i.e. refrigerant and air, at the inlet. The model provides as output the state of refrigerant and air at the outlet and the cooling capacity of the coil $\dot{Q}_{eva}$, according to Eq. 4.23 (where

$h_r^{(IN)} = \bar{h}_r^{(6)}$ and $h_r^{(OUT)} = \bar{h}_r^{(1)}$), and the total pressure loss $\Delta p_r^{(TOT)}$ of the refrigerant though Eq. 4.24:

$$\dot{Q}_{eva} = \dot{m}_r(h_r^{(OUT)} - h_r^{(IN)}) \quad (4.23)$$

$$\Delta p_r^{(TOT)} = \sum_{j=1}^{6} \Delta p_r^{(j)} \quad (4.24)$$

The mean evaporation pressure $\bar{p}_{EVA}$ and the mean evaporation temperature $\overline{T}_{EVA}$ are also defined as the arithmetic mean of the values of pressure and temperature evaluated in each discretized element of the heat exchanger.

4.7.4. Gas-cooler/condenser numerical model

The same approach described in the previous section was used to model the gas-cooler/condenser. Depending on the external air ambient temperature T_{amb}, which is equal to the air temperature at the inlet of the heat exchanger, the heat rejection can be in both subcritical or transcritical conditions: Table 4.6 reports the numerical correlations employed to evaluate the heat transfer rate and the pressure drop of the refrigerant, as the air pressure drop is neglected.

Table 4.6 – Empirical correlation utilized in the case of gas-cooler/condenser

	Heat transfer coefficient	Pressure drop
Air	Colburn j-factor [24]	
CO_2 transcritical	Gnielinski, 1976 [26]	Friedel, 1979 [27]
CO_2 subcritical, two-phase condensation	Shash, 19769 [29]	Friedel, 1979 [27]

The gas-cooler/condenser refrigerant target outlet temperature$T_{out,gc}^{design}$ and high operative pressure p_{gc}^{design} are defined as a function of the external ambient temperature T_{amb} with the same logic presented in the previous model (see section 4.5). A PI controller was used in order to maintain the actual values of $T_{g-c,out}$ and p_{g-c} close to the design values, acting on the the gas-cooler's fans and the the back pressure valve opening cross-sectional area.

4.7.5. Internal heat exchanger numerical model

The internal heat exchanger located in the suction line of the compressor is modelled with two pipes exchanging heat with one another through a copper medium, as their walls are kept in contact, in a counter-flow configuration. The input required by the sub-model are the exchanging area A_{IHX}, the thermal conductivity of the walls (i.e. copper medium 300 $Wm^{-2}K^{-1}$) and the state of the refrigerant at the two inlets while the state of the refrigerant at the outlets, the heat flow rate $\dot{Q}_{IHX}$ and the effectiveness of the heat exchanger ε_{IHX} are given as output.

4.7.6. Expansion device numerical model

The expansion devices of the system are the back-pressure and the manual throttling valves. The valve is considered adiabatic with the surrounding environment and the effect of chocked flow is neglected. The mass flow rate through the throttle is determined by the flow coefficient C_q, the actual cross flow area A_{op}, the inlet density and the pressure difference across the valve Δp_{VALVE} according to Eq. 4.25:

$$\dot{m} = C_q A_{op} \sqrt{\rho_{in} \Delta p_{VALVE}} \tag{4.25}$$

The input required by the sub-model are the state of the refrigerant at the inlet of the expansion device, the hydraulic diameter of the valve at the maximum opening and the ratio between the actual cross flow area A_{op} and the cross flow area at the maximum opening : $r_{op} = A_{op}/A_{op,MAX}$. In the back-pressure valve numerical model, the value of r_{op} is modulated by a PI controller as previously stated; in the manual throttling valve, the value of r_{op} is set by the user. The output of the sub-model are the state of the refrigerant at the outlet of the expansion device and the value of the localized pressure loss introduced by the valve.

4.7.7. Two-phase ejector numerical model

Like the previous model, the two-phase ejector performance is modelled in accordance with the study of Banasiak *el al.* (2015)[12], which provides the performance mapping for a fixed-geometry vapor ejector and corresponding interpolation functions.

Motive nozzle mass flow rate $\dot{m}_{EJ}$ and ejector entrainment ratio ϕ are expressed as a function of motive nozzle inlet pressure and density, suction nozzle inlet pression and ejector outlet pressure. Given the state of the refrigerant at the motive nozzle and suction nozzle inlet, the model provides as output the value of motive nozzle mass flowrate $\dot{m}_{EJ}$ and entrainment ratio ϕ by means of the interpolation functions. Moreover, with the formulation of the mass and energy conservation equation, the specific enthalpy and the total mass flow rate at the outlet of the ejector are evaluated with Eq. 4.26 and Eq. 4.27:

$$\dot{m}_{OUT,EJ} = \dot{m}_{EJ} + \dot{m}_{L} \tag{4.26}$$

$$h_{OUT,EJ} = \frac{h_{EJ} + \phi h_L}{1+\phi} \tag{4.27}$$

The model also provides the value of the ejector efficiency η_{EJ}, according to the definition given by Elbel and Hrnjak (2008) [30] reported in Eq. 3.28:

$$\eta_{EJ} = \phi \frac{h_C - h_D}{h_A - h_B} \tag{4.28}$$

Where h_A is the specific enthalpy of the refrigerant at the ejector's motive nozzle (h_8) and h_B is equal to the specific enthalpy of the refrigerant at the ejector's suction nozzle. On the other hand, the specific enthalpies h_C and h_D are evaluated at the same ejector outlet pressure (p_D) but at the suction nozzle and motive nozzle specific entropies s_8 and s_4 respectively.

4.8. Numerical results of the model developed with the software AMESim

The internal flow components in the low-pressure side of the system are initialized to the saturation pressure corresponding to the internal cargo space temperature ($T_{air,IN}$) and unitary vapour quality and the internal flow components in the high-pressure side of the system are initialized to the optimum high pressure and external ambient temperature. The external flow components and thermal masses of the heat exchanger are initialized to the environmental temperature they are located in: $T_{air,IN}$, T_{amb} respectively. After the initialization of the state variable of the system, a simulation time of 3600 s was imposed, to ensure the achievement of steady state condition and the independence of the solution from the initial conditions. A variable step integration method was employed to calculate the numerical solution; to check the accuracy of the numerical results, a tolerance of 10^{-7} was utilized. When the iteration converges, an error test is applied to determine if the results are accurate enough, however if the error test fails, the integration step must be replaced with a smaller step size.

Similarly to the previous numerical model, the model is utilized to investigate the theoretical performance of the refrigerating system operating in different configurations. The performance of the system operating according to a traditional back-pressure cycle (BP) is taken as reference, while the performance of the ejector cycle (EJ) and ejector cycle with an auxiliary evaporator (EJ-AUX) will be compared to the reference configuration.

4.8.1. Performance comparison among the classical configuration and the ejector cycle configuration

The performance indicator of the systems efficiency is given by the Coefficient Of Performance (COP), as reported in Eq. 4.29.

$$COP = \frac{\dot{Q}_{eva}}{P_{el,comp}} \tag{4.29}$$

To determine the COP of the system operating in different steady-state working points, the evaporator' s air return temperature $T_{air,IN}$ (assumed to be equal to the internal cargo space mean temperature T_i) is set equal to -2 °C while the external ambient temperature, instead, is varied in a range between 15 °C and 45 °C to consider the operation of the system in both subcritical and transcritical conditions.

While in the BP configuration the evaporation pressure results from the system equilibrium with the internal and ambient temperature, in the EJ configuration, the evaporation pressure is a free parameter that can be manually set by mean of the manual throttling valve. For each pair of temperatures ($T_{air,IN}$,T_{amb}) which identify a steady state working point, the opening degree of the manual throttling valve (h) was set to maximize the COP, solving $\partial COP_{EJ} / \partial \bar{p}_{eva} = 0$, as already discussed in section 4.6.2.

Figure 4.17 reports the comparison between the performance of the refrigerating system operating according to a traditional back-pressure configuration (BP) and simple ejector configuration (EJ). From Figure 4.17a is possible to observe the comparison between the trend of COP_{BP} and COP_{EJ}, which

demonstrates that if the system is operating in a hot environment (T_{amb}> 26 °C) the ejector cycle configuration results to be most convenient.

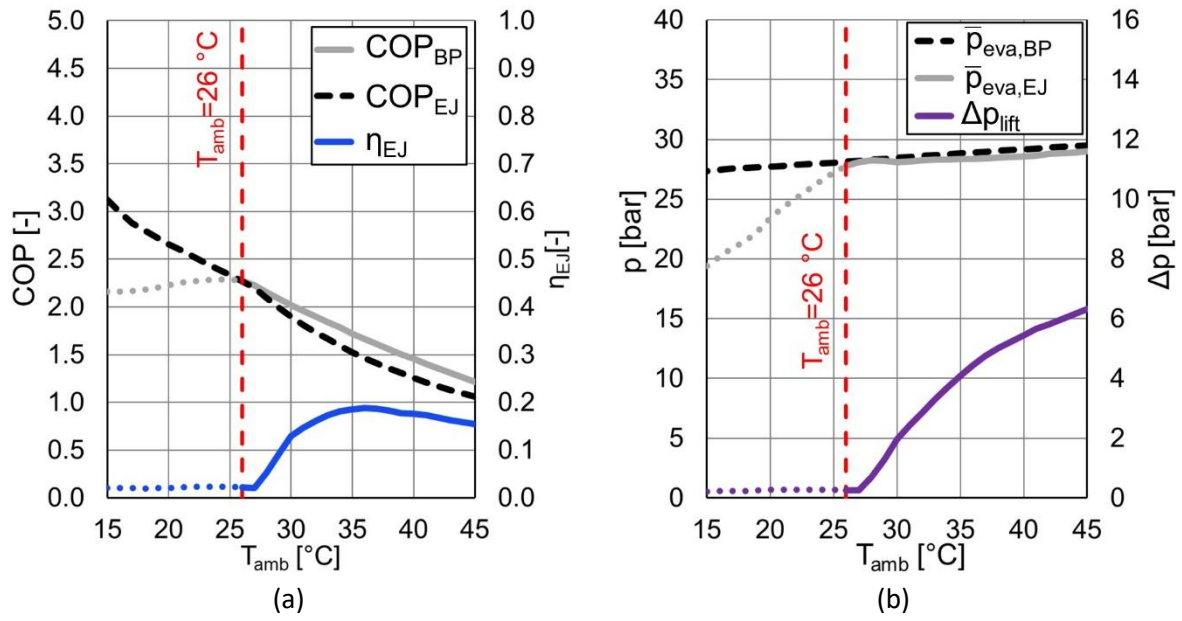

Figure 4.17 – Trend of (a)COP_{BP}, COP_{EJ} and η_{EJ} (b) $\bar{p}_{eva,PB}$, $\bar{p}_{eva,EJ}$ and Δp_{lift} for an internal cargo space temperature of -2°C and a varying ambient temperature

This is given by the fact that, even if the mean evaporation pressure of the EJ configuration is slightly inferior than the one of the BP configuration (Figure 4.17b), the pressure lift provided by the two-phase ejector ensures a higher value of operating pressure at the low-pressure receiver, leading to a major energy saving at the semi-hermetic compressor, which is quantified by the ejector efficiency reported in Figure 4.17a. On the other hand, when the ambient temperature is below the value of 26 °C, the traditional BP configuration results to be the most convenient, as there is no more benefit given by the two-phase ejector, since the pressure lift is constantly below the value of 0.3 bar. The steady state working point is in fact determined by the equilibrium between the vapour quality of the two-phase mixture at the mixing point M(x_M) resulting from the ejector working condition and the vapour quality of the refrigerant entering the liquid-vapour separator needed to feed the liquid line (1L) and the vapour line (1V) at the same operating condition, as already in the mass and energy balance of the previous numerical model (see section 4.5.2). For a decreasing ambient temperature T_{amb}, the specific enthalpy at the gas-cooler/condenser's outlet is reduced, and so is the vapour quality at the mixing point x_M. On the other side, as the gas-cooler/condenser's operative pressure lowers, the ejector's performance is reduced, leading to a lower entrainment ratio ϕ at constant pressure lift, which causes an increase of the value of vapour quality x_1 required to reach the equilibrium to the low pressure receiver. The contemporary reduction of the vapour quality x_M and the need for a higher x_1 leads to a consequent decrease of $\bar{p}_{LPR}$ to promote a higher entrainment ratio, reducing the pressure lift of the ejector until the constrain $x_1 = x_M$ is satisfied. Figure 4.18 reports the trend of the entrainment ratio ϕ and ejector efficiency η_{EJ} as a function of the pressure lift Δp_{lift} provided by the ejector.

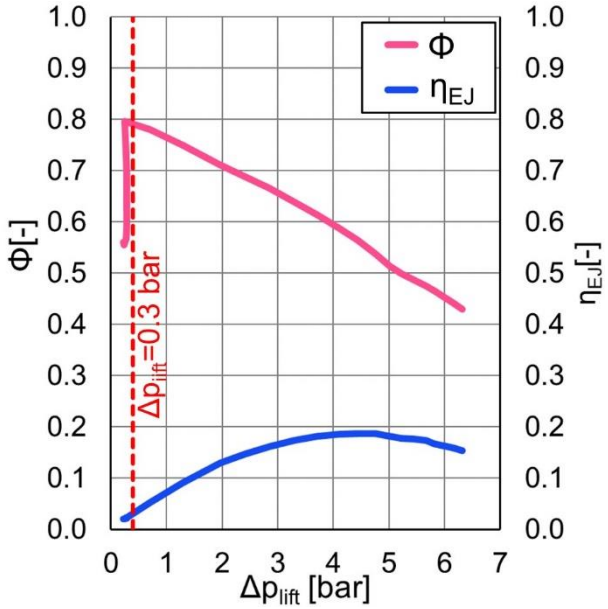

Figure 4.18 – Ejector efficiency and entrainment ratio as function of the ejector's pressure lift

Table 4.7 instead, reports the values of $\mathrm{COP_{BP}}$, $\mathrm{COP_{EJ}}$ and the percentage difference between these two values $\Delta\mathrm{COP_{\%}}$ (defined in Eq. 4.29) as a function of the external ambient temperature.

$$\Delta\mathrm{COP_{\%}} = \frac{\mathrm{COP_{EJ}} - \mathrm{COP_{BP}}}{\mathrm{COP_{EJ}}} \cdot 100 \tag{4.30}$$

The performance indicators of the two-phase ejector operating in the refrigerating system are reported in Table 4.8 for the corresponding values of ambient temperature.

Table 4.7 – Performance comparison between the traditional cycle configuration and ejector cycle configuration at $\mathrm{T_{air,IN}} = -2$ °C, with a varying $\mathrm{T_{amb}}$

$\mathbf{T_{amb}}[°\mathbf{C}]$	$\mathbf{COP_{BP}}[-]$	$\mathbf{COP_{EJ}}[-]$	$\Delta\mathbf{COP_{\%}}$
15	3.13	2.16	-33.9 %
17	2.88	2.17	-32.5 %
20	2.66	2.23	-19.3 %
22	2.53	2.27	-11.6 %
25	2.33	2.29	-1.9 %
27	2.20	2.23	+1.1 %
30	1.90	2.02	+6.0 %
32	1.73	1.90	+8.8 %
35	1.53	1.72	+11.2 %

38	1.35	1.56	+13.0 %
40	1.26	1.45	+13.7 %
42	1.17	1.36	+13.8 %
45	1.06	1.22	+13.0 %

Table 4.8 –Characteristic parameters of the ejector operating in the ejector cycle configuration at $T_{air,IN} = -2$ °C, with a varying T_{amb}

$\mathbf{T_{amb}}[°\mathbf{C}]$	$\boldsymbol{\phi}[-]$	$\boldsymbol{\eta_{EJ}}[\%]$	$\Delta\mathbf{p}_{lift}[\mathrm{bar}]$	$\dot{\mathbf{m}}_{\mathbf{EJ}}[\mathrm{kg\ h^{-1}}]$
15	0.56	2.1	0.22	90.8
17	0.56	2.0	0.24	99.7
20	0.57	2.0	0.27	113.8
22	0.62	2.3	0.28	112.9
25	0.73	2.3	0.27	106.1
27	0.80	2.0	0.25	100.7
30	0.71	12.9	1.97	115.6
32	0.67	16.1	2.85	126.4
35	0.59	18.6	4.09	143.3
38	0.51	18.2	5.02	160.9
40	0.49	17.6	5.45	165.0
42	0.47	16.8	5.82	167.0
45	0.43	15.4	6.32	169.9

As refrigerated transport is characterized by a high variability of operating conditions not only on the external environment temperature (T_{amb}), but also on the internal cargo space temperature (T_i), the performance of the ejector cycle was also evaluated for an internal cargo space temperature varying in between -5 °C and 15 °C. Table 4.9 reports the percentage variation between COP_{EJ} and COP_{BP}, as defined in the Eq. 4.30, assessing that the best performance of the ejector cycle configuration can be found for an high ambient and an internal space temperature comprehended between +5 °C and -5 °C, compatible with the typical internal air temperature required during transportation of chilled products. The maximum convenience of 15.9 % on COP over the traditional configuration is identified for an ambient temperature of 42 °C and internal cargo space temperature of -5 °C.

The pressure lift provided by the ejector and the ejector efficiency for the same temperature range can be observed in Table 4.10 and 4.11 respectively.

Table 4.9 –$\Delta COP_{\%}$ between the EJ and BP configurations for a varying T_i and T_{amb}

T_{amb}/T_i [°C]	-5	0	5	10	15
15	-33.5	-53.5	-76.2	-102.8	-134.9
17	-22.2	-39.6	-59.6	-82.7	-110.5
20	-10.3	-25.8	-42.6	-62.7	-85.4
22	-2.8	-17.4	-32.9	-51.0	-71.7
25	1.9	-6.8	-20.9	-36.5	-55.0
27	3.0	3.5	-8.4	-22.5	-37.5
30	8.3	4.8	2.2	-1.8	-12.4
32	10.6	7.6	4.8	2.1	-0.1
35	13.7	10.0	7.7	5.2	3.2
38	15.5	11.7	8.7	7.0	4.6
40	15.3	11.9	9.1	7.1	5.1
42	15.9	12.4	8.7	6.8	4.9
45	12.8	12.2	7.9	5.0	3.5

Table 4.10 –pressure lift Δp_{lift} provided by the ejector evaluated with a varying T_i and T_{amb}

T_{amb}/T_i [°C]	-5	0	5	10	15
15	0.22	0.22	0.23	0.23	0.24
17	0.23	0.24	0.25	0.25	0.26
20	0.25	0.28	0.29	0.30	0.31
22	0.25	0.29	0.31	0.33	0.34
25	0.26	0.30	0.33	0.35	0.37
27	1.76	0.28	0.34	0.36	0.38
30	2.42	1.48	0.61	0.45	0.52
32	3.33	2.54	1.70	0.87	0.58
35	4.81	3.83	3.14	2.39	1.62
38	5.54	4.75	4.10	3.57	2.90
40	5.66	5.18	4.58	4.16	3.59
42	6.68	5.55	4.83	4.30	3.87
45	7.56	5.91	4.92	4.27	3.85

Table 4.11 – ejector efficiency η_{EJ} evaluated with a varying T_i and T_{amb}

T_{amb}/T_i [°C]	-5	0	5	10	15
15	2.0	2.1	2.2	2.3	2.4
17	1.9	2.1	2.2	2.2	2.3
20	2.0	2.2	2.4	2.6	2.8
22	2.0	2.4	2.7	2.9	3.1
25	2.0	2.5	3.0	3.3	3.6
27	12.8	2.5	3.1	3.4	3.8
30	14.6	10.2	4.9	4.2	5.3
32	17.5	15.2	11.7	7.0	5.6
35	20.8	18.4	17.3	15.2	12.0
38	19.7	18.1	17.8	18.0	17.0
40	17.7	16.9	17.0	17.9	18.0
42	19.5	16.3	15.3	15.6	16.3
45	18.6	14.5	12.4	11.9	12.4

From Tables 4.9-4.11 is possible to observe that for each value of internal cargo space temperature T_i, the model assesses a threshold value of the external ambient temperature over which the ejector cycle configuration is more convenient than the traditional one. The minimum and maximum ambient temperature threshold values are equal to 25 °C and 35 °C for an internal space temperature of -5 °C and 20 °C respectively.

4.8.2. Performance comparison among the classical configuration and the ejector cycle configuration using an auxiliary evaporator in the line between the ejector outlet and the low-pressure receiver

When the auxiliary evaporator is considered, the constrain described in the previous section on the vapour quality can be by-passed, as the vapour quality x_M can be increased to the required equilibrium value x_1 thanks to the heat exchange performed by the evaporator. Furthermore, with the use of an auxiliary evaporator, the operating range of the two-phase ejector can be extended to lower ambient temperatures, as will be discussed later in this section. The COP for the refrigerating system operating according to this configuration, is defined in Eq. 4.31:

$$COP_{EJ-AUX} = \frac{\dot{Q}_{eva} + \dot{Q}_{eva,AUX}}{P_{el,comp}} \tag{4.31}$$

The auxiliary evaporator was assumed for this study to have the same geometrical dimensions of the main one (see Table 4.4). As done in the EJ configuration, due to the possibility of choosing the pressure loss at the manual throttling valve, the optimal mean evaporation pressure which maximizes the COP was chosen for each steady state working point.

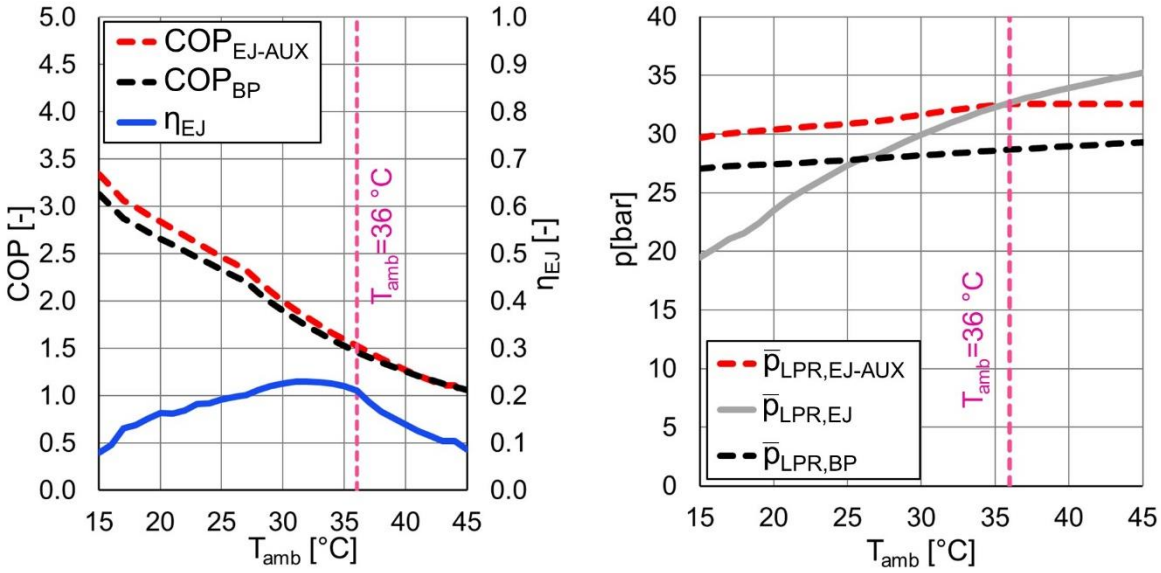

Figure 4.19 –Trend of (a) COP for the EJ-AUX and BP configurations (b) low-pressure receiver operating pressure for the three different configurations (BP, EJ, EJ-AUX), with an internal cargo space temperature of -2 °C and a varying ambient temperature

Figure 4.19a provides the comparison between the trend of COP_{BP} and $COP_{EJ\text{-}AIX}$ for an internal space temperature of -2 °C and a varying ambient temperature. Figure 4.19b, instead, reports the trend of the low-pressure receiver operating pressure for the three different configurations (BP, EJ, EJ-AUX) and the same values of internal and external temperatures. From the two figures it is possible to observe that for an external ambient temperature lower than 36 °C, the EJ-AUX configuration ensures the highest value of low-pressure receiver operating pressure. On the other hand, when the external ambient temperature exceeds that value, the low-pressure receiver operating pressure of the ejector cycle with a single evaporator becomes the highest, as the ejector cycle with the auxiliary evaporator cannot increase further the operating pressure of the vessel. This is given by the fact that for T_{amb}< 36 °C, the auxiliary evaporator provides the necessary vapour quality increase (Figure 4.20a) to satisfy the vapour quality constrain required by the liquid-vapour separator. On the other hand, when the ambient temperature exceeds the value of 36 °C, the mean evaporation temperature at the auxiliary evaporator ($\overline{T}_{eva,AUX}$) reaches the maximum admissible value, i.e. the inlet air temperature of -2 °C. Consequently, in the range of external ambient temperatures higher than 36 °C the operating pressure of the low-pressure receiver is constantly at the value of 32.6 bar, as it cannot be increased further, as the auxiliary evaporator can no longer provide the necessary vapour quality increase.

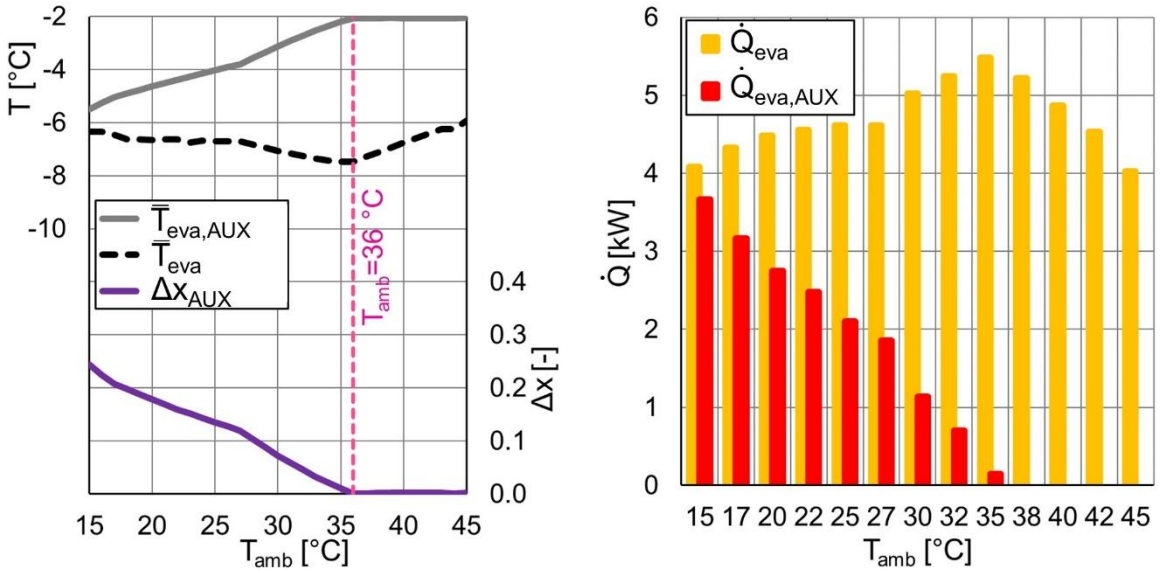

Figure 4.20 – Trend of (a) mean evaporation temperature $\overline{T}_{eva}$, $\overline{T}_{eva,AUX}$ and vapour quality increase in the auxiliary evaporator(b) Cooling power provided by the main and auxiliary evaporator, with an constant internal cargo space of -2 °C and a varying ambient temperature

Figure 4.20b reports the value of cooling power provided by each evaporator as a function of the external ambient temperature with a constant internal air temperature equal to -2 °C. Table 4.12 reports the value of the total cooling capacity of the refrigerating system and the percentage of total cooling power provided by each evaporator, according to the definition given in Eq. 4.32 and Eq. 4.33.

$$\dot{Q}_{eva\,\%} = \frac{\dot{Q}_{eva}}{\dot{Q}_{eva}+\dot{Q}_{eva,AUX}} \cdot 100 \tag{4.32}$$

$$\dot{Q}_{eva,AUX\,\%} = \frac{\dot{Q}_{eva,AUX}}{\dot{Q}_{eva}+\dot{Q}_{eva,AUX}} \cdot 100 \tag{4.33}$$

Table 4.12 – Performance comparison between the traditional cycle configuration and ejector cycle configuration using the auxiliary evaporator (having the same dimensions as the main one) at $T_{air,IN} = -2$ °C, with a varying T_{amb}

$\mathbf{T_{amb}}$[°C]	$\dot{Q}_{\mathbf{eva,TOT}}$[kW]	$\dot{Q}_{\mathbf{eva}}$ %	$\dot{Q}_{\mathbf{eva,AUX}}$ %
15	7.7	52.7 %	47.3 %
17	7.5	57.8 %	42.2 %
20	7.2	62.0 %	38.0 %
22	7.0	64.8 %	35.2 %
25	6.7	68.7 %	31.3 %
28	6.5	71.3 %	28.7 %

30	6.2	81.5 %	18.5 %
32	5.9	88.2 %	11.8 %
35	5.6	97.3 %	2.7 %
38	5.2	100 %	0 %
40	4.9	100 %	0 %
42	4.5	100 %	0 %
45	4.0	100 %	0 %

It can be observed that the heat rate exchanged by the auxiliary evaporator increases as the ambient temperature decreases, reaching a maximum of 47.3 % for an ambient temperature of 15 °C, while for an ambient temperature grater than 36 °C the cooling power it totally provided by the evaporator located in the ejector's suction line.

The comparison between $\mathrm{COP_{BP}}$ and $\mathrm{COP_{EJ-AUX}}$ and the percentage variation $\Delta\mathrm{COP_{\%}}$ evaluated with the same definition given in Eq. 4.30 is given in Table 4.13, from which is possible to observe that the ejector cycle configuration using an auxiliary evaporator is always convenient for an ambient temperature lower than 42 °C.

Table 4.13 – Performance comparison between BP and EJ-AUX configurations. $\mathrm{T_{air,IN}} = -2$ °C and a varying $\mathrm{T_{amb}}$

$\mathbf{T_{amb}[°C]}$	$\mathbf{COP_{BP}}[-]$	$\mathbf{COP_{EJ-AUX}}[-]$	$\Delta\mathbf{COP_{\%}}$
15	3.13	3.34	+6.3 %
17	2.88	3.07	+6.2 %
20	2.66	2.84	+6.4 %
22	2.53	2.69	+6.0 %
25	2.33	2.47	+5.4 %
28	2.20	2.21	+5.3 %
30	1.90	2.00	+5.1 %
32	1.73	1.82	+4.9 %
35	1.53	1.59	+4.2 %
38	1.35	1.39	+2.9 %
40	1.26	1.27	+1.3 %
42	1.17	1.16	-0.6 %
45	1.06	1.00	-5.6 %

Moreover, is also possible to observe that the use of an auxiliary evaporator in the outlet line of the ejector can effectively extend the operating range of the two-phase ejector to lower values of the ambient temperature: in Table 4.15 can be observed, that differently from the previous configuration with a single evaporator, the ejector can provide a significant pressure lift even for an ambient temperature lower than 26 °C, ensuring thus a higher value of operating pressure of the low-pressure receiver even in that range of ambient temperatures.

Table 4.14 –Characteristic parameters of the ejector at $T_{air,IN} = -2$ °C, with a varying T_{amb}

$\mathbf{T_{amb}}[°\mathbf{C}]$	$\boldsymbol{\phi}[-]$	$\boldsymbol{\eta_{EJ}}[\%]$	$\Delta\mathbf{p}_{lift}[\mathrm{bar}]$	$\dot{\mathbf{m}}_{\mathbf{EJ}}[\mathrm{kg\ h^{-1}}]$
15	0.47	7.9	1.00	127.1
17	0.51	13.1	1.65	122.2
20	0.56	16.3	2.09	116.9
22	0.60	16.8	2.22	112.9
25	0.66	19.2	2.59	106.1
27	0.68	20.2	2.78	100.7
30	0.65	22.6	3.68	115.6
32	0.62	23.0	4.21	126.4
35	0.58	22.0	4.85	143.3
38	0.57	16.7	4.71	157.4
40	0.61	13.9	4.43	155.6
42	0.64	11.5	4.15	154.0
45	0.69	8.6	3.74	151.6

As already done with the previous EJ configuration, the performance of the refrigerating system operating according to the EJ-AUX configuration was evaluated also for an internal space temperature varying in a range between -5 °C and 15 °C. Table 4.15 reports the percentage variation of COP_{EJ-AUX} respect to COP_{BP} : while the EJ-AUX configuration presents always an advantage over the BP configuration for an ambient temperature lower than 40 °C, is possible to observe that the EJ-AUX configuration presents the best performance for a low ambient temperature (T_{amb}< 27 °C) and an increasing internal space temperature. While this range of temperatures is not compatible with the typical transport temperature of perishable freights, is compatible with the internal space temperature during the pull-down operation which typically take place prior to the loading of perishable cargo and after door opening operations. The maximum advantage of 14.2% on COP over the traditional cycle can be assessed for an internal temperature of 5 °C and an external ambient temperature of 25 °C.

Table 4.15 – $\Delta COP_{\%}$ between the EJ-AUX and BP configurations for a varying T_i and T_{amb}

T_{amb}/T_i [°C]	**-5**	0	5	10	15
15	6.0	6.2	7.1	7.4	9.0
17	5.9	6.6	7.2	8.3	11.3
20	6.2	6.4	7.1	8.1	11.5
22	6.2	6.1	7.0	8.0	10.6
25	5.5	5.8	14.2	7.4	8.7
27	9.8	10.0	10.8	11.6	13.0
30	4.8	5.1	5.8	6.5	7.4
32	4.5	5.3	5.4	6.1	6.7
35	3.6	4.5	5.2	5.3	6.1
38	1.5	3.7	3.7	4.7	4.8
40	-1.3	2.3	3.1	3.7	3.6
42	-3.8	0.8	1.8	2.5	2.7
45	-10.1	-2.3	-0.1	0.0	0.3

Table 4.16 –Vapour quality increase Δx provided by the auxiliary evaporator for a varying T_i and T_{amb}

T_{amb}/T_i [°C]	-5	0	5	10	15
15	0.22	0.26	0.29	0.34	0.39
17	0.19	0.22	0.25	0.28	0.34
20	0.16	0.19	0.22	0.25	0.30
22	0.14	0.17	0.21	0.24	0.27
25	0.11	0.15	0.21	0.21	0.24
27	0.10	0.13	0.17	0.20	0.23
30	0.05	0.09	0.12	0.15	0.18
32	0.02	0.06	0.10	0.13	0.16
35	0.00	0.03	0.06	0.09	0.12
38	0.00	0.00	0.04	0.07	0.10
40	0.00	0.00	0.02	0.06	0.08
42	0.00	0.00	0.02	0.05	0.07
45	0.00	0.00	0.00	0.04	0.07

Table 4.17 –Pressure lift provided by the ejector for a varying T_i and T_{amb}

T_{amb}/T_i [°C]	-5	0	5	10	15
15	1.25	0.76	0.82	0.87	0.97
17	1.63	1.38	1.09	1.00	1.09
20	1.98	1.84	1.50	1.26	1.34
22	2.61	2.11	2.01	1.56	1.40
25	2.87	2.58	2.01	2.01	1.80
27	3.04	2.79	2.57	2.25	2.29
30	3.94	3.63	3.51	3.49	3.44
32	4.35	4.27	4.31	4.20	4.26
35	4.31	5.05	5.11	5.09	5.19
38	3.93	5.29	5.51	5.73	5.86
40	3.64	4.99	5.74	5.88	6.13
42	3.41	4.67	5.71	6.08	6.25
45	3.00	4.25	5.62	5.78	5.98

Table 4.18 –Ejector efficiency for a varying T_i and T_{amb}

T_{amb}/T_i [°C]	-5	0	5	10	15
15	9.1	6.4	8.5	11.0	15.3
17	11.7	11.5	10.9	12.7	17.1
20	13.9	15.0	14.5	14.9	20.5
22	18.9	16.9	19.1	17.9	20.8
25	20.2	20.1	19.1	21.7	24.6
27	21.1	21.4	22.6	23.4	30.2
30	23.3	23.2	25.3	29.4	35.1
32	22.8	24.2	27.5	30.7	37.2
35	17.6	24.0	26.8	30.1	35.8
38	13.2	20.2	23.2	27.2	31.9
40	10.7	16.1	20.9	23.8	28.4
42	8.9	13.3	17.7	21.1	24.4
45	6.4	10.2	14.1	15.3	17.7

Table 4.17 and 4.18 report the performance of the two-phase ejector operating in the refrigerating system while Table 4.16 reports the vapour quality increase provided by the auxiliary evaporator. From the tables is possible to observe that for an ambient temperature grater than 35 °C and internal space temperature below 5 °C, the auxiliary evaporator do not provide an increase of vapour quality of the two-phase mixture at the ejector outlet, as the evaporation temperature in the auxiliary evaporator reaches the maximum admissible value, as previously discussed. Consequently, the performance of the EJ-AUX configuration decreases, even if the ejector's performance is still considerable.

Lastly, the percentage variation between the coefficient of performance between the EJ-AUX and EJ configuration is provided in Table 4.19, according to Eq. 4.34:

$$\Delta COP_{\%} = \frac{COP_{EJ-AUX} - COP_{EJ}}{COP_{EJ}} \cdot 100 \tag{4.34}$$

Table 4.19 – $\Delta COP_{\%}$ between the EJ-AUX and EJ configurations for a varying T_i and T_{amb}

T_{amb}/T_i [°C]	-5	0	5	10	15
15	29.6	38.9	47.3	54.3	61.3
17	23.0	33.1	41.8	49.8	57.9
20	14.9	25.6	34.9	43.5	52.3
22	8.7	20.0	30.0	39.1	48.0
25	3.6	11.8	29.0	32.2	41.1
27	7.0	6.8	17.7	27.8	36.8
30	-3.8	0.3	3.7	8.2	17.6
32	-6.8	-2.5	0.6	4.0	6.8
35	-11.6	-6.2	-2.6	0.1	3.0
38	-16.6	-9.1	-5.6	-2.5	0.2
40	-19.6	-11.0	-6.6	-3.7	-1.5
42	-23.4	-13.3	-7.5	-4.7	-2.3
45	-26.3	-16.5	-8.6	-5.3	-3.3

Is possible to observe that the EJ-AUX configuration is more convenient for a decreasing ambient temperature and an increasing internal space temperature. On the other hand, in a hot climate and low internal space temperature, the EJ configuration is the most convenient.

4.8.3. Evaluation of the net COP of the refrigerating system

In this section, the comparison between the performance of the cooling unit operating according to the three different configurations is discussed. To consider the total electric power absorption of the

refrigerating system given by the semi-hermetic compressor and the fans of the finned-coil heat exchangers, the net coefficient of performance COP^{net} is introduced, according to Eq. 4.35 for BP and EJ configuration and Eq. 4.36 for EJ-AUX configuration:

$$COP_{BP/EJ}^{net} = \frac{\dot{Q}_{eva}}{P_{el,comp}+P_{el,fans\ eva}+P_{el,fans\ g-c}} \quad (4.35)$$

$$COP_{EJ-AUX}^{net} = \frac{\dot{Q}_{eva}+\dot{Q}_{eva,AUX}}{P_{el,comp}+P_{el,fans\ eva}+P_{el,fans\ eva-AUX}+P_{el,fans\ g-c}} \quad (4.36)$$

Table 4.20 and Table 4.21 report the percentage variation between the net coefficient of performance of the EJ and EJ-AUX configuration, compared with the traditional BP configuration, using the same formula provided in Eq. 4.30.

Table 4.20 – $\Delta COP^{net}{}_{\%}$ between the EJ and BP configurations for a varying T_i and T_{amb}

T_{amb}/T_i [°C]	**-5**	0	5	10	15
15	-35.4	-55.5	-77.9	-103.6	-134.2
17	-23.6	-41.2	-61.1	-83.8	-110.3
20	-10.7	-26.2	-42.8	-62.3	-84.0
22	-2.8	-17.5	-33.0	-50.7	-70.5
25	2.0	-6.9	-20.9	-36.3	-54.1
27	2.5	2.9	-9.1	-23.0	-37.8
30	8.5	4.9	2.2	-1.8	-12.2
32	10.9	7.8	4.9	2.2	-0.1
35	14.1	10.3	7.8	5.2	3.2
38	15.9	12.0	9.0	7.1	4.7
40	15.6	12.3	9.4	7.3	5.2
42	16.1	12.7	9.0	7.0	5.1
45	13.0	12.3	8.2	5.3	3.7

From Table 4.20 is possible to observe that, for the EJ configuration, the net coefficient of performance follows the same trend of the coefficient of performance which did not consider the fans' electric power draw, thus confirming the convenience of the ejector cycle configuration over the traditional one when the system operates in hot climates, due to the work recovery provided by the two-phase ejector which allows to increase the operating pressure of the low pressure receiver.

On the other hand, the same trend is not observed for the EJ-AUX configuration, reported in Table 4.21.

Table 4.21 – $\Delta COP^{net}_{\%}$ between the EJ-AUX and BP configurations for a varying T_i and T_{amb}

T_{amb}/T_i [°C]	-5	0	5	10	15
15	-4.3	-4.2	-3.8	-4.0	-2.0
17	-3.9	-3.3	-3.0	-2.4	0.8
20	-3.3	-3.1	-2.7	-2.1	1.2
22	-3.0	-3.1	-2.6	-1.9	0.5
25	-3.5	-3.2	4.8	-2.1	-1.3
27	1.0	1.1	1.7	2.2	3.1
30	-3.2	-2.9	-2.3	-1.8	-1.2
32	-2.9	-2.2	-2.1	-1.6	-1.2
35	-3.4	-2.5	-1.7	-1.7	-1.1
38	-5.8	-2.8	-2.7	-1.8	-3.3
40	-8.9	-4.2	-3.1	-2.5	-2.6
42	-11.6	-5.9	-4.2	-3.5	-3.3
45	-18.4	-9.3	-5.9	-5.7	-5.4

The numerical model showed that if the net coefficient of performance is considered, the EJ-AUX configuration is barely convenient for a reduced range of temperature (T_{amb}= 27 °C). This is due to the fact that the reduction of electric power absorption at the semi-hermetic compressor is unable to counterbalance the additional electric power absorption introduced by the fans of the auxiliary evaporator, which in this study operates at fixed speed.

4.9. Conclusions

In this chapter, the numerical investigation of a new refrigerating system using CO_2 as the working fluid for refrigerated transport application is presented. A numerical model of the refrigerating system is developed to predict its thermal performance under different ambient conditions and to discuss on the best configuration ensuring the maximum COP during operation.

- Initially, a mathematical model of the system is developed with the software MATLAB to assess its performance during steady state operation. The dimensions of the main components of the system were chosen among real components available on the market.
- The numerical model was then utilized to compute the thermal performance of the refrigerating system in ATP test conditions ($T_{air,IN}$ =-2 °C, T_{amb}=30 °C) for 0 °C-class

refrigerated vehicle, assessing an increase by 4% of COP and 4.5% of refrigerating capacity if the configuration using a two-phase ejector were to be used instead of the traditional cycle.

- In order to evaluate the system configuration ensuring the best performance (COP) during operation of a refrigerated vehicle, which is characterized by high variability of the external temperature $\mathrm{T_{amb}}$, the COP of different system configurations is compared at the same refrigerated cargo space temperature ($\mathrm{T_{air,IN}}$=-2°C) but with different ambient temperature, which is varied in the range 15 °C-40 °C. It is observed that while the configuration of the system using the selected non-adjustable ejector can be utilized only with hot ambient temperatures (higher than 28 °C), the COP of the refrigerating unit using this configuration is higher than the COP of the traditional cycle, with a maximum of 11.5% and 14.8% for COP and refrigerating capacity respectively, for an ambient temperature of 38 °C.
- Furthermore, the possibility of utilizing an auxiliary evaporator was considered, assessing that if the auxiliary evaporator were to be sized identically to the evaporator utilized in the previous configurations ($\mathrm{KS_{AUX}/KS_{EVA}} \cong 1$), an increment of 11% on COP would be obtained respect to the traditional cycle at 30 °C ambient temperature and -2 °C cargo space temperature.
- After a preliminary evaluation of the performance of the system operating according to three different configurations in steady state condition which demonstrated its feasibility, a more accurate numerical model was developed with the commercial software AMESim, able to reproduce the operation of the refrigerating system even in unsteady conditions. In order to increase the accuracy of the model and better predict the performance of the heat exchangers, the simulation of the heat exchangers is obtained with a 1-D numerical model, where the device is approximated with a counter-flow heat exchanger and discretized in 6 elements, each modelled with a lumped capacitance which considers the refrigerant flow, the thermal mass of the tubes and fins and the external flow.
- The three different operating configurations of the refrigerating system were simulated assuming a constant internal space air temperature of -2 °C and an external ambient temperature between 15 °C and 45 °C: it was found that the configuration using a two-phase ejector and a single evaporator was convenient for an ambient temperature higher than 26 °C, with a maximum percentage advantage on COP, over the traditional BP configuration, equal to 13.8% for an ambient temperature of 42 °C. Evaluated at the same conditions, the refrigerating system operating according to the EJ-AUX configuration demonstrated to be more convenient than the classical one at all ambient temperatures below 36°C, extending the operating range of the two-phase ejector to subcritical operation of the refrigerating system. The EJ-AUX configuration had a maximum convenience of 6.4% for an ambient temperature of 20 °C.
- As the refrigerated transport is characterized by a high variability of internal and external environment temperature, the operation of the system according to the three possible configurations BP, EJ and EJ-AUX, was evaluated for an internal temperature comprehended between -5 °C and 15 °C and an external temperature varying in a range between 15 °C and 45 °C. The numerical model assessed that the EJ configuration had a maximum advantage on COP over the traditional configuration equal to 15.9 % for an internal space temperature and

external ambient temperature equal to -5 °C and 42 °C respectively. The maximum advantage on COP assessed by the numerical model for the EJ-AUX configuration compared to the BP configuration was equal to 14.2 % for an internal space temperature and external ambient temperature equal to 5 °C and 25 °C, respectively.

- The study of the performance of the refrigerating system operating in three different configurations, with varying internal and external temperature, assessed that the EJ configuration is more convenient when the system is operating in a hot climate with a low internal space temperature. On the other hand, when the internal space temperature is increased (i.e. during pull down operations which are necessary after each door opening operation) and the system is operating in subcritical conditions, the EJ-AUX configuration is better performing.
- Lastly, the net coefficient of performance was considered, taking into consideration the electric power absorption of the fans of the evaporators and gas-cooler. While the EJ configuration confirmed its advantage over the BP configuration for the same temperature range since the previous COP does not consider the additional electric power absorptuon, the EJ-AUX configuration demonstrated that the advantage of the EJ-AUX configuration is very limited, as the fans of the two evaporator operate at fixed speed, opening the discussion to the optimization of fans speed control in the EJ-AUX configuration.

The numerical models of the refrigerating system developed in this study will be coupled to the dynamic model of the insulated body previously developed to simulate the performance of a refrigerated vehicle in a typically delivery mission.

References

[1] T. Michineau, G. Cavalier, E. Devin. F-gases in refrigerated transport. Proceedings of the 3rd IIR International Conference on Sustainability and the Cold Chain, 2014. London, England: The Institute of Refrigeration.

[2] Ge Y.T., Tassou S.A:, 2009. Control optimisation of CO2 cycles for medium temperature retail food refrigeration systems. International Journal of Refrigeration, 32, 1376-1388.

[3] Besagni, G., Mereu, R., Inzoli, F., 2016. Ejector refrigeration: a comprehensive review. Renew. Sust. Energy Rev. 53, 373–407.

[4] Ge Y.T., Tassou S.A. Thermodynamic analysis of transcritical CO2 booster refrigeration systems in supermarkets. Energ Convers Manage 2011;52(4):1868-75.

[5] Gullo P., Konstantinos T., Hafnera A., Geb Y., Tassou S.A., 2017. State-of-the-art technologies for transcritical R744 refrigeration systems – a theoretical assessment of energy advantages for European food retail industry. Energy Procedia. 123, 46-53.

[6] Koury R.N.N, Faria R.N, Nunes R.O., Ismail K.A.R., Machado L. 2013. Dynamic model and experimental study of an air-water heat pump for residential use. International Journal of Refrigeration 36, 674-688.

[7] Bendapudi S., Braun J.E., 2002. A review of literature on dynamic models of vapor compression equipment. ASHRAE Report, no.4036-5.

[8] Rasmussen B.P. 2002. Control-Oriented Modeling of a transcritical vapor compression systems (Master thesis). University of Illinois, Urbana-Champaign.

[9] S. Minetto, 2011. Theoretical and experimental analysis of a CO2 heat pump for domestic hot water. International Journal of Refrigeration, 34(3): 742-751.

[10] R.F. Shi, D.G. Fu, Y.S. Feng, J.Q. Fan, S. Mijanovic, T. Radcliff, 2010. Dynamic modelling of CO2 Supermarket Refrigeration System. International Refrigeration and Air Conditioning Conference. Paper 1127.

[11] N. Lawrence, S. Elbel, P.Hrnjak, 2018. Design and validation of a transcritical CO2 mobile refrigerated container system for military applications. Proceedings of 13th IIR Gustav Lorentzen Conference, Valencia.

[12] Banasiak K, Hafner A, Kriezi EE, Madsen KB, Birkelund M, Fredslund K., 2015. Development and performance mapping of a multi-ejector expansion work recovery pack for R744 vapour compression units. Int. J. Refrigeration; 57, 265-276.

[13] Dugaria, S., Calabrese, L., Azzolin, M., Minetto, S., Del Col, D., 2018. Energy analysis of CO2 refrigeration systems using measured values of compressor efficiency. Proceedings of 13th IIR Gustav Lorentzen Conference, Valencia.

[14] Chen Y, Gu J. The optimum high pressure for CO2 transcritical refrigeration systems with internal heat exchangers. International Journal of Refrigeration 2005;28:1238-49.

[15] Jolly P.G., Tso C.P., Wong Y.W., Ng S.M., 2000. Simulation and measurement on the full-load performance of a refrigeration system in a shipping container. Int. J. Refrigeration; 23:112-126

[16] F.C. McQuiston Finned tube heat exchangers: state of the art for the air side ASHRAE Trans, 87 (1) (1981), pp. 1077-1085Mc-Quiston.

[17] Chen JC. A correlation for boiling heat transfer to saturated fluids in convective flow. ASME Paper 63-HT-34 (1963).

[18] Dittus, F. W. and Boelter, L. M. K., Heat transfer in automobile radiators of the tubular type. University of California Publications in Engineering, 1930,2,443461.

[19] Elbel, Stefan Wilfried and Hrnjak, Predrag S., "Effect of Internal Heat Exchanger on Performance of Transcritical CO_2 Systems with Ejector" (2004). International Refrigeration and Air Conditioning Conference. Paper 708.

[20] Elbel, S., & Hrnjak, P. S., 2008. Experimental validation of a prototype ejector designed to reduce throttling losses encountered in transcritical R744 system operation. International Journal of Refrigeration, 31(3), 411-422.

[21] United Nations, Agreement on the international carriage of perishable foodstuffs and on the special equipment to be used for such carriage (ATP), UNECE Transport Division, Geneva, Switzerland, 1970.

[22] Benedict, Manson; Webb, George B.; Rubin, Louis C. (1940), "An Empirical Equation for Thermodynamic Properties of Light Hydrocarbons and Their Mixtures: I. Methane, Ethane, Propane, and n-Butane", Journal of Chemical Physics, 8 (4): 334–345.

[23] B.P. Rasmussen, 2005. Dynamic modelling and advanced control of air conditioning and refrigeration systems, Ph.D. thesis, University of Illinois at Urbana-Champaign, USA.

Modello Jolly contro corrente

[24]] McQuiston, F.C., 1978. Correlation of heat, mass and momentum transport coefficients

for plate-fin-tube heat transfer surfaces with staggered tubes. ASHRAE Transactions, Vol. 84, No. 1, pp. 294-309.

[25] D. Steiner, J. Taborek. Flow boiling heat transfer in vertical tubes correlated by an asymptotic mode. Heat transfer engineering, Vol.13, pp 322-329.

[26] V. Gnielinski, 1976. New equations for heat and mass transfer in turbulent pipe and channel flow. Int. Chem. Eng. 16,359-368.

[27] L.Friedel, 1979. Imrpoved friction pressure drop for horizontal and vertical two-phase pipe flow. Europ. Two-phase Flow Group Meet, Paper E2, Ispra.

[28] S.W. Chiurchill, 1977. Friction-factor equation spans all fluid flow regimes. Chem. Eng. 7, 91-92.

[29] M.M. Shash, 1979. A general correlation for heat transfer during film condensation inside pipes. International Journal of Heat and Mass Transfer, Vol.22, pp 547-556.

[30] Elbel, S., Hrnjak, P., 2008. Experimental validation of a prototype ejector designed to reduce throttling losses encountered in transcritical R744 system operation. Int. J. Refrigeration 31,411-422.

5. Modelling of a refrigerated truck during a delivery mission

In this chapter, the numerical models of the refrigerating system developed in chapter 4 are coupled with the dynamic model of the insulated body presented in chapter 3 to simulate the performance of a refrigerated vehicle in a typical delivery mission. During a typical mission, the thermal load of a refrigerated vehicle is affected by both the external environment and operating conditions, dictated by the mission profile (number of stops, door opening operations, cargo loading/unloading).

In a typical refrigerated transport system operation, the refrigeration unit interacts with the truck cargo space and regulates its temperature to a certain set-point, depending on the type of transported goods. By far, the most common temperature control in the refrigerated transport having a cooling unit based on a vapor compression cycle is a simple on-off feedback controller with hysteresis (James et al. 2006 [1]), where the compressor ON or OFF control action is driven by the difference between measured cargo space temperature and set-point temperature.

After all, the maintenance of an optimal product temperature should be assured from production to consumption. The postproduction handling chain (perishable freights distribution and delivery) is one of the weakest links in the cold chain, especially in short or medium distance delivery runs where the chilled or frozen products can be subjected to many doors opening, with relevant heat loads directly related to infiltration air (James et al. 2006 [1]; Pereira et al. 2010 [2]). Frequent door openings can also lead to increased evaporator frosting, resulting in a reduction of the evaporator's performance and an increase in the need for defrosts, particularly in humid weather conditions (Estrada-Flores et al. 2006 [3]).

The performance of the small refrigeration units can be significantly reduced by the absence of a proper control of the cooling capacity, which is often driven by the power available at the vehicle engine. This is the case of the refrigeration units of small trucks, where the compressor is powered

by the vehicle's internal combustion engine. As a result, there are substantial difficulties in maintaining the optimal temperature of refrigerated products and proper cycling, especially when multi-drop deliveries to retail stores and caterers are considered (James et al. 2006 [1]). In this case, in fact, the cooling demand presents strong fluctuations due to the repetition of pull-down periods, associated to the door openings, and the driving time.

To investigate and improve the refrigeration system performance, good knowledge of the system behaviour is required: this knowledge can be obtained from modelling and simulation tools which offer an economic alternative to physical experiments, though a reliable model needs to be validated with experimental data.

In this chapter, the performance of a simple vapour compression cycle, when coupled to a small

refrigerated truck employed in a daily delivery mission, is evaluated by means of an unsteady simulation. A typical delivery mission profile characterized by a total of 12 door opening operations where the doors of the insulated body are kept wide open and the external air ingresses directly from the external environment is considered.

5.1. Numerical modelling of a refrigerated van in a short distance delivery mission using the software MATLAB

In this study, the cooling unit coupled with the refrigerated van's insulated box is modelled after a basic R-134a vapour compression system. The reference operating scheme and corresponding cycle reported in the p-h diagram is provided in Figure 6.1: the refrigerant enters the semi-hermetic compressor (a) suction line in the state of superheated vapour (1) and is compressed to the condensation pressure before flowing in the finned-coil condenser (b) where rejects the heat to the external environment. After that, the refrigerant now in the state of subcooled liquid is expanded to the evaporation pressure by a thermostatic expansion valve (TXV) (c_1), coupled with a sensing bulb (c_2) to ensure a constant superheating of the refrigerant at the outlet of the evaporation process, and the resulting two-phase mixture flows in the finned-coil evaporator (d) before the superheated vapour enters the compressor suction line.

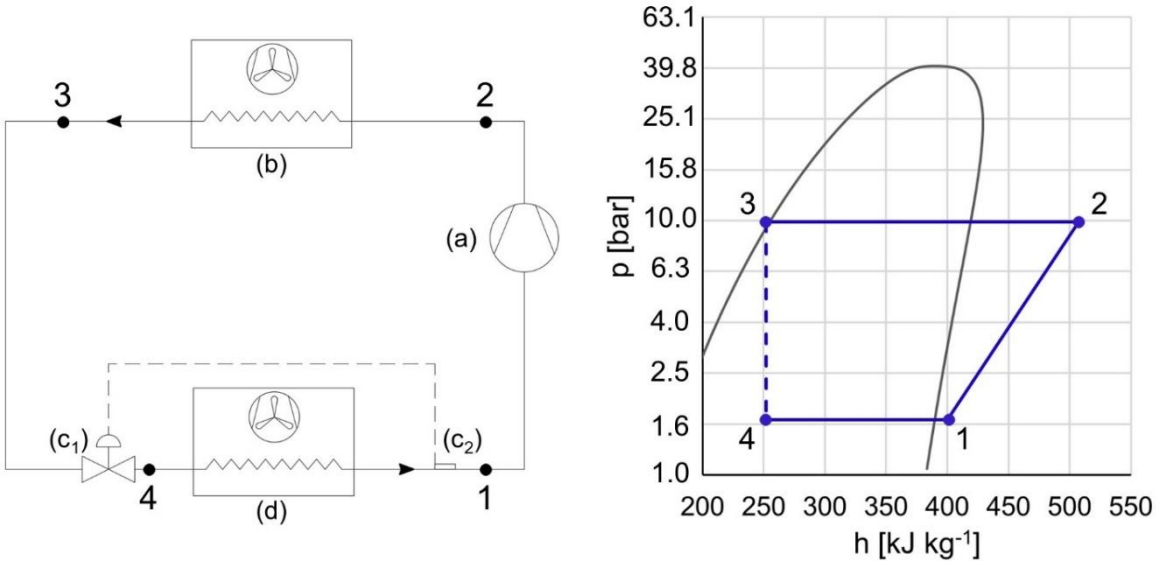

(a) (b)

Figure 5.1 – (a) Reference cycle operating scheme (b) Thermodynamic cycle of the refrigerating system in the diagram p-h

The refrigerating performance of the cooling unit is modelled with the numerical model presented in the previous chapter (see chapter 4, section 4.5), which determined the value of the total refrigerating capacity $\dot{Q}_{eva}$ and COP given the geometric dimensions of the main components and the temperature of the air at the inlet of the evaporator ($T_{air,IN}$) and condenser (T_{amb}) as input. In the numerical model, a constant approach point temperature difference ($\Delta T_{ap,cond}$ =7 K) and subcooling ($\Delta T_{sc,cond}$ = 2 K) are set at the condenser: the condensation temperature is then defined as $T_{cond} = T_{amb} + 9$ K. In the evaporator heat exchanger numerical model, the evaporation temperature T_{eva} is chosen to ensure a constant superheating of the refrigerant leaving the coil (ΔT_{sh}=10 K). Furthermore, as previously discussed, in the evaporator numerical model only sensible heat exchange is considered, as the model does not consider the presence of humidity and thus neglects dehumidification process and water condensation in the external surface of the finned coil.

The main dimensions of the finned-coil evaporator and semi-hermetic compressor, which must be given as input to the numerical model, are provided in Table 5.1.

Table 5.1 – Refrigerating system's main components

Component	Dimensions
Finned-coil evaporator	External convective area, $A_e = 8.7\ m^2$
	Air volumetric flow rate, $\dot{V}_{air} = 680\ m^3h^{-1}$
Semi-hermetic compressor	Displacement $V_d = 121.9\ cm^3$

With this dimensions, the cooling unit has a nominal cooling power of 2.1 kW, evaluated at the reference conditions of $T_i = 0\ °C$ and $T_{amb} = 30°C$, which was evaluated from a typical refrigerating unit for insulated vans employed in local distribution missions. The modulation of the refrigerating capacity provided to the cargo space $\dot{Q}_c$ is obtained by turning ON and OFF the compressor. The ON/OFF controller is implemented by means of a simple thermostat with 2 °C hysteresis.

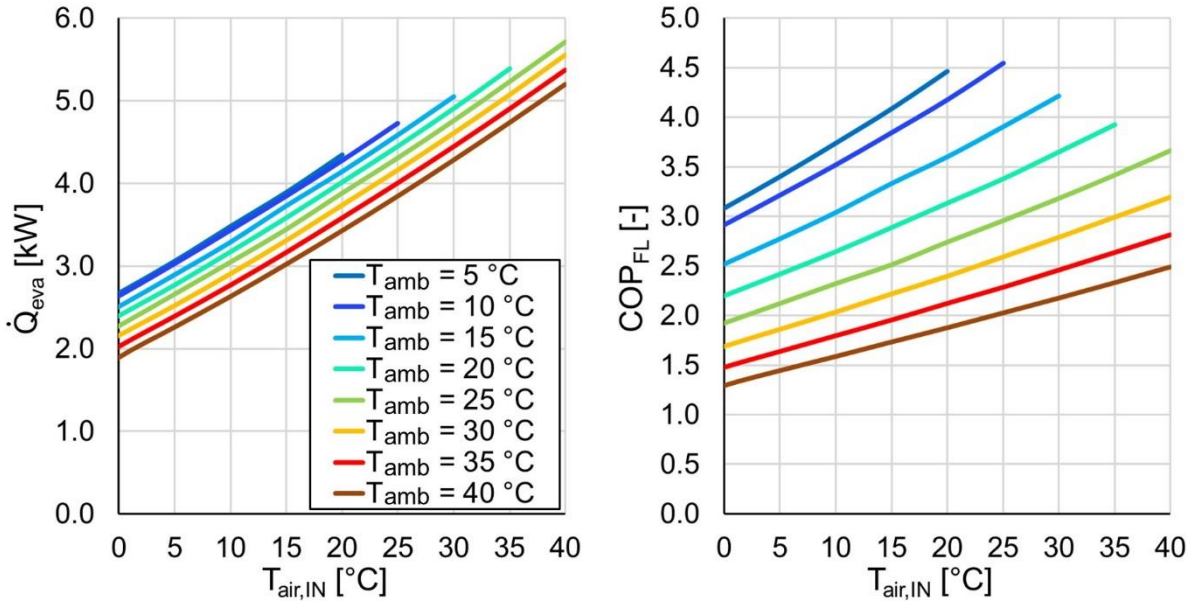

Figure 5.2 – Performance mapping of the refrigerating system: (a) refrigerating capacity (b) COP at full load

The performance maps reported in Figure. 5.2 for both refrigerating capacity and coefficient of performance at full load, are then implemented in the truck model by means of interpolation tables. Interpolation is based on the mean internal air mean temperature, which is assumed to be equal to the evaporator's air inlet temperature $T_{air,IN}$, and on the external environment temperature T_{amb}, resulting in the refrigerating capacity $\dot{Q}_c$ and the full load coefficient of performance COP_{FL}. In order to account for the reduction of the performance associated with ON/OFF cycles, a degradation factor was included in the model. The degradation factor C_d is assumed equal to 0.25, in accordance with

UNI-EN-14825 (2012), while the capacity ratio C_R is assumed equal to the mean duty cycle during operation. The resulting coefficient of performance at partial load is then obtained as:

$$COP_{PL} = COP_{FL}(1 - C_d(1 - C_R)) \tag{5.1}$$

The refrigerating capacity is implemented in the internal air heat balance of the numerical model of the refrigerated van, in accordance with equation 5.2:

$$C_i \frac{dT_i}{dt} = \dot{Q}_{convi} + \dot{Q}_{im} + \dot{Q}_{inf} - \dot{Q}_c \tag{5.2}$$

The numerical model of the refrigerated van is the same presented and validated in chapter 3 (see section 3.2.2), which refers to a refrigerated van with an internal air volume of 9.8 m^3. The walls of the insulated body are modelled with a formulation of a 0-D time-varying lumped capacitance method and are discretized using a series of 12 thermal capacities and 11 thermal resistances.

5.1.1. Definition of the delivery mission

A local distribution activity is simulated. The mission starts with the pre-cooling activity of the insulated body, as common practice in the industry, when the cooling unit is kept on with the doors closed and the internal air is pulled down to the set-point temperature, reaching a steady state condition while the refrigerated vehicle is kept still under the fluctuating ambient conditions. After two-hours of pull down, the cooling unit is switched off and the loading operation takes place: the perishable cargo is loaded inside the insulated body, while the refrigerated cargo space with the doors completely open is kept in contact with a controlled environment at $T_{amb,environment} = T_i^{set} = 4\ °C$ and the perishable cargo is already at the set-point temperature when is loaded.

Standard profiles for testing of emissions and fuel consumption from light duty vehicles ECE and EUDC [EEC Directive 90/C81/01] are then used to construct the delivery mission profile. Five EUDC cycle, corresponding to a 30 km drive, are used to simulate the rural drive condition between the logistic facilities to the city. Then the urban drive condition is defined as 5 ECE cycle, corresponding to 5 km in 15 minutes with frequent stops. The urban drive is repeated 6 times before a new rural cycle is performed. Between each urban cycle, a stop of 5 min is considered, where the doors are opened to the ambient for 4 minutes, and part of the refrigerated cargo is unloaded. This mission in then repeated during the afternoon.

In this delivery mission, a total of 400 kg of meat products are distributed evenly during the 12 deliveries.

Table 5.2 – Delivery mission structure

Start Time [h.mm]	Duration [h.mm]	Activity	Travel distance [km]
6.00 AM	2.00	Pull down	-
8.00 AM	1.00	Loading	-
9.00 AM	0.30	Rural drive	30
9.30 AM	2.00	6 delivery cycles	-
	0.17	- Urban drive	5
	0.01	- Stop	-
	0.04	- Delivery	-
11.30 AM	0.15	Urban drive	5
11.45 AM	0.30	Rural drive	30
12.15 PM	1.45	Stop	-
2.00 PM	0.30	Rural drive	30
2.30 PM	2.00	6 delivery cycles	-
	0.17	- Urban drive	5
	0.01	- Stop	-
	0.04	- Delivery	-
4.30 PM	0.15	Urban drive	5
4.45 PM	0.30	Rural drive	30
5.15 PM	-	Stop	-
TOTAL	11.15		190

5.1.2. Mission results

The numerical model was run to evaluate the average performance of the cooling unit, assuming different climates and different refrigeration unit size. Athens and Strasburg were identified as reference for hot and warm temperate climate, so to assess the impact of the ambient data on the results. Simulations were run in three typical days: 15th of March, 15th of June and 15th of August, assumed as representative days and the trend of the ambient temperature, provided by EnergyPlus database [4] and reported in Figure 5.3.

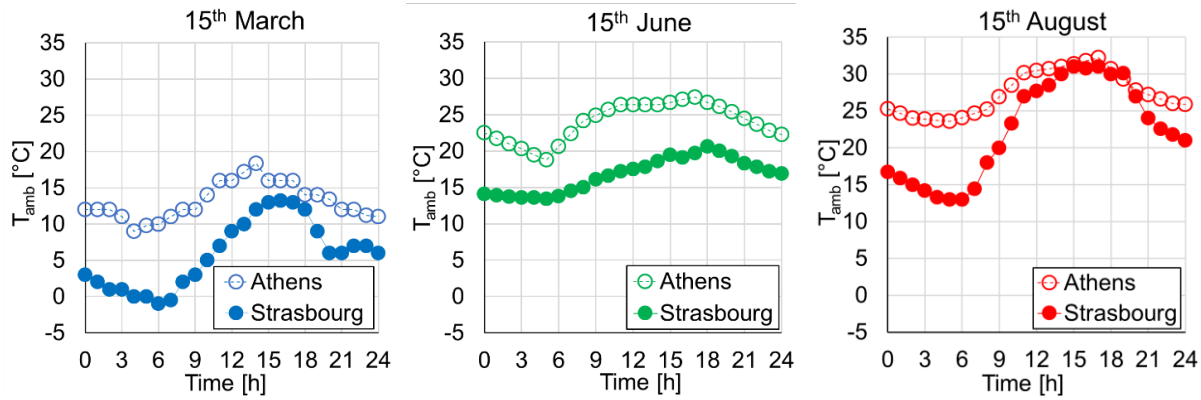

Figure 5.3 – Trend of the ambient temperature of Athens and Strasbourg (a) 15th March (b) 15th June (c) 15th August

First the response of the vehicle to the mission, in terms of temperature and loads using the expected capacity of the group $\dot{Q}c$ = 2.1 kW was evaluated. Then, the refrigeration unit size is discussed in terms of daily consumption and overall performance. The internal average temperature for each part of the delivery mission carried out the 15th August for both Athens and Strasbourg climate is reported in Figure 5.4, as well as the goods temperature and the ambient temperature identified as the internal mass temperature (T_{im}).

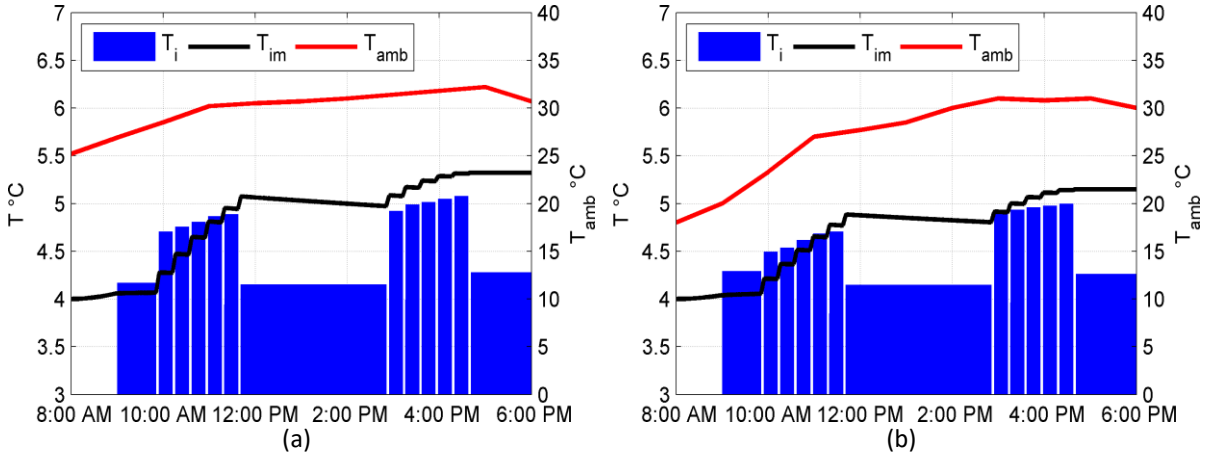

Figure 5.4 – Temperature trend for the mission carried out the 15th August (a) Athens (b) Strasbourg

As expected, the average internal temperature is close to set point of 4 °C during transport and the long stop at noon, when the doors are kept closed. On the contrary, during the delivery phase the average internal temperature increases, as the result of the hot ambient air entering the refrigerated box during the door opening. The increase after each stop does not represent in this case a cumulative effect, as the cooling unit can efficiently remove the heat from the air, but is caused by the increase in temperature of the infiltrating air, which reach its maximum in the late afternoon. On the contrary, the transported goods show a clear cumulative effect associated to the doors opening. The goods temperature increases steeply during each door opening, due to the high temperature difference with the infiltrating air, which promote the exchange. On the contrary, due to the relatively small

temperature difference $T_{im} - T_i$, the removal of the infiltrated heat from the goods is slow, as clearly shown by the small gradient of T_{im} between 12:00 AM and 13:00 PM, when the doors are kept closed.

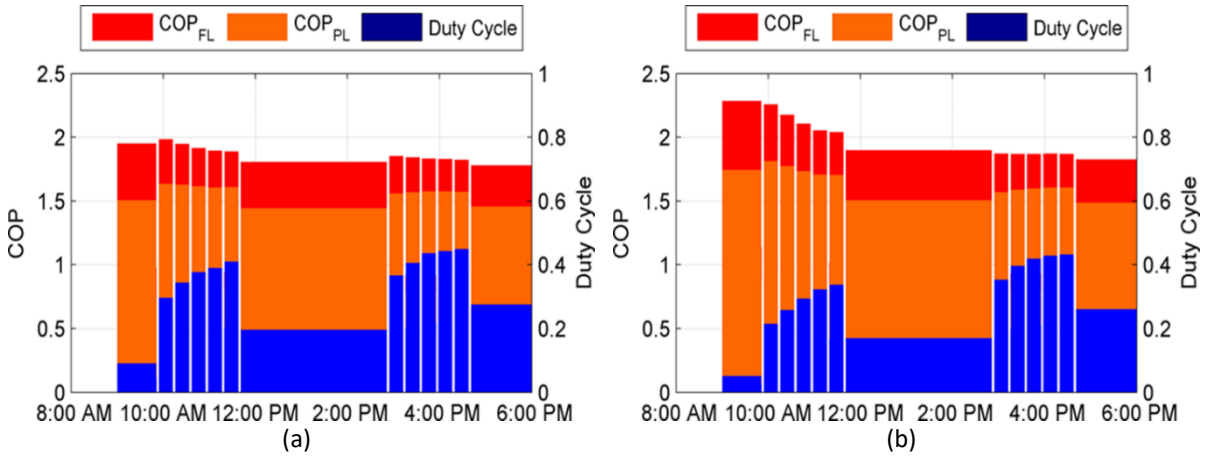

Figure 5.5 – Coefficient of performance and duty cycle (a) Athens (b) Strasbourg

Figure 5.5 reports the refrigeration unit performances for each part of the missions. Each graph reports the duty cycle, the full load and partial load coefficient of performance COP_{FL} and COP_{PL} respectively. When the full load performances are compared, the temperate climate in Strasburg allows obtaining significant higher COP_{FL} than in Athens. However, when the performance degradation ascribed to cycling is considered (Equation 5.1); the Strasburg data series present a marginal improvement only in the first hours of the morning. In fact, the lower cooling demand in Strasburg directly reduces the unit Duty Cycle, which is furthermore reduced by the increase of the capacity lead by the lower external ambient temperature.

5.1.3. Comparison between cooling capacities

As results of these observations, the ideal size of the refrigeration unit to complete the chosen mission is subject to antithetical requests. On one side, the unit capacity should be large enough to pull-down promptly the box temperature when the doors are closed, to reduce the temperature increase of the transported goods. On the other side, high capacities lead to small duty cycles thus reducing the actual energy performance. In order to discuss the optimum cooling capacity, the ATP limit capacity $\dot{Q}_{c,min}$ is considered, where:

$$\dot{Q}_{c,min} = 1.75\ K_{nom} S_m \Delta T_{nom} \tag{5.3}$$

with K_{nom}=0.7 $Wm^{-2}K^{-1}$ for refrigerated goods, S_m the average box surface euqal to 29.9 m^2 and ΔT_{nom}=30 K. This value was then used as the reference to define the capacity ratio $r = \dot{Q}_c/\dot{Q}_{c,min}$. For the considered test case, $\dot{Q}_{c,min}$ =1.1 kW. Simulation were then run with $r \in [0.6 ..5.1]$, for the 15th of March, the 15th of June and the 15th of August, for both the reference locations. Figure 5.5 report the daily average of COP_{PL} against the time for which $T_i > T_{set}^+$.

As expected, the increase of the group capacity decreases both the average efficiency and the exposure of the goods to high temperature. The sensitivity to the capacity ratio increases as the

average temperature increases. The exposure time of the goods to high temperature decreases by increasing of the capacity ratio, but it can't be reduced to zero, as it is bounded by the opening time (a total of 48 minutes in this mission) and the ambient condition which rules the air infiltration when doors are open.

The data presented in Figure 5.5 justify the choice of installing a 2.1 kW capacity unit ($r=1.8$) for the considered case, as an acceptable compromise between food safety and energy consumption. Further increase in the cooling capacity, in fact, has a marginal impact on the exposure time while decreasing the actual coefficient of performance.

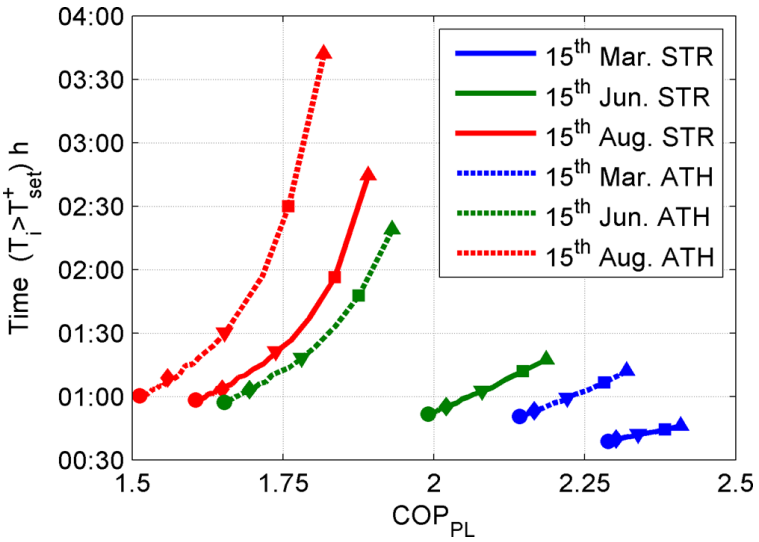

Figure 5.5 – Performance comparison between cooling capacities ratios: ▲ r = 0.6; ■ r = 07; ▼ r = 1.0; ♦ r = 1.8; ● r = 5.1;

In order to fulfil the two objective (quick pull-down and high efficiency), simulation were run assuming a step modulating unit, with a minimum capacity equal to $\dot{Q}_{c,min}$, and a maximum capacity equal to $r\,\dot{Q}_{c,min}$. A simple logic was implemented on the ON/OFF unit controller, using the highest capacity during the pull-down phases and the lowest when the temperature is inside the thermostat limits:

$$\dot{Q}_c = r\,\dot{Q}_{c,min} \text{ when } T_i > T^+_{set} \tag{5.4}$$

$$\dot{Q}_c = \dot{Q}_{c,min} \text{ when } T_i \in [T^-_{set}; T^+_{set}] \tag{5.5}$$

Results of this different control logic can be observed in Figure 5.6. The use of lower capacity when the temperature is between the thermostat hysteresis bounds allows increasing the average Duty Cycle during the mission, thus reducing the performance degradation due to partial loads (Eq. 5.1). Implementing this step control reduces the sensitivity of the average COP_{PL} to the capacity, when compared to the results in Figure 5.5.

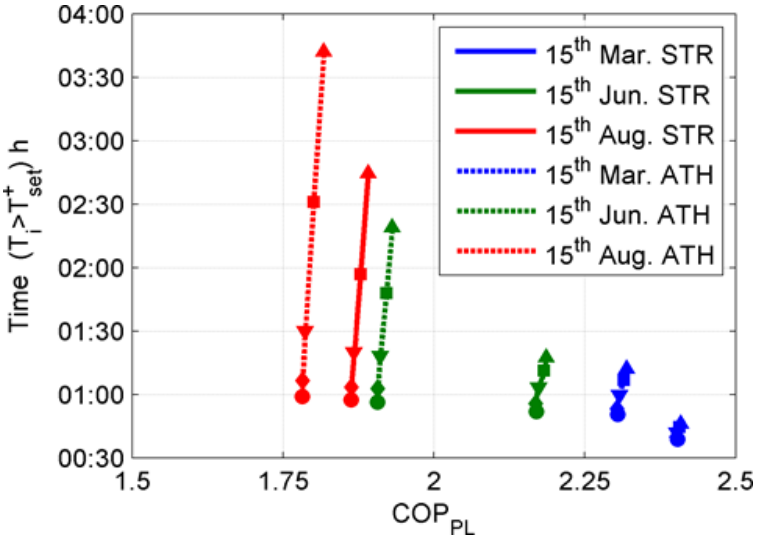

Figure 5.6 - Performance comparison between cooling capacities ratios: ▲ r = 0.6; ■ r = 07; ▼ r = 1.0; ♦ r = 1.8; ● r = 5.1;

5.1.4. Conclusions

In this section, a numerical simulation of a refrigerated van's insulated body during a short distance delivery mission is presented. Simulations are conducted for different climates and cooling capacities. Despite the simplicity of the model employed, results allow to discuss the impact of the cooling unit sizing on the overall performance, in terms of food security and energetic efficiency. While high capacities are needed to effectively pull down the temperature after each door opening, the low duty cycle of these units during the driving time can significantly reduce the overall performance of the system. The use of a step modulation of the unit capacity can positively affect the overall performance of the system, reducing the performance degradation at partial load.

In order to obtain more precise data further development of this research will be oriented to couple the refrigerated box dynamic model with a detailed dynamic model of the refrigeration unit.

5.2. Numerical simulation of a refrigerated van during a typical short distance delivery mission using the software AMESIM

In the previous section (5.1), the validated numerical model of the insulated body was coupled with the performance mapping of a cooling unit using R134a as the working fluid. The performance mapping of the cooling unit was obtained by means of the numerical model developed in the previous chapter (see section 4.1) which provided the refrigerating capacity $\dot{Q}_c$ and the coefficient of performance COP_{FL} of the refrigerating system operating in steady-state condition. However, even if ON/OFF cooling capacity control was implemented, the numerical model was unable to evaluate the transient phenomena occurring in the refrigerating system. Furthermore, the cooling unit implemented operated with R134a, which will be most likely phase out as an indirect consequence of the F-gas regulation: carbon dioxide is considered a promising substitute as a non-toxic and non-flammable refrigerant and benign to the environment. In this section, the thermal performance of a refrigerated van equipped with a cooling unit which utilizes carbon dioxide as the working fluid is assessed by

means of a dynamic simulation of both cooling unit and refrigerated cargo space, taking the climate of Athens as reference.

5.2.1. The refrigerating system dynamic model

A typical refrigerated transport system consists of a cooling unit and a refrigerated cargo space: the refrigerated unit interacts with the cargo space, ensuring the satisfaction of temperature requirements and cooling demand over a wide range of operating conditions. As the most common temperature control approach in refrigerated transport system is a simple on/off feedback controller with hysteresis [1], in the system considered in this study the compressor's ON/OFF control action is driven by the difference between mean cargo space temperature T_i, assumed equal to the evaporator return temperature $T_{air,IN}$, and the set-point temperature T_i^{set}, as can be observed in Figure 5.7. The other system actuators, such as gas-cooler and evaporator fans, operate with the same schedule as the compressor. In the numerical model, the cargo space of a refrigerated van is coupled to the cooling unit: the cargo space output, i.e. the mean internal air conditions, are the input to the refrigerating unit, i.e. the evaporator air inlet conditions. At the same time, the refrigerating unit output, i.e. the supply air conditions, are the inputs to the cargo space model.

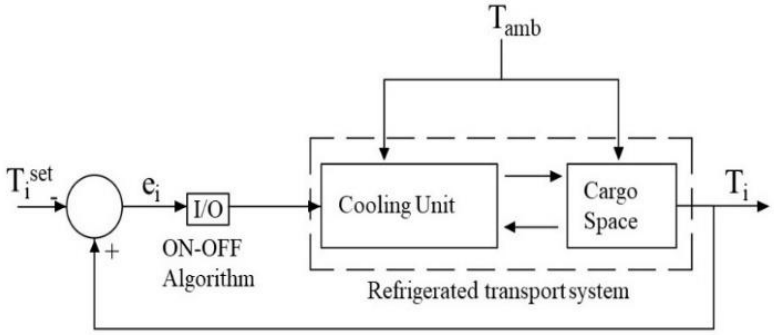

Figure 5.7 – Schematic of the refrigerated transport system model

Both dynamic models are obtained, and later coupled, with the software AMESim v.17 while ambient data are provided by EnergyPlus weather data[4]. The dynamic numerical model of the insulated body is the one presented and validated in chapter 4, i.e. the insulated body of a refrigerated van with an internal air volume of 9.8 m^3. However, differently from the previous numerical model, the insulated body's internal air considers the presence of air humidity as both energy and mass conservation equations are implemented. Consequently, the evaporator numerical model considers both sensible and latent heat transfer, since moisture condensation on the finned coil heat exchanger is considered.

The cooling unit considered in this study operates according to a traditional Low Pressure Receiver (LPR) cycle and utilizes a back pressure valve for expansion, in accordance with the configuration presented in the previous chapter (see section 4.3.1), which provides a full description of the system. The cooling unit's main components are a semi-hermetic compressor, a finned coil gas-cooler and evaporator, a back-pressure valve, a liquid-vapor separator and a regenerative heat exchanger. The compressor displacement has been resized for the cooling unit to have a nominal cooling power of 2.7 kW, evaluated ATP test conditions for 0 °C class vehicles, which is a typical cooling power for a refrigerated van designed for urban distribution activities.

The dimensions of the cooling unit's main components are chosen among real components available on the marked and are provided in Table 5.3.

Table 5.3 – Main dimensions of the components

Component	Dimension
Semi-hermetic compressor	Displacement $V_d = 12.9\ cm^3$
Finned-coil evaporator	External convective surface $A_{e,eva} = 36.4\ m^2$
IHX	Exchanging surface $A_{IHX} = 0.39\ m^2$
Finned-coil gas-cooler	External convective surface $A_{e,g-c} = 15.8\ m^2$

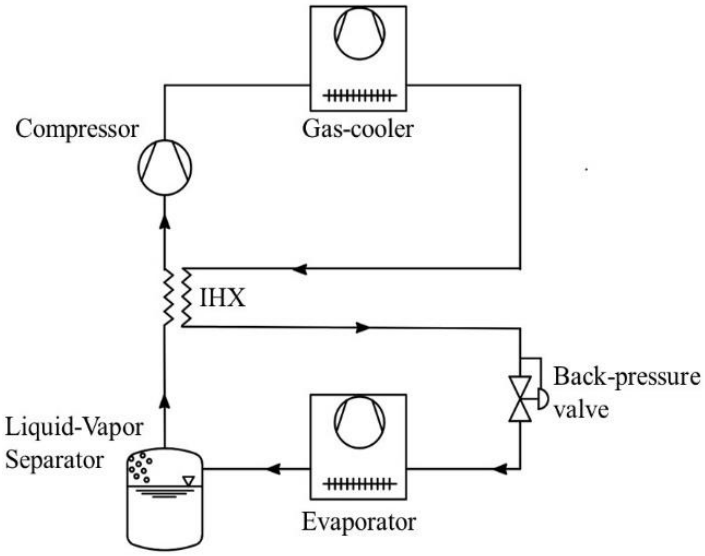

Figure 5.8 – Schematic of the refrigerating unit using carbon dioxide as working fluid and operating according a classical low pressure receiver cycle

Submodels of the semi-hermetic compressor, heat exchangers (evaporator, gas-cooler and IHX), expansion device, liquid-vapor separator and pipes are created using the two-phase flow library of AMESim, which also assesses the value of thermophysical properties of the refrigerant. Pressure losses in the internal flow are evaluated with the Mac-Adams[5] correlation while moist air pressure drop which occurs on the external flow of the evaporator and gas-cooler is neglected.

The control of the high pressure of the refrigeration unit, i.e. gas-cooler operating pressure, is achieved by means of a PI controller which modulates the cross-sectional area of the back-pressure valve in order to ensure the maintenance of the optimal gas-cooling/condensing pressure, evaluated as a function of the refrigerant temperature at the gas-cooler outlet, $T_{g-c,out}$, in accordance with Dugaria et al. 2018[6].

The semi-hermetic compressor is modelled as a fixed-displacement compressor: the value of volumetric efficiency η_V, overall compression efficiency η_C and the mechanical efficiency η_m, necessary to the submodel to evaluate mass flow-rate and power draw, are computed from the data

supplied by the compressor manufacturer. The nominal rotation velocity n during the ON-stage of the compressor is set equal to 1450 rpm and thus the mass-flow rate developed by the compressor can be calculated with equation 5.6:

$$\dot{m}_V = \frac{\rho_{in} V_d n}{60} \eta_V \tag{5.6}$$

The gas-cooler and the evaporator are modelled using a simplified approach which consists of a discretization of the heat exchanger using three basic elements: a pipe with heat exchange which represents the refrigerant flow with internal convective heat exchange, a thermal capacity representing the thermal structure of the heat exchanger and a convective moist-air component describing external convective heat exchange between the moist-air and the external wall, as reported in Figure 5.9. This simplified approach ensures that within the model, the transient processes involving internal refrigerant flow, wall thermal capacities and external heat transfer with moist air, are all taken into account without the necessity of a more complex and detailed model.

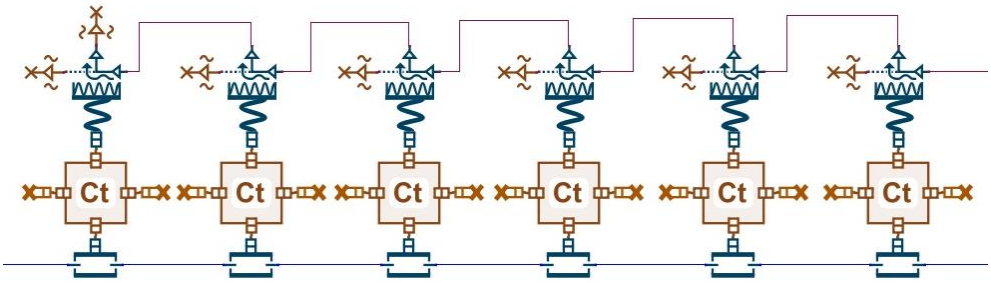

Figure 5.9 – Simplified approach of the dynamic modelling of the finned-coil heat exchanger

For both finned coil heat exchangers, coil-to-air heat transfer coefficients are calculated by Colburn j-factor correlations [7] while internal heat exchange is defined by empirical correlations. In the case of boiling process, which occurs in the evaporator, the Verein Deutscher Ingenieure (VDI) correlation [8] for horizontal tubes is implemented and thus the value of the internal heat transfer coefficient is computed depending on the contribution of nucleate boiling and forced convection. For the gas-cooler, in the case of subcritical operation, condensation occurs, the internal heat transfer coefficient is calculated using the Shash [9] correlation. For single phase conditions operating conditions eventually occurring in the evaporator (superheating), gas-cooling process (when the gas cooler operates in trans-critical conditions) and in the regenerative heat exchanger, Gnielinski correlation [10] is utilized. The air side boundary condition for these two heat exchangers is obtained with a moist air source submodel that simulates the air mass flow rate developed by the heat exchangers' fans which provide a boundary condition to the finned coil evaporators' submodels. The evaporator cooling coil extract both sensible and latent heat from the refrigerated cargo space, providing both cooling and dehumidification of the air inside of the cargo space. However, the evaporator's performance degradation due to the presence of frost on the heat exchanger external surface as well as defrost operation are neglected in this model. The regenerative heat exchanger is modelled with the same approach as the evaporator and gas-cooler, while the liquid-vapor separator is modelled as a constant cross-sectional area receiver and the liquid volume percentage is evaluated by solving mass and energy

conservation equations in the volume. The input required by the cooling unit model are the air conditions, i.e. dry bulb temperature, relative humidity and mass flowrate, at the evaporator and gas-cooler inlet. The main output provided by the model are the cooling power $\dot{Q}_c$, the electric power draw of the refrigerating unit which is equal to the algebraic sum of compressor and fans power draw, as well as air conditions at the outlet of the evaporator. The coefficient of performance of the cooling unit can be evaluated using equation 5.7:

$$COP = \frac{\dot{Q}_c}{P_{el,comp} + P_{el,fans-eva} + P_{el,fans-gc}} \tag{5.7}$$

The refrigerated van was set to carry out the same mission presented in the previous section (see section 5.1.1), which is a short distance delivery mission with a total of 12 door opening operations.

5.2.2. Simulation results

The numerical model was utilized to simulate the delivery mission for each month of the year, which is identified by a single reference day whose ambient conditions, i.e. ambient temperature, relative humidity and solar radiation, are obtained as a mean of their values during the month. Maximum, minimum and mean value of the external temperature T_{amb} for each month of the year is provided in Figure 5.9a, which in turn identifies February as the mildest month and August as the harshest.

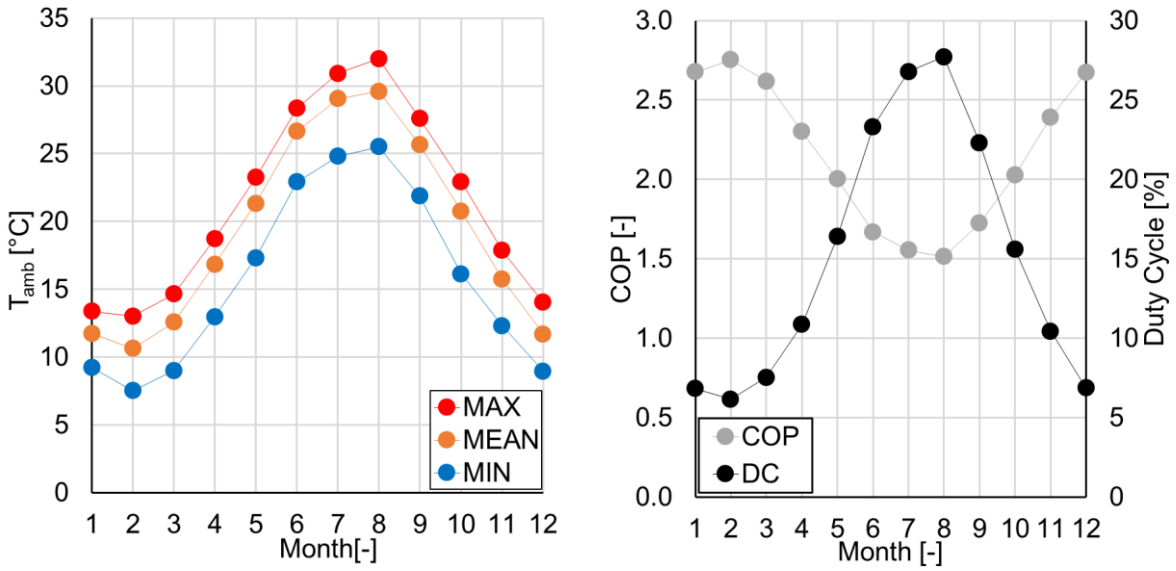

(a) (b)

Figure 5.9 – (a) Monthly COP and duty cycle during the year (b) Trend of the maximum, mean and medium ambient temperature during the year for the climate of Athens.

The model initialization is achieved by simulating the empty refrigerated van with the door closed under the fluctuating ambient conditions for 24 hours prior to the mission. For each simulation, the value of the mean coefficient of performance during the mission is obtained: Figure 5.9b reports the trend of mean COP and duty cycle, defined as the percentage ratio between the total on-stage time of the refrigerating unit and the total time in which the cooling unit is set on, during the mission for each

year. As expected, February presents the maximum value of COP, 2.8, and minimum duty cycle, 6%, while August has the minimum value of COP, 1.5, and maximum duty cycle, 26%.

The expected annual COP of the refrigerating system, evaluated with equation 5.8, is evaluated as the ratio between the whole cooling energy provided by the refrigerating unit and the whole electric energy the unit has consumed and represents the global performance of the cooling unit during the year.

$$\overline{\mathrm{COP}_{\mathrm{annual}}} = \frac{\sum_{j=1}^{12} \mathrm{E}_{\mathrm{cool,j}}}{\sum_{j=1}^{12} \mathrm{E}_{\mathrm{el,j}}} \tag{5.8}$$

Its value is equal to 1.9, which is a promising value, as the typical value of COP for refrigerated transport system that can be found in literature usually stays between 0.5 and 1.5.

5.2.3. Cooling energy consumption analysis

Differently from a long-transport mission, delivery missions are characterized by a high number of door openings, which cause a rapid increase of the internal air temperature and relative humidity that must be consequently reduced by the cooling unit. Numerical simulation can be utilized to evaluate the impact of the infiltration heat load, due to the frequent door openings, latent heat load, due to the humidity infiltration, and conduction heat load trough the walls of the refrigerated cargo during the delivery mission profile, as reported in Figure 5.10.

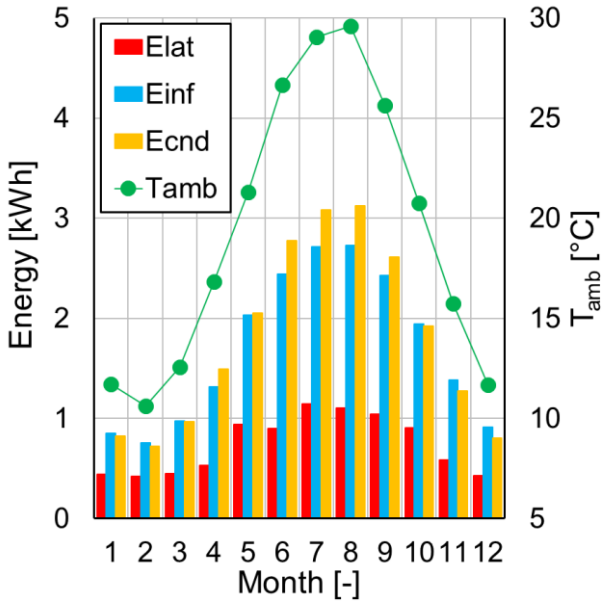

Figure 5.10 – Impact of latent heat load, infiltration heat load and conduction heat load during the mission

From the figure, it's possible to observe that the major role is played by infiltration and conduction, as latent heat load has a always a lower value during the year. The fact that infiltration heat load is comparable to the heat load given by conduction trough the walls highlights that the type of mission must be taken into account in the cooling unit sizing, since the cooling power required by the refrigerated cargo during a delivery mission will be much higher due to an important infiltration heat

load. Furthermore, as hot air enters the controlled environment, usually kept around 0 °C, cold air and hot air from the external environment mixes and condensation will most likely occur, as the cold air turns saturated. The condensation of water vapor on the good's surface may affect the quality of the product itself and thus solutions such as air curtains or strip curtains to reduce the heat and mass transfer through the open door should be taken into consideration.

5.2.4. Comparison between the performance of a cooling unit operating with R134a and CO_2 for the same delivery mission

In the previous sections, the same delivery mission was simulated for a refrigerated van equipped with a cooling unit using R134a (section 5.1) and CO_2 (section 5.2) as the refrigerant respectively. In order to compare the expected annual COP of the two refrigerating systems, defined in Eq. 5.8, the same delivery mission was simulated using the typical reference day of each month of the year, with the climate of Athens, as already reported in section 5.2.

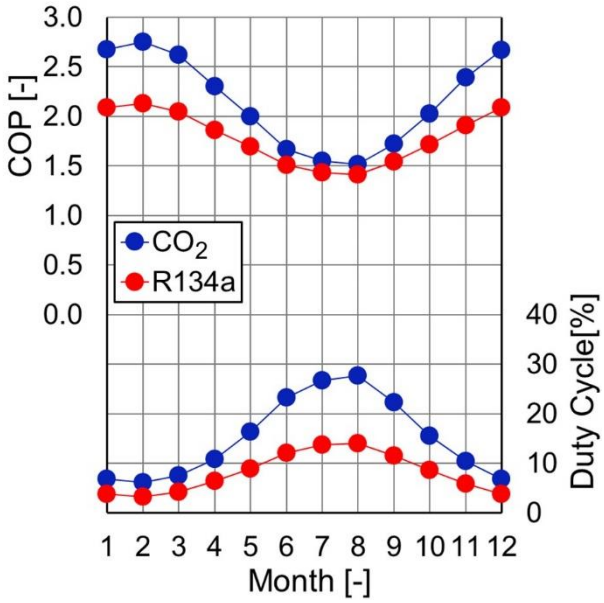

Figure 5.11 – Trend of the monthly COP and Duty Cycle for the two refrigerating systems using R134a and CO_2 as the refrigerant.

Figure 5.11 reports the trend of expected monthly COP and corresponding duty cycle for the two cooling units during the same delivery mission. The value of the expected annual COP is equal to 1.9 and 1.6 for the refrigerating system using CO_2 and R134a as the working fluid respectively.

5.2.5. Conclusions

In this study a dynamic simulation of a refrigerated vehicle during a typical delivery mission is presented. The dynamic model of the refrigerated cargo space is coupled with the dynamic model of a refrigerating unit using carbon dioxide as the working fluid, and the thermal performance of the system during the mission is evaluated:

- The thermal performance of a new cooling unit coupled with the refrigerated cargo space of a refrigerated van is assessed, providing an expected annual Coefficient Of Performance of 1.9 for the refrigerating system.
- Numerical simulation shows that for a delivery mission characterized by frequent door openings, infiltration heat load has an impact of the cooling energy provided by the refrigerating unit during the mission comparable to the one given by heat conduction through the insulated body walls. Thus mission profile plays an important role in the current dimensioning and sizing of the cooling unit, and in order to reduce hot air infiltration during door opening operations air curtains or plastic strips should be adopted.

Future developments are foreseen in modelling of performance degradation of the cooling unit due to presence of frost on the evaporator external surface and the impact of defrost cycling on the cooling power required by the refrigerated cargo space during the mission. A more detailed study of heat transfer phenomena occurring on the perishable cargo during the mission will be included, which will quantify the effective maintenance in high quality condition of the perishable foodstuff during the whole mission.

Reference

[1] James S.J., James C., Evans J.A., 2006. Modelling of food transport system- a review. Int.J.Refrigeration, 29: 947-957.

[2] Pereira V.F., Doria E.C., Carvalho jr B.C., Neves jr L.C., Silveira jr V., 2010. Evaluation of temperatures ina refrigerated container for chilled and frozen food transport. Ciencia e Tecnologia de alimentos, campinas, 30(1), 158-165.

[3] Estrada-Flores S., Eddy A., 2006. Thermal performance indicators for refrigerated road vehicles. Int. J. Refrigeration, 29: 889-898.

[4] Energy Plus Weather Data, EnergyPlus. <https://energyplus.net/weather location/europe_wmo_region_6/GRC//GRC_Athens.167160_IWEC >.

[5] McAdams, William H.: Heat Transmission. Third ed., McGraw-Hill Book Co. ,

Inc., 1954. Mac Adams.

[6] Dugaria, S., Calabrese, L., Azzolin, M., Minetto, S., Del Col, D., 2018. Energy analysis of CO2 refrigeration systems using measured values of compressor efficiency. Proceedings of 13th IIR Gustav Lorentzen Conference, Valencia.

[7] Colburn A.P., A method of correlating forced convection heat transfer data and a comparison with fluid friction, Trans AICHE, 29 (1933), pp. 174-210.

[8] Steiner, D.; Taborek, J. Flow boiling heat transfer in vertical tubes correlated by an asymptotic model. Heat Transf. Eng. 1992, 13, 43–69.

[9] Shah, M.M. A general correlation for heat transfer during film condensation inside pipes. Int. J. Heat Mass Transf. 1979, 22, 547–556.

[10] Gnielinski V. (1976). New equation for heat and mass transfer in turbulent pipe and channel flow. Int. Chemical Enginnering 16, 359-68

6. Conclusions

This study provides a deep analysis of a typical road refrigerated transport system. Each component of the system is considered: the insulated body where perishable goods reside, the cooling unit which ensures precise temperature control, and the mission profile which determines the dynamic solicitation on the insulated body and thus the thermal load that must be extracted by the cooling unit in order to ensure the maintenance of the desired set-point temperature inside of the cargo space.

The first component analysed was the insulated box, where perishable freights reside:

- The experimental data collected during the ATP test and the following step test of a brand-new refrigerated van were used to develop a fully dynamic numerical model of the refrigerated vehicle. The numerical model was achieved with a 0-D lumped capacity method, which is a simple and computationally efficient method utilized in the study of the transient thermal behaviour. The experimental data collected in the ATP tests were used to tune the model, while the experimental data collected during the following step tests were used for numerical validation, which demonstrated excellent agreement between simulated results and experimental data, with a maximum difference in the predicted average internal temperature equal to 0.3 K.
- The simple, reliable, 0-D lumped capacitance model avoided the need for a more complex numerical model requiring a detailed description of the box structure and materials, and the resolution of a 3D thermal model accounting for all the thermal pairs and bridges of the structure. Furthermore, during the tuning of the numerical model, it was possible to observe that the value of the wall's thermal capacity C_w and conductive resistance R_w could not be derived from the walls stratigraphy, as they would provide a rough approximation and could lead to significant errors. The best fit values of thermal capacity was found to be 47% higher than the one derived from stratigraphy while the best fit value of thermal resistance was evaluated by 23% lower than the one from stratigraphy.

After the development and validation of a simple reliable model able to replicate the dynamic behaviour of the box, the analysis of the refrigerating unit was performed. A cooling unit operating with a natural refrigerant (CO_2) was considered, since the choice of the refrigerant in refrigerated transport is undergoing a though revision as an indirect consequence of the F-gas regulation and synthetics refrigerants typically employed in this sector (R134a, R404A) are most likely to be phase out in a near future.

- The operating scheme of a new cooling unit using carbon dioxide as the working fluid was developed. With two thee-way valves and several circulation valves, the refrigerating system was designed to be able to switch among different operating configurations. In particular, the system can operate in both cooling and heating mode, where the system extracts or provides heat to the cargo space of a refrigerated vehicle, working as a heat pump. In cooling mode, the refrigerating system can operate according to a classical low pressure receiver cycle using a back-pressure valve for expansion and according to an ejector cycle using the parallel

between a fixed-geometry two phase ejector and a back-pressure valve. Furthermore, in the ejector cycle configuration, an auxiliary evaporator can be integrated in the line between the ejector outlet and the low-pressure receiver to extend the operating range of the ejector cycle to lower values of ambient temperature.

- A numerical model of the system operating in steady state condition was developed with the software MATLAB. The performance of the system operating in cooling mode, was determined according to the ATP test conditions for 0 °C refrigerated vehicles, where the return air temperature at the evaporator inlet is assumed to be equal to the mean internal air temperature of the vehicle of -2 °C and the external ambient temperature is equal to 30 °C. The numerical model assessed that the use of the ejector cycle configuration (with a single evaporator) ensures an advantage over the traditional configuration equal to 4% and 4.5% for the refrigerating capacity and COP respectively. Moreover, as refrigerated transport is characterized by a high variability of external ambient conditions, the ambient temperature was varied in a range between 15 °C and 40 °C, maintaining a constant internal space temperature of -2 °C. During this analysis, the numerical model could evaluate the functional limit of the two-phase ejector, as the ejector cycle could not find a steady state working point for an ambient temperature lower than 28 °C. For an ambient temperature higher than 28 °C, it was observed that the ejector system increases its advantage over the traditional cycle up to a maximum of 11.5% in COP and 14.8% in refrigerating capacity at 38°C ambient temperature. It was also possible to preliminary evaluate the advantage introduced using an auxiliary evaporator, in the ejector cycle, with the same geometrical dimension as the main one. The use of the auxiliary evaporator, for a fixed internal air temperature and a varying ambient temperature, can provide a constant advantage of 10-13% for both COP and refrigerating capacity over the traditional cycle configuration.
- As the previous numerical model could assess the performance of the refrigerating system only when operating in steady state conditions and was characterized by major assumptions and simplifications, a more detailed numerical model of the refrigerating system was developed with the software AMESim v.17, able to predict the theoretical performance of the system in both dynamic and steady state conditions. The performance of the three configurations of the refrigerating unit were investigated at varying internal cargo space temperature and external ambient temperature. The model assessed that the ejector cycle configuration was convenient during operation in a hot climate with a low internal space temperature (between -5 °C and +5 °C), compatible with the internal space temperature required during transportation of chilled products. Moreover, to extend the operation of the ejector cycle to lower values of ambient temperature, the ejector cycle using the auxiliary evaporator had to be employed. The ejector cycle presented the maximum advantage of 15.9 % on COP over the traditional configuration for an ambient temperature of 42 °C and an internal space temperature of -5 °C while the ejector cycle using the auxiliary evaporator presented the maximum advantage of 14.2 % over the traditional configuration for an internal space temperature of 5 °C and an ambient temperature of 27 °C.

- The net coefficient of performance $\mathrm{COP}^{\mathrm{net}}$, accounting for the electric power draw of the fans in the finned-coil heat exchangers, was considered. While the ejector cycle configuration demonstrated to be still more convenient than the traditional configuration when operating in a hot external environment at low internal space temperature, the convenience of the ejector cycle configuration considering the additive electric power draw of the fans was very limited, mainly for an ambient temperature equal to 27 °C. This was due to the fact that both evaporators were operating with fans at maximum speed, since velocity regulation of the fans in the evaporator was not implemented on the model, leading to a higher energy consumption. Future work will comprehend the optimization of the fans rotation velocity and thus electric power absorption as a function of the cooling power effectively provided by each evaporator.

Once the numerical model of the insulated body and the numerical model of the refrigerated system were obtained, the two models were coupled to fully simulate the entire system. The simulation of the complete refrigerated transport system assumes that the state of the air at the inlet of the evaporator equals the mean state of the air inside of the insulated body, while the state of the air at the inlet of the external heat exchanger is assumed to be equal to the state of the air identified by the external ambient conditions. The control of the cooling capacity was obtained turning ON and OFF the compressor, depending on the value of the internal air temperature and its difference from the set-point temperature. After that, a typical short distance delivery mission characterized by a total of 12 door opening operations, where heat enters directly from the external environment, is defined. During the mission, a total of 400 kg of meat carcasses is loaded in the insulated body and later distributed evenly during each delivery operation.

- First, the insulated body was coupled with the performance mapping of a simple vapour compression cycle operating with R134a as the working fluid (which is a widely used refrigerant in refrigerated transport applications). Different nominal refrigerating capacities of the refrigerating unit were investigated for three typical days of two different climates (Athens and Strasbourg), in order to test the system in a hot and mild climates. To determine the impact of the duty cycle on the performance of the refrigerating system, the coefficient of performance at partial load ($\mathrm{COP_{PL}}$) was defined and for each simulation it was coupled with the total time in which the internal air temperature exceeds the maximum allowable value $\mathrm{T}^{+}_{\mathrm{set-point}}$. Simulation results assessed that the nominal value of refrigerating capacity (2.1 kW) represents a good compromise between the time in which $\mathrm{T_i} > \mathrm{T}^{+}_{\mathrm{set}}$, which must be minimized to ensure safety of perishable freights, and the degradation of the $\mathrm{COP_{FL}}$,which is resposible of the highest energy consumption during the mission. An oversized cooling unit would ensure a minimum time where perishable freights would be exposed to high temperature and rapid pull down, but on the other hand, given the consequently increased duty, this would correspond to a low $\mathrm{COP_{PL}}$
- Assuming the same mission delivery mission profile, the dynamic, more accurate numerical model of the refrigerating system, utilizing carbon dioxide as the working fluid and operating according a traditional cycle was coupled with the dynamic model of the insulated body. An annual simulation of the typical delivery mission was performed,

assuming as reference the mean day of each month of the year. The numerical model assessed an annual COP of the refrigerating system equal to 1.9, which is a promising value since literature review assesses the typical COP of a refrigerated transport system between 0.5 and 1.5. Furthermore, with the numerical model, it was possible to evaluate and compare the impact of infiltration heat load, conduction heat load and latent heat load during the typical mission carried out in the annual simulation. It was determined that the infiltration heat load and conduction heat load had a comparable magnitude, which identified them as the main components to the heat load of the refrigerated vehicles, as the latent heat load played a minor role. It is clear then that the mission profile and the number of door opening operations and by extension the mission profile of the vehicle, play a major role into the correct dimensioning and sizing of the refrigerating unit of a refrigerated vehicle.

The numerical model of the refrigerated transport system (insulated body, cooling unit and mission profile) developed in this study was then able to determine the dynamic load of a refrigerated vehicle during a mission. Furthermore, numerical results could be utilized to evaluate how solar radiation, external convection, heat conduction and mission profile impact the cooling energy demanded by the insulated body, allowing an optimal sizing of the refrigerating system.

Considering the achieved results, the future research activity may look at:

- the actual build-up of the refrigerating system operating with carbon dioxide as the working fluid, for the validation of the numerical model of the refrigerating system in both dynamic and steady state conditions;
- the modelling of the performance degradation of the evaporator heat exchanger due to the presence of frost on the external surface of the finned coil heat exchanger and consequent defrost operation, which is needed for evaporation temperatures below 0 °C.

Appendix A: internal heating method for the assessment of the global heat transfer coefficient K

6.1. The ATP agreement

As an essential link in the cold chain, refrigerated transport systems are in charge of guaranteeing the delivery to the market of perishable freights in safe ad high-quality conditions. In 50 Countries all over the world, including Italy and many European Countries, the specifications for refrigerated vehicles and the way of testing them are covered by the International Agreement for the Transport of Perishable (ATP) [1], which regulates the transport of perishable foodstuff across borders and, in some cases including Italy, it has been adopted also for internal transport.

The ATP agreement was signed in Geneva on September 1, 1970 and entered into force on 21 November 1976. The objectives of the agreement are to facilitate the international transport of perishable freights during the carriage and applies to the carriage of perishable foodstuffs performed on the territory of at least two contracting states not only by road, but also by rail and by sea.

The equipment covered by the agreement concerns all types of refrigerated vehicles including insulated trailers, truck and van bodies (single and multi-compartment), and liquid-foodstuffs tanks. The ATP agreement prescribes, among other tests, the method to experimentally evaluate the overall heat transfer coefficient (K-value) of the insulated body. The experimental value of the K-value reflects the properties of the insulated body's insulation, design and manufacturing process.

6.2. Method and procedures for measuring and checking the insulating capacity of the insulated body of a refrigerated vehicle

The Annex 1 of ATP provides definitions and standards for the special equipment for the carriage of perishable foodstuff.

Due to the limited scope of this Appendix, that is to provide the necessary information to value the experimental data collected in this thesis in the ATP test station in Padua, among the different tests procedure presented in the ATP document, only the one relevant to this work will be presented that is the heating method for the evaluation of the global heat transfer coefficient K.

6.2.1. Measure Set-Up

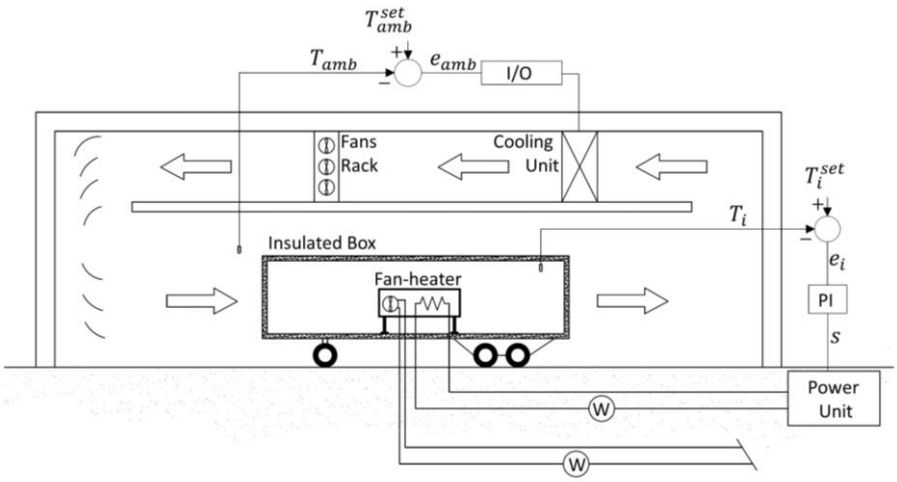

Figure A-1.1: Scheme of ATP test station and refrigerated semitrailer during a typical ATP test

The testing method is based on imposing a known and controlled thermal load by electrical heating inside of the insulated box through the use of fan-heaters.

During the test the internal and external temperature should be maintained at prescribed values, as well as the external air velocity at 100 mm from the body walls. Internal and external temperatures should be measured at 12 prescribed positions at 100 mm from the internal and external walls respectively.

The test is based on the average internal temperature T_i, the average external temperature T_e, the electrical power delivered by the fan heaters $\dot{Q}$ as the results of the electrical heating and the power required by the fans.

The overall heat transfer coefficient of the insulated body of a refrigerated vehicle is defined as follow:

$$K = \frac{\dot{Q}}{S_m \Delta T} \quad [W\ m^{-2}K^{-1}] \qquad \text{A-1.1}$$

where S_m is the geometrical mean between the internal and the external surfaces of the body.

6.2.2. General prescription

The average internal and external temperature should be set to satisfy the following relations:

$$T_i - T_e = 25\ °C \pm 2\ °C \qquad \text{A-1.2}$$

$$\frac{T_i + T_e}{2} = 20\ °C \pm 0.5°C \qquad \text{A-1.2}$$

The external ventilation should provide a external air velocity in the range 1-2 ms^{-1}.

The electrical fan heater should provide an overall flow rate equal to 40 to 70 times the internal volume per hour.

Instruments must ensure the K value with a maximum error of $\pm 5\%$, while the electrical power consumption should be measured with ac accuracy of 0.5%.

6.2.3. Test procedure, stability and duration of the test

During the test the following condition should be satisfied:

- The value of the maximum and minimum internal air temperature measured by the 12 temperatures sensors must not exceed 2 K;
- The value of the maximum and minimum external air temperature measured by the 12 temperature sensors must not exceed 2 K;

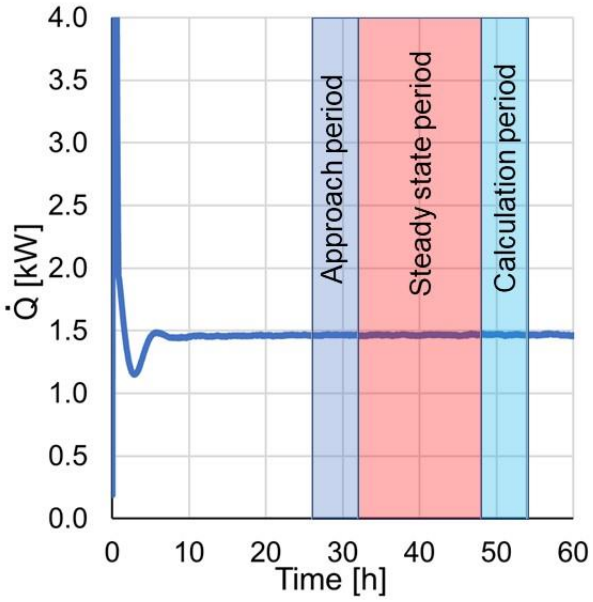

Figure A-1.2 -Subdivision in Approach period, Steady state period and calculation period in the ATP test

Approach period

- The steady state period should be preceded by an approach period during at last 6 hours. During the approach period the mean internal temperature T_i and the mean expernal temperature T_e should not vary by more than $\pm$ 1°C;

Steady state period

- The steady state should be maintained after the approach for at least 12 h. During the steady state the mean internal temperature T_i and the mean expernal temperature T_e should not vary by more than $\pm$ 0.3°C;
- The average electrical power $\dot{Q}$ has to be computed at the beginning and at the end of the calculation period. Each average should account at least 3 hours of acquisitions, and the two intervals should be separated by at least six hours;

Calculation period

- The calculation period which should cover at last the last 6 hours of the stability period;

- The mean internal temperature T_i and the mean expernal temperature T_e difference between the beginnig and the end of the calculation period should be less than $\pm\ 0.2°C$;

The average values of the acquisition during the calculation period should be used to assess the overall heat transfer coefficient of the insulated body as defined in equation A.1-1.

References

[1] United Nations Economic and Social Council, Economic Commission for Europe, Agreement on the International Carriage of Perishable Foodstuffs and on the Special Equipment to be used for such Carriage, United Nations, Geneva.

List of pubblications

Journal papers

Artuso P., Rossetti A., Minetto S., Marinetti S., Moro L., Del Col D., 2019. Dynamic modeling and thermal performance of a refrigerated truck body during operation. *International Journal of Refrigeration*, 99: 288-299.

Papers submitted to journals

Artuso P., Rossetti A., Minetto S., Marinetti S., Del Col D., 2019. Modelling the performance of a new cooling unit for refrigerated transport using carbon dioxide as the refrigerant. *International Journal of Refrigeration* (submitted)

Papers published in indexed Conference Proceedings

Artuso, P., Rossetti, A., Minetto, S., Marinetti, S., Del Col, D. Numerical investigation on the thermal performance of a new cooling unit for refrigerated transport application using CO_2 as working fluid. *Ammonia and CO2 Refrigeration Technologies*, April 11-13, 2019, Ohrid, Republic of Macedonia.

Artuso, P., Rossetti, A., Minetto, S., Marinetti, S., Del Col, D. Numerical modelling of transient heat transfer phenomena in a refrigerated truck body during operation. *37th UIT Heat Transfer Conference*, June 24-26, 2019, Padova, Italy.

Artuso P., Rossetti A., Minetto S., Marinetti S., Ferrari F. Impact of PWM Valve Unsteadiness on the performance of a Commercial Display Cabinet Evaporator. *37th UIT Heat Transfer Conference*, June 24-26, 2019, Padova, Italy.

Artuso, P., Rossetti, A., Minetto, S., Marinetti, S., Del Col, D. Numerical transient simulation of the insulating performance of a refrigerated truck body. *25th IIR International Congress of Refrigeration*, August 24-30, 2019, Montreal, Quebec, Canada.

Rossetti, A., Artuso, P., Minetto, S., Marinetti, S., Zennaro, D. Innovative layout for electric powered refrigeration for insulated trucks: the integration of photovoltaic generator. *25th IIR International Congress of Refrigeration*, August 24-30, 2019, Montreal, Quebec, Canada.

Papers published in Conference Proceedings

Artuso, P., Del Col, D., Rossetti,A., Minetto,S., Marinetti,S., « Experimental analysis of the dynamic behavior of the insulated box in refrigerated truck », XVII European Conference: the lastest technology in refrigeration and air conditioning, 2017